Proximity Effects in Epitaxial Graphene on SiC and their Impact on Atomic-Scale Charge Transport

Dissertation
zur Erlangung des mathematisch-naturwissenschaftlichen Doktorgrades
"Doctor rerum naturalium"
der Georg-August-Universität Göttingen

im Promotionsstudiengang Physik
der Georg-August University School of Science (GAUSS)

vorgelegt von

Anna Sinterhauf
aus Preetz

Göttingen, 2021

Betreuungsausschuss

PD Dr. Martin Wenderoth

IV. Physikalisches Institut, Georg-August-Universität Göttingen

Prof. Dr. Hans-Christian Hofsäss

II. Physikalisches Institut, Georg-August-Universität Göttingen

apl. Prof. Dr. Vasily Moshnyaga

I. Physikalisches Institut, Georg-August-Universität Göttingen

Mitglieder der Prüfungskommission

Referent: PD Dr. Martin Wenderoth

IV. Physikalisches Institut, Georg-August-Universität Göttingen

Korreferent: Prof. Dr. Hans-Christian Hofsäss

II. Physikalisches Institut, Georg-August-Universität Göttingen

Korreferent: Prof. Dr. Rolf Möller

Fakultät für Physik und Center for Nanointegration Duisburg-Essen (CeNIDE), Universität Duisburg-Essen

Weitere Mitglieder der Prüfungskommission

Prof. Dr. Thomas Weitz

I. Physikalisches Institut, Georg-August-Universität Göttingen

Prof. Dr. Christian Jooß

Institut für Materialphysik, Georg-August-Universität Göttingen

apl. Prof. Dr. Michael Seibt

IV. Physikalisches Institut, Georg-August-Universität Göttingen

Prof. Dr. Claus Ropers

Max-Planck-Institut für Biophysikalische Chemie, Göttingen

IV. Physikalisches Institut, Georg-August-Universität Göttingen

Tag der mündlichen Prüfung: 31.08.2021

Introduction

Interactions and couplings between two materials in close proximity take place at the interface and can dominate not only the properties of the interface itself, but of the entire material. This concept of bringing materials with different properties into contact with each other is the basis of many electronic devices.

For example, if we consider a simple metal-semiconductor contact, two different cases can occur depending on the difference in work function of the metal and the (n-doped) semiconductor. If, on the one hand, the work function of the metal is smaller than that of the semiconductor, a charge is generated at the interface which compensates the difference between the Fermi energies. In this case, current flow is possible in both directions across the boundary layer and this type of device represents a simple ohmic contact. If, on the other hand, the work function of the metal is greater than that of the (n-doped) semiconductor, an energy barrier forms at the interface, the so-called Schottky barrier, resulting in rectifying properties with respect to the current flow [1]. This type of contact is called Schottky diode. Although there is no common definition of the term 'proximity effect', effects such as the formation of a Schottky barrier can be understood as such: the proximity of two materials to each other leads to an interaction between them, which in turn dominates the properties around the interface.

Another mechanism that relates to the term proximity is so-called remote doping. Dopant impurities are introduced at specific locations in a semiconductor structure by selectively burying them [2]. Typically, this approach is combined with the epitaxial growth of semiconductors, such as molecular beam epitaxy, or chemical vapor deposition. The proximity and resulting coupling of the carrier matrix to the dopant atoms allows the properties of the carrier matrix to be tuned. A prominent example of this is the burial of Si in GaAs [2].

A third area in which the term proximity effect is used is the field of superconductivity. As early as 1932, R. Holm and W. Meissner observed supercurrents in superconductor - normal conductor - superconductor heterostructures [3]. Contact of a superconductor to a normal conductor can lead to a lowering of the critical temperature of the superconductor and, at the same time, to signs of superconductivity

on mesoscopic length scales in the normal conductor [4]. In this case, the critical temperature of the heterostructure is dominated by the thickness of the superconducting layer [4].

Two findings can be deduced from these three examples. Firstly, if we bring two materials in proximity, interaction can occur between the materials at their interface. Secondly, the properties of the interface can be manifold and depend on the properties of the materials involved. If now one of these materials in close proximity to each other is replaced by a 2D material, this 2D material is essentially an interface to the 3D system. In this sense, proximity effects significantly determine the properties of the whole 2D material.

A well-known example of this is the strong n-type doping of graphene on silicon carbide (SiC), which originates from the spontaneous polarization of SiC mediated via donor-like states in the so-called buffer layer, a carbon-rich interlayer between graphene and SiC [5]. However, this example already raises questions as to what exactly is meant by the term 'proximity effect' in the context of graphene, since a total of three different areas are involved in the example, i.e. the SiC substrate, the buffer layer and the graphene sheet itself. In the context of this work, we use this term to refer to changes in the properties of graphene compared to an isolated, perfect graphene layer, which have their origin in the spatial proximity of the graphene to other materials. Thus, in the case of the doping, this includes both the buffer layer and the SiC.

Proximity effects in graphene on SiC have often been considered troublesome in the past. For example, it was initially believed that the pseudo-relativistic behavior of a graphene monolayer resulting from its linear dispersion could not be observed in epitaxial graphene on SiC due to its strong coupling to the substrate [6]. However, this controversy was settled when the 'half-integer quantum Hall effect', which is evidence of pseudo-relativistic behavior, was experimentally observed in graphene on SiC [7–9]. Nevertheless, in graphene on SiC a strong influence of the substrate is noticeable, which is not only evident in the already mentioned n-type doping, but also in the limited mobility of the charge carriers [9]. Therefore, different strategies were pursued to reduce this coupling. Besides improving the growth processes [10,11], significant progress has been made by exploring different substrates such as boron nitride [12]. Furthermore, there is also a way to reduce the graphene-substrate

interaction in epitaxial graphene on SiC: partially etching the substrate away yields so-called suspended graphene [13].

Another idea to reduce the interaction of the graphene with the SiC substrate was to intercalate an element between both materials [14,15]. Although this approach can drastically reduce the temperature dependence of the sheet resistance and increase the carrier mobility [16] (which is why it is referred to as quasi-free-standing graphene), the intercalation results in its own graphene-substrate interactions. For hydrogen intercalated graphene, e.g., a p-type doping is observed.

Intercalation could be achieved for a variety of different elements, such as Cu [17], Au [18], Ge [19], F [20], Pb [21] or Pd [22]. It turns out that the properties of the graphene are strongly dependent on the atomic species that is intercalated, which can also be understood as a manifestation of proximity coupling. Approaches to exploit the proximity of graphene to certain materials in order to specifically tune graphene's properties start to emerge [13,23–27]. One idea is to tune graphene's charge carrier density by bringing it in close proximity to metals. It was shown theoretically that contact with metals results in a species- and separation-dependent doping of the graphene [28,29]. Furthermore, if superconducting materials are brought into contact with graphene, proximity superconductivity can be observed [30]. Contact with transition metal dichalcogenides leads to a significant increase in the spin-orbit coupling in the graphene [23,24].

However, to turn these approaches into truly beneficial tools to engineer epitaxial graphene's properties, it is first necessary to investigate proximity effects in pristine graphene on SiC and to understand the coupling mechanisms behind them. A direct influence of the proximity to the substrate is seen in the charge transport properties of epitaxial graphene, as characteristic quantities such as the charge carrier density and the charge carrier mobility are significantly affected [31]. In this thesis, a comprehensive approach based on linking local structural, electronic as well as transport properties is used to investigate proximity effects of the SiC substrate on epitaxial graphene. This allows to identify local variations in the coupling and to gain access to the fundamental mechanisms of the substrate-graphene interaction.

Outline

Section 1 | An introduction to the fundamental properties of graphene covering the crystal and the electronic structure is presented. Furthermore, characteristics of epitaxial graphene on SiC are reviewed and concepts of electronic transport, in particular in two dimensions, are introduced.

Section 2 | This section serves to present the different experimental methods that have been used for structural, electronic and transport characterization of graphene on SiC. In particular, the scanning probe methods of scanning tunneling microscopy and atomic force microscopy are introduced.

Section 3 | Starting from a mesoscopic point of view, the resistance anisotropy of high-quality graphene on SiC is determined. By adding local scale information based on scanning tunneling potentiometry on the sheet resistance as well as the resistance of SiC substrate steps, the remaining anisotropy is explained. This project has been carried out in cooperation with partners from PTB Braunschweig (division head PD Dr. Hans Werner Schumacher) as well as partners from TU Chemnitz (group of Prof. Dr. Christoph Tegenkamp). The results have been published in Ref. [32].

Section 4 | The impact of the SiC substrate on the local sheet resistance is in the focus of this section. By applying scanning tunneling potentiometry to high-quality graphene, the local charge transport properties are linked to the properties of the substrate. Thereby, systematic variations in the sheet resistance are revealed, which are correlated with the stacking of the SiC substrate as well as with the distance of the graphene to the substrate. This project has been carried out in cooperation with partners from PTB Braunschweig (division head PD Dr. Hans Werner Schumacher) as well as partners from TU Chemnitz (group of Prof. Dr. Christoph Tegenkamp and group of Prof. Dr. Thomas Seyller). The results have been published in Ref. [33].

Section 5 | This section puts emphasis on literature results devoted to surface potential variations by discussing them against the results of this thesis. To this end, surface potential measurements based on Kelvin probe force microscopy and calculations of low-energy electron microscopy spectra are presented.

Section 6 | The impact of substrate steps, an unavoidable defect even in high-quality graphene on SiC samples, on the charge transport is studied. In particular,

it is revealed that the resistance associated with SiC substrate steps shows strong intrinsic variations, which are traced back to the local electronic properties. This project has been carried out in cooperation with partners from PTB Braunschweig (division head PD Dr. Hans Werner Schumacher). The results have been published in Ref. [34].

Section 7 | A summary of the experimental results in a broader context is presented along with an outlook for future research questions.

General remarks | Where applicable, the results have been edited from their appearance in the respective journals to ensure readability. This editing includes, e.g., the font style and the layout of the citations. However, the content of figures and text remains unchanged. An author contributions statement is included for each publication individually.

Publications Related to This Thesis

1. D. Momeni Pakdehi, J. Aprojanz, **A. Sinterhauf**, K. Pierz, M. Kruskopf, P. Willke, J. Baringhaus, J. P. Stöckmann, G. A. Traeger, F. Hohls, C. Tegenkamp, M. Wenderoth, F.-J. Ahlers, H. W. Schumacher, Minimum resistance anisotropy of epitaxial graphene on SiC, *ACS Applied Materials & Interfaces* **10**(6), 6039-6045 (2018)

   included in section 3.2

2. **A. Sinterhauf**, G. A. Traeger, D. Momeni Pakdehi, P. Schädlich, P. Willke, F. Speck, T. Seyller, C. Tegenkamp, K. Pierz, H. W. Schumacher, M. Wenderoth, Substrate induced nanoscale resistance variation in epitaxial graphene, *Nature Communications* **11**, 555 (2020)

   included in section 4.2

3. **A. Sinterhauf**, S. Bode, M. Auge, M. Lukosius, G. Lippert, H. Hofsäss, M. Wenderoth, A comprehensive study of charge transport in Au-contacted graphene on Ge/Si(001), *Applied Physics Letters* **117**, 023104 (2020)

4. J. Aprojanz, P. Rosenzweig, T. T. Nhung Nguyen, H. Karakachian, K. Küster, U. Starke, M. Lukosius, G. Lippert, **A. Sinterhauf**, M. Wenderoth, A. A. Zakharov, C. Tegenkamp, High-mobility epitaxial graphene on Ge/Si(001) substrates, *ACS Applied Materials & Interfaces* **12**(38), 43065-43072 (2020)

5. **A. Sinterhauf**, G. A. Traeger, D. Momeni Pakdehi, K. Pierz, H. W. Schumacher, M. Wenderoth, Unraveling the origin of local variations in the step

resistance of epitaxial graphene on SiC: a quantitative Scanning Tunneling Potentiometry study, *Carbon* **184**, 463–469 (2021)

included in section 6.2

Table of Contents

Introduction i

Publications Related to This Thesis vii

Table of Contents ix

1 Theoretical Background 1

1.1 Graphene 1

1.1.1 Crystal and Electronic Structure of Monolayer Graphene 2

1.2 Graphene on Substrates 4

1.3 Epitaxial Graphene on SiC 7

1.3.1 Properties of the Buffer Layer 8

1.3.2 Polarization of the SiC and Graphene's Doping 10

1.4 Graphene Growth on SiC 12

1.5 Electronic Transport 13

1.5.1 Electronic Transport in 2D 15

1.5.2 Inelastic Scattering in Graphene 17

1.5.3 Finite Transmission in Graphene at SiC Substrate Steps 18

1.5.4 Current Density Simulations 22

2 Experimental Methods 25

2.1 Structural Analysis 25

2.1.1 Scanning Tunneling Microscopy 26

2.1.2 Atomic Force Microscopy 29

2.2 Analysis of Electronic Properties 31

2.2.1 Scanning Tunneling Spectroscopy 31

2.2.2 Kelvin Probe Force Microscopy 32

2.3 Transport Properties on a Local Scale 33

2.3.1 Scanning Tunneling Potentiometry 34

2.3.2 Kelvin Probe Force Microscopy for Transport Measurements 35

2.4 Experimental STM Setup 36

3 Charge Transport in Graphene from Mesoscopic to Microscopic 39

3.1 Author Contributions 39

3.2 Minimum Resistance Anisotropy of Epitaxial Graphene on SiC 40

3.2.1 Introduction 40

3.2.2 Sample Preparation 42

3.2.3 Results and Discussion 43

3.2.4 Conclusion 50

3.2.5 Acknowledgement 51

3.2.6 Supplementary Information 51

4 Sheet Resistance on a Local Scale 55

4.1 Author Contributions 56

4.2 Substrate Induced Nanoscale Resistance Variation in Epitaxial Graphene 57

4.2.1 Introduction 57

4.2.2 Results 59

4.2.3 Discussion 67

4.2.4 Methods 72

4.2.5 Acknowledgement 74

4.2.6 Supplementary Information 74

5 SiC Stacking Order and Surface Potential 85

5.1 Surface Potential from KPFM 86

5.2 Simulation of LEEM-IV Spectra 88

6 Line Defects in Local Transport Measurements 91

6.1 Author Contributions 92

6.2 Unraveling the Origin of Local Variations in the Step Resistance of Epitaxial Graphene on SiC: A Quantitative Scanning Tunneling Potentiometry Study 92

6.2.1 Introduction 93

6.2.2 Results 95

6.2.3 Discussion 98

6.2.4 Conclusion 103

6.2.5 Methods 104

6.2.6 Acknowledgements 105

6.2.7 Supplementary Information 105

7 Big Picture 107

7.1 Outlook 109

Bibliography 111

List of Abbreviations 121

Danksagung 123

1 Theoretical Background

This section reviews the theoretical properties of graphene necessary to understand the physical processes discussed in this thesis. We start with an introduction to the crystal and electronic structure of single layer graphene in section 1.1.1. More detailed information on the fundamental properties of graphene can be found in [35,36].

Next, the consequences of the proximity of a graphene layer to a real substrate are discussed for different substrates in section 1.2, before the case of graphene on SiC is elaborated (section 1.3), which is the focus of this work. Here we discuss the properties of the SiC such as the stacking sequence and the resulting properties of the graphene. Furthermore, the so-called buffer layer (section 1.3.1) as well as the concept of polarization doping and the intrinsic n-type doping of graphene on SiC are discussed (section 1.3.2). Subsequently, in section 1.4 the sample growth is explained.

This section concludes with a description of charge transport (section 1.5). Starting with the Drude model and Sommerfeld's extension, this section covers diffuse scattering in the context of the sheet resistance (section 1.5.2) as well as scattering at localized defects (section 1.5.3). In addition, the peculiarities of the description of charge transport in 2D are discussed in section 1.5.1. This section concludes with the description of simulations based on finite elements, which are used to calculate the current density (section 1.5.4).

1.1 Graphene

For almost two decades, graphene has been one of the most comprehensively studied materials due to its extraordinary properties. It provides a truly two-dimensional carbon allotrope and thereby complements the three-dimensional diamond and graphite, as well as the one-dimensional carbon nanotubes and the zero-dimensional fullerens. The first experimental realization was achieved by K. S. Novoselov and A. K. Geim in 2004 [37] and subsequently, they provided the first electronic characterization of this fascinating material [37]. Their experiments triggered

the emergence of a wide field of graphene research, as well as the study on related two-dimensional materials such as boron nitride (BN) [38].

1.1.1 Crystal and Electronic Structure of Monolayer Graphene

Graphene is a monoatomic layer of carbon atoms arranged in a periodic honeycomb lattice. This crystal structure is dominated by two different types of bondings within the sp^2 hybridization. Three of the four valence orbitals $2s$-, $2p_x$- and $2p_y$-orbitals form σ bonds within the layer. The remaining p_z- orbitals, with z being the direction normal to the graphene sheet, form π orbitals. These π orbitals crucially determine the electronic properties of the graphene. The carbon atoms in the graphene layer are localized at the vertices of a honeycomb lattice, which can be described as a hexagonal bravais lattice with two basis vectors $\overrightarrow{a_1}$ and $\overrightarrow{a_2}$:

$$\overrightarrow{a_1} = a\left(\frac{\sqrt{3}}{2}, \frac{1}{2}\right), \quad \overrightarrow{a_2} = a\left(\frac{\sqrt{3}}{2}, -\frac{1}{2}\right) \qquad (1.1)$$

with $a = \sqrt{3}\, a_{cc}$ and $a_{cc} = 1.42$ Å being the distance between two neighboring carbon atoms. The lattice consists of a basis of two atoms A and B. In Figure 1.1 the atoms A and B are depicted as blue and grey dots, respectively. Every atom is

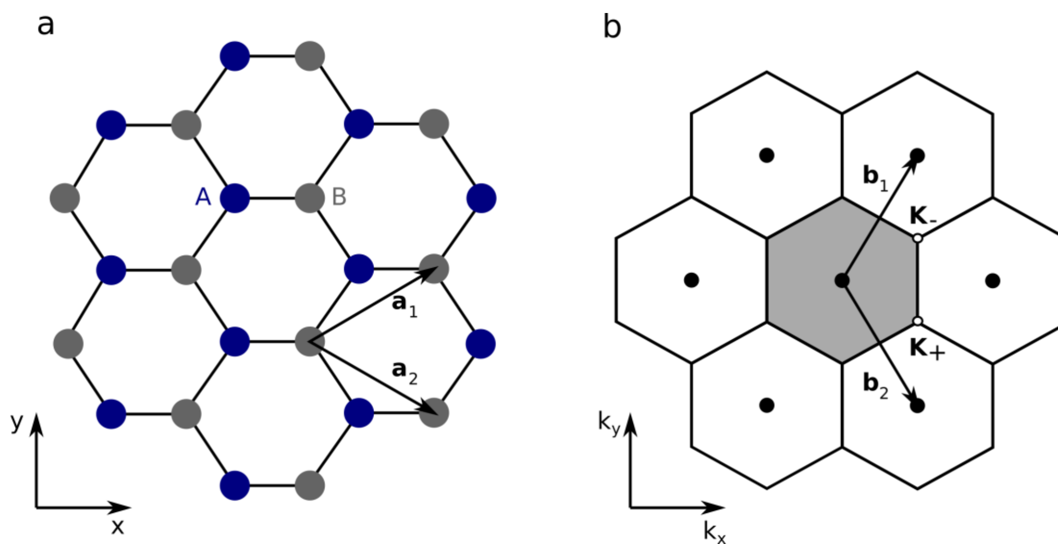

Figure 1.1 Graphene Bravais lattice In (a) the honeycomb lattice of graphene is shown, which can be described using a two atomic basis of A and B and two basis vectors $\overrightarrow{a_1}$ and $\overrightarrow{a_2}$. In (b) the corresponding reciprocal lattice is depicted, which itself is a hexagonal bravais lattice with basis vectors $\overrightarrow{b_1}$ and $\overrightarrow{b_2}$. K_- and K_+ are high symmetry points, grey shaded area indicates the Brillouin zone. Graphic adapted from Foa Torres, Roche & Charlier, Introduction to Graphene-Based Nanomaterials [35]. Copyright (2014) by Foa Torres, Roche & Charlier, reproduced with permission of Cambridge University Press through PLSclear.

surrounded by three atoms of the other sublattice. The reciprocal lattice vectors $\overrightarrow{b_1}$ and $\overrightarrow{b_2}$ read

$$\overrightarrow{b_1} = b\left(\frac{1}{2}, \frac{\sqrt{3}}{2}\right), \quad \overrightarrow{b_2} = b\left(\frac{1}{2}, -\frac{\sqrt{3}}{2}\right) \tag{1.2}$$

with $b = \frac{4\,\pi\sqrt{3}}{a}$. The reciprocal honeycomb lattice of graphene is shown in Figure 1.1b. Typically, the corner points of the Brillouin zone are denoted by K_- and K_+, and can be chosen as follows

$$\overrightarrow{K_-} = \frac{4\pi}{3a}\left(\frac{\sqrt{3}}{2}, -\frac{1}{2}\right), \quad \overrightarrow{K_+} = \frac{4\pi}{3a}\left(\frac{\sqrt{3}}{2}, \frac{1}{2}\right). \tag{1.3}$$

The electronic properties of graphene can be derived using the tight-binding-model, which was done for the first time by Wallace in 1947 [39]. The resulting energy dispersion reads [35]

$$E_\pm(\vec{k}) = \pm\gamma_0|\alpha(\vec{k})| = \pm\gamma_0\sqrt{3 + 2\cos(\vec{k}\overrightarrow{a_1}) + 2\cos(\vec{k}\overrightarrow{a_2}) + 2\cos\left(\vec{k}(\overrightarrow{a_1} - \overrightarrow{a_2})\right)}. \tag{1.4}$$

The wave vector $\vec{k}$ is chosen within the first Brillouin zone. For graphene, there are zeros of $\alpha(\vec{k})$ indicating a crossing of the two energy bands (equation 1.4). The crossing occurs at K_- and K_+ (Figure 1.2). By expanding the energy dispersion around K_- and K_+, a linear dispersion relation (for small energies) is found for the corner points of the first Brillouin zone

$$E_\pm(\delta\vec{k}) = \pm\hbar v_F|\delta\vec{k}| \tag{1.5}$$

where $v_F = \frac{\sqrt{3}\gamma_0 a}{2\hbar}$ is the group velocity. Here, the plus sign and the minus sign refer to electron states and hole states, respectively. The electronic properties at these crossing points are similar to those of massless Dirac fermions yielding the Dirac cones depicted in Figure 1.2. Following this line, K_- and K_+ are called Dirac points and charge carriers in graphene are treated as pseudo-relativistic particles with a group velocity of $8.4 \cdot 10^5\ \frac{m}{s}$ [35], which can be described by the Weyl-Dirac-equation (instead of the Schrödinger-equation). The linear dispersion is one of the most outstanding characteristics of monolayer graphene. The regions around the Dirac points are also referred to as valleys [16].

The corner points of the Brillouin zone and the corresponding sublattices are electronically not equivalent. As a consequence, the total wave function of an electron can be written as a two-component vector, which is composed of the respective parts of the Bloch wave functions of the two sublattices. The relative amplitude of these two wave functions is called pseudo-spin and represents an additional degree of freedom of the system.

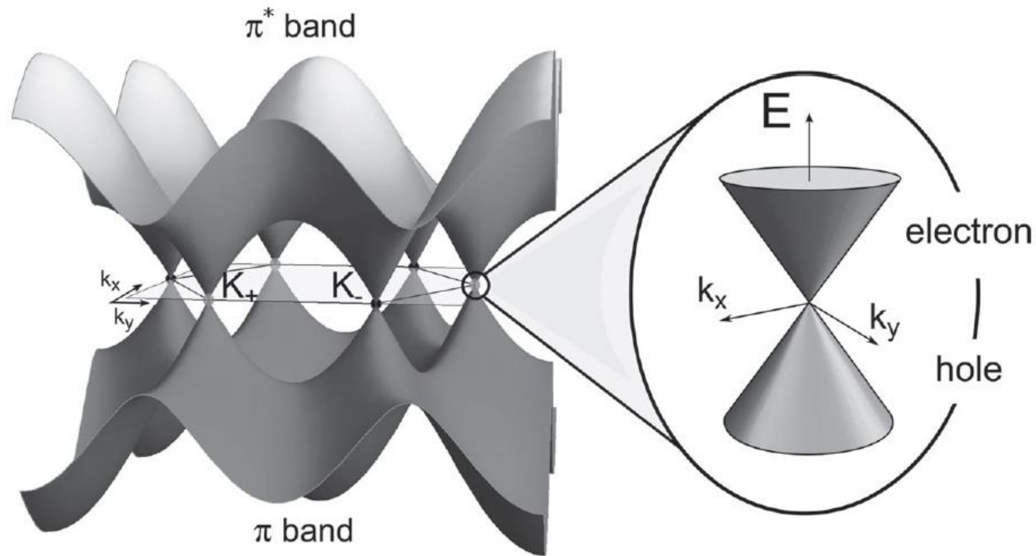

Figure 1.2 Graphene valence and conduction band. Schematic illustration in reciprocal space. Close to the K_- and K_+ the linear dispersion relation leads to 'Dirac cones' depicted in the close-up. Graphic adapted from Foa Torres, Roche & Charlier, Introduction to Graphene-Based Nanomaterials [35]. Copyright (2014) by Foa Torres, Roche & Charlier, reproduced with permission of Cambridge University Press through PLSclear.

As K_- and K_+ are separated in k-space, only sharp, atomic-scale potentials can scatter charge carriers from one sublattice to the other, which is referred to as intervalley scattering. Examples for such sharp atomic-scale potentials are step edges or point defects in the graphene lattice, such as vacancies. If electrons are scattered within a Dirac cone or between two cones of the same sublattice this scattering processes is referred to as intravalley scattering [35].

1.2 Graphene on Substrates

In the previous theoretical considerations of graphene, the fact that the graphene layer is in most cases in direct proximity to a substrate has so far been neglected.

However, since this is the central aspect of this thesis, this section briefly reviews the most commonly used substrates. A detailed discussion of the properties and impact of the substrate in graphene on SiC, the material of choice in this thesis, is given in section 1.3.

The very first graphene flakes were exfoliated using the scotch tape method on graphite until only one layer of graphene was left [37]. In this approach, adhesive tape is pressed onto an HOPG crystal and, when peeling it off, graphite layers stick to the scotch tape. These graphite layers are further exfoliated and finally transferred to a substrate. This process yields graphene flakes with a varying number of layers that are randomly distributed on the chosen substrate. Suitable substrates are SiO_2 or hexagonal BN. Although both substrates are suitable for an electronic characterization of graphene due to their insulating nature, there is still a non-negligible interaction of the graphene with the substrate. In the case of SiO_2, e.g., the carrier mobility is limited by scattering from charged impurities and optical phonons of the substrate [12]. Moreover, graphene on SiO_2 exhibits a non-negligible doping. Although this doping can be tuned routinely to the charge neutrality point by using a gate, in the vicinity of the Dirac point, the 2D electron gas, by which the graphene can be well described in this case, breaks up into so-called electron hole puddles [12]. The use of hexagonal BN allows to reduce some of these substrate induced effects, such as the intrinsic doping, however, the fundamental interactions are similar to those on SiO_2. In addition, it should be noted that the growth of high-quality 2D hBN is still a major challenge [38] .

The second graphene production method is called chemical vapor deposition (CVD), where carbon-rich gases are deposited onto a substrate. This method relies on epitaxy to the chosen substrate. Carbon-rich gases like methane are used as precursors, and the growth was demonstrated for a wider range of metal substrates, such as ruthenium [40], iridium [41], and copper [42]. Graphene on metal substrate shows a strong hybridization between the electronic states of the graphene and the metal [43]. In line with this, theoretical studies investigate the charge transfer from different metals to graphene as a function of the proximity between the two systems [28,29] and find a distance-dependent doping (Figure 1.3). Structurally, a pronounced Moiré type superstructure is observed in scanning tunneling microscopy (STM) experiments [43]. Moreover, graphene on metallic substrates is typically characterized by the presence of line defects in the form of winkles and strain due to a mismatch of the lattice constants [44].

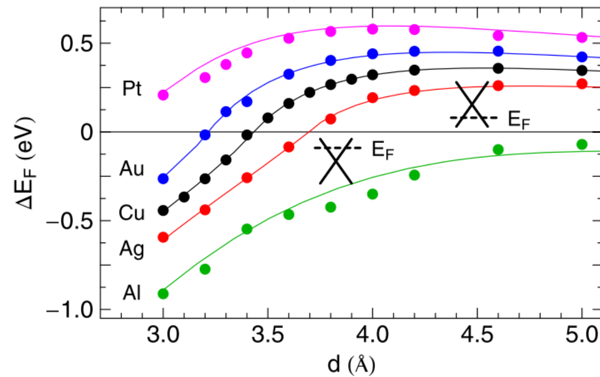

Figure 1.3: Graphene in proximity to a metal shows a distance dependent shift in the Fermi level. Reprinted figure with permission from Giovannetti *et al.* Doping graphene with metal contacts. *Phys. Rev. Lett.* **101**, 026803 (2008) [28]. Copyright (2008) by the American Physical Society.

For some years now, it has also been possible to produce graphene by CVD on non-metallic substrates such as germanium [45] (see Figure 1.4). This type of sample system has also been studied in this work and the results have been published in two papers Ref. [46] and Ref. [47]. Graphene on germanium is characterized by substrate induced grain boundaries and crystalline imperfections, which limit the carrier mobility. Nevertheless, mobility values comparable to graphene on SiC in the range of $1 \times 10^4\ \mathrm{cm^2/Vs}$ were obtained [47].

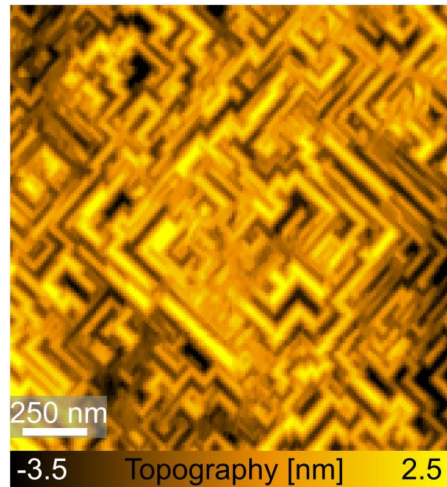

Figure 1.4 AFM topography of pristine Gr/Ge/Si(001). Structurally, graphene on Ge is dominated by facets oriented at 90° to each other. The height of these facets was determined to be about 4 nm. Graphic adapted from Sinterhauf et al. [46] licensed under CC BY 4.0.

1.3 Epitaxial Graphene on SiC

Graphene can routinely be grown from silicon carbide (SiC) substrates by thermal decomposition. Crystalline SiC is a semiconductor with a wide bandgap that exists in more than 150 crystalline forms, also called polytypes [36], with cubic, hexagonal or rhombohedral Bravais lattice. The following remarks refer to hexagonal SiC, which was used as substrate in the present thesis.

The different hexagonal SiC polytypes consist of fundamental layers of silicon and carbon atoms arranged in tetrahedral coordination [48–50]. These layers are referred to as fundamental bilayers. The individual polytypes differ in the arrangement and number of fundamental bilayers within a unit cell. The most commonly used polytypes for epitaxial graphene growth are hexagonal 6H (band gap: 3.05 eV) and hexagonal 4H (band gap: 3.23 eV) [36]. The 4H-SiC and 6H-SiH crystal consists of 4 and 6 stacked fundamental bilayers, respectively. In this thesis, semi-insulating 4H and 6H-SiC polytypes are used as substrate material and all experimental results in sections 3, 4, 5 and 6 are obtained on epitaxial graphene on these SiC polytypes. The stacking sequence of the 6H-SiC is illustrated in Figure 1.5. Due to the composition of the 6H-SiC there are, in principle, 6 different surface terminations. These are named S1, S2, S3, S1*, S2* and S3* according to [51].

When graphene is grown on SiC, the SiC substrate is heated so that the silicon atoms sublime. An important property of the SiC in this context is that the surface terminations have different decomposition velocities [52], which is schematically indicated in Figure 1.5. These decomposition velocities are the origin of step bunching. In this process, step edges move (e.g. due to thermal activation) and two or more steps can be merged and thereby form higher steps [53].

There is disagreement about the quantitative velocities (compare [52] and [53]). A detailed discussion on the step retraction during the graphene growth can be found in [54]. For this thesis, it is important to note that the terminations S1 and S1* have a much higher decomposition velocity than the other surfaces and, thus, disappear first during the graphene growth process [52,53]. Combining this knowledge with high-quality samples with defined step sequences, it is possible to assign the graphene terraces to the local termination of the substrate. This possibility is exploited in section 4.2 revealing a dependence of the local sheet resistance on the termination of the SiC substrate, which we attributed to proximity coupling of the graphene to the SiC substrate.

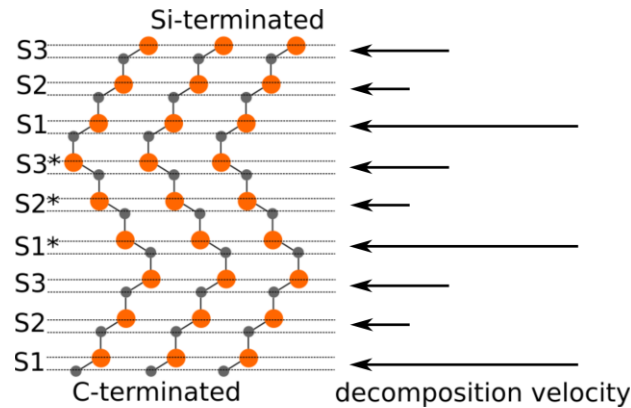

Figure 1.5 Schematic side view of the crystal structure of 6H-SiC and the decomposition velocities according to [52]. Graphic taken from Sinterhauf et al. [33] licensed under CC BY 4.0.

In the following, two other important characteristics of graphene on SiC will be discussed. Firstly, the presence of a carbon-rich intermediate layer between the SiC and the graphene layer, the so-called buffer layer and, secondly, the fact that SiC has a spontaneous polarization. This spontaneous polarization is the origin of the strong n-type doping of graphene on SiC as will be discussed in section 1.3.2.

1.3.1 Properties of the Buffer Layer

The buffer layer is a carbon-rich layer that resides on the SiC substrate as shown in Figure 1.6a. The crystallographic structure of the buffer layer is similar to that of graphene [36], however, one-third of the carbon atoms in the buffer layer is bonded to Si in the SiC below [55] resulting in a very large unit cell that complicates an exact determination of the structure of the buffer layer [36]. Nevertheless, the buffer layer can be reversibly transformed to a graphene layer. This was demonstrated by intercalating hydrogen between the SiC substrate and the buffer layer [15].

At elevated temperature (T>300°C), hydrogen gas dissociates and intercalates between buffer layer and the SiC surface. The hydrogen atoms form Si-H bonds at the SiC surface [56] and, thereby, break the Si-C bonds of the buffer layer and, additionally, the hydrogen saturates dangling bonds [14,15]. This breaking of the Si-C bonds leads to a reconstruction of the buffer layer to a graphene layer. In this way, monolayer graphene on SiC is converted into quasi-free-standing bilayer graphene (QFBLG) [96] as shown in Figure 1.6b. In the same way, a buffer layer epitaxially grown on SiC is converted into quasi-free-standing monolayer graphene (QFMLG)

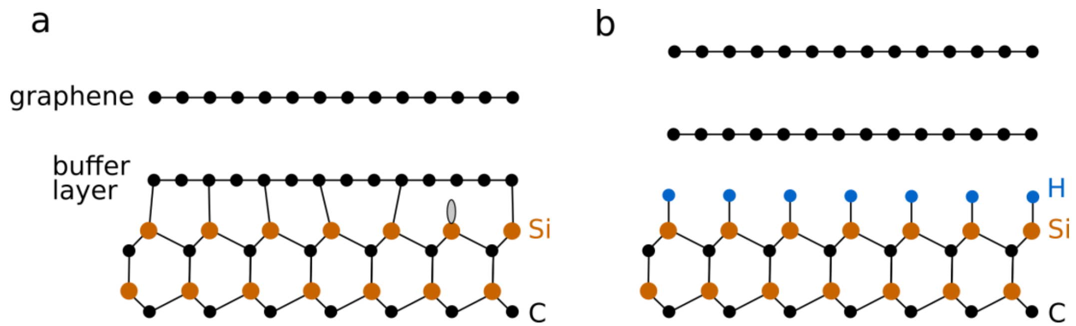

Figure 1.6 Schematics of (a) monolayer graphene on SiC residing on a buffer layer and (b) quasi-free-standing bilayer graphene (QFBLG) on hydrogen saturated SiC.

demonstrating the crystallographic similarities between the buffer layer and a graphene layer. It was demonstrated that quasi-free-standing graphene exhibits an enhanced macroscopic room-temperature mobility with a reduced temperature dependence [16]. The graphene is weakly bound to the hydrogen-terminated SiC surface, which is why intercalated samples are usually referred to as quasi-free-standing.

The buffer layer is characterized by a $6\sqrt{3}\times\ 6\sqrt{3}\ R30$ reconstruction [57]. Although typically covered with at least one graphene layer, it is possible to (partially) image the buffer layer using STM. At sufficiently high tunneling voltages, a significant contribution to the tunneling current originates from states in the buffer layer [58]. In

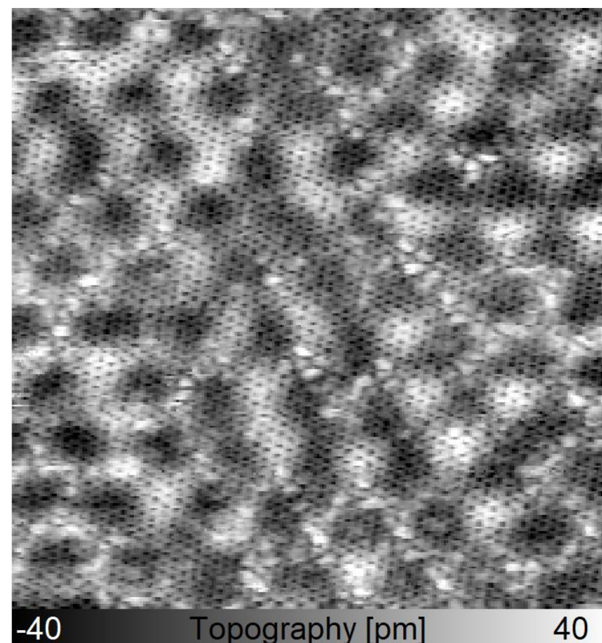

Figure 1.7 15 nm × 15 nm constant current topography ($\mathrm{V_{Bias}} = -0.3\ \mathrm{V}, \mathrm{I_T} = 0.15\ \mathrm{nA}$) showing the graphene lattice, the $6\times\ 6$ reconstruction as well as defect states associated with the buffer layer.

this way, not only a 6×6 reconstruction [59], but also the $6\sqrt{3} \times 6\sqrt{3}\,R30$ structure consistent with low-energy electron diffraction (LEED) measurements was mapped [57]. The origin of the appearance of the 6×6 reconstruction is attributed to the non-bonded carbon atoms forming a superhexagonal network detectable in STM [60]. This is in agreement with photoelectron spectroscopy, which shows interface states for the buffer layer [31]. These interface states are mainly attributed to silicon or carbon dangling bonds [55]. In addition, defect states, are present at the interface as observed by STM [58], see Figure 1.7.

1.3.2 Polarization of the SiC and Graphene's Doping

One of the fundamental properties of hexagonal SiC is the fact that these polytypes carry a spontaneous polarization [31], including the 6H-SiC mainly used in this work. For the 6H-SiC, this spontaneous polarization originates from a broken bulk symmetry in the [0001]-direction resulting in a charge transfer [49] (see Figure 1.8) .

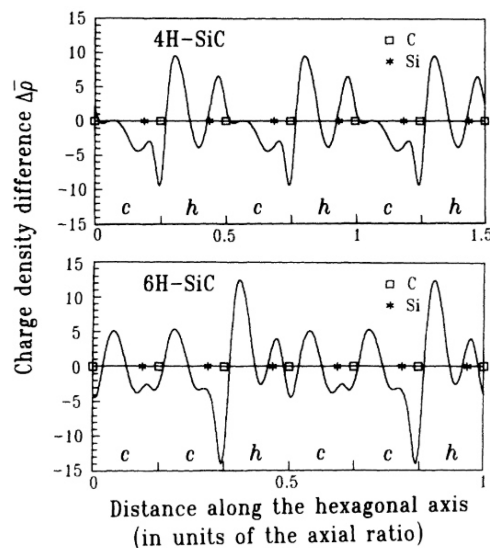

Figure 1.8 Charge transfer in the 4H and the 6H-SiC polytype. Reprinted figure with permission from Park, Cheong, Lee & Chang. Structural and electronic properties of cubic, 2H, 4H, and 6H SiC. *Phys. Rev. B* **49**(7), 4485–4493 (1994) [49]. Copyright (1994) by the American Physical Society.

Although this spontaneous polarization is fundamentally a bulk effect, it becomes important at interfaces. A polarization charge with the same magnitude but opposite sign is formed on the two surfaces of the SiC[i]. For the case of graphene on

[i] if the SiC is placed between two non-pyroelectric layers. A simple example of this is vacuum.

SiC, this can be understood as a layer of charged dopants on the surface of the SiC, as shown schematically in Figure 1.9, which causes donor-like states to form in the buffer layer. These donor-like states overcompensate for the polarization of the SiC substrate and provide a strong n-type doping with a Fermi level position of about 0.45eV above the Dirac energy and a charge carrier concentration of roughly $1 \times 10^{13}\ \mathrm{cm}^{-2}$ [31] in the graphene as shown schematically in Figure 1.9a.

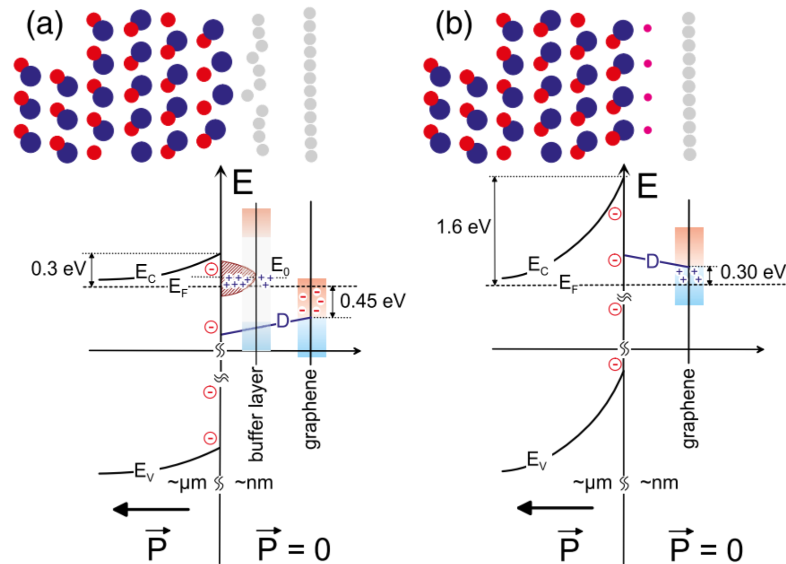

Figure 1.9 Schematics of the origin of the (a) strong n-type doping in epitaxial graphene on SiC and the (b) p-type doping in H-intercalated graphene on SiC. The main cause is the spontaneous polarization of the SiC substrate, which leads to a pseudo-charge at its surface. Reprinted figure with permission from Ristein, Mammadov & Seyller. Origin of doping in quasi-free-standing graphene on silicon carbide. *Phys. Rev. Lett.* **108**, 246104 (2012) [31]. Copyright (2012) by the American Physical Society.

In contrast to this, hydrogen intercalated graphene on SiC shows a p-type conductivity [5]. Due to the absence of a buffer layer, a p-type doping is formed in the graphene layer to compensate for the spontaneous polarization of the SiC (see Figure 1.9b). This mechanism is usually referred to as polarization doping [31]. Moreover, the strength of this p-type doping was shown to depend on the polytype of the SiC substrate [5], which can be understood recalling Figure 1.8 showing the charge transfer in the SiC for the 4H and the 6H polytype. For QFBLG on 4H-SiC a 1.5 times larger doping was measured than for 6H-SiC as a substrate [5].

Although the term polarization doping was originally introduced for the H-intercalated case [31], this term is also common in the context of n-type doping, because

also here the origin of the doping is the spontaneous polarization of the substrate. Therefore, we will use the term polarization doping also in the context of epitaxial graphene and its n-type doping.

In summary, the doping of both epitaxial graphene on SiC and H-intercalated graphene is caused by the proximity of the graphene to the substrate and can be considered as the dominant proximity effect in graphene on SiC.

A recent study based on Kelvin probe force microscopy (KPFM) under ambient conditions and low-energy electron microscopy (LEEM) IV spectroscopy in vacuum on epitaxial graphene on SiC reports on differences in the strength of the polarization doping depending on the surface termination of the SiC [54]. This topic will be addressed in detail in section 5.

1.4 Graphene Growth on SiC

The graphene production method used to fabricate graphene on SiC is thermal decomposition of SiC and, actually, this method has already been used long before the first experimental realization of graphene in 2004 [37]. Thermal sublimation of SiC and the subsequent graphitization of the surface has first been demonstrated by van Bommel et al. already in 1975 [61]. The first preparation of graphene on the C-terminated face of SiC has been achieved in the group of Walt de Heer [62] and on the Si-terminated face in the group of Thomas Seyller [63]. When graphene is grown epitaxially on SiC, the SiC substrate is heated such that the silicon atoms sublime and the remaining carbon atoms rearrange and form the buffer layer (see section 1.3.1 for details on the buffer layer). Upon further heating, the growth of a second layer starts below the former buffer layer and transforms it into a graphene monolayer. The number of layers as well as the quality of the graphene sheet crucially depend on the growth parameters such as growth temperature, time, and pressure.

Originally, graphene growth on insulating SiC surfaces was carried out by high temperature annealing in vacuum [36,62]. However, vacuum deposition of SiC was demonstrated to yield inhomogeneous, defectuous graphene layers with small grain sizes [64], which is mainly due to step bunching during the high temperature annealing [10]. Furthermore, the decomposition of SiC is not a self-limiting process

and the growth in UHV allows only little control over the layer thickness. Consequently, regions of different graphene layer thickness coexist on a typical UHV-grown graphene sample [10]. Major improvement of the sample quality by refined growth procedures could be achieved in 2009 with the introduction of ex-situ graphitization of Si-terminated SiC in argon atmosphere [10]. This method yields monolayer graphene films with a significantly larger domain sizes compared to graphene grown in UHV. However, even with this refined growth process bilayer stripes start to grow at step edges due to the availability of more carbon.

In 2016, this problem of bilayer formation at step edges was solved by Kruskopf and co-workers [11] who introduced a new fabrication method for epitaxial graphene, which relies on the deposition of a polymer onto the SiC surface prior to the growth process. This procedure is called polymer-assisted sublimation growth (PASG). The polymer acts as an additional carbon source that enhances the graphene nucleation [11] and, thus, suppresses the formation of bilayer regions, as well as the formation of high substrate steps. This method allows to obtain high-quality monolayer graphene on large scales [11,32,65].

The most important property of PASG graphene in the context of this thesis is the absence of bilayer graphene. This results in a homogeneous current density (see section 1.5.4), which in turn is a basic prerequisite for carrying out quantitative local transport measurements. Using a semi-insulating substrate, which is compatible with this growth method, allows to conduct transport experiments at low temperatures as well as at room temperature. This enables temperature-dependent measurements and, thus, allows to unravel different scattering processes. In this thesis, graphene on 4H-SiC and 6H-SiC prepared at PTB Braunschweig is studied in great detail regarding its charge transport properties from a mesoscopic to a microscopic scale in section 3, as well as on a truly atomic scale in sections 4 and 6.

1.5 Electronic Transport

In this section, an introduction to the theoretical description of charge transport is given. The starting point is the Drude model for electron transport and the extensions by Sommerfeld. Subsequently, a description of electronic transport in two dimensional materials is presented in section 1.5.1. Furthermore, the mechanisms behind the experimentally observed resistance of SiC substrate steps (section 6.2)

are reviewed and finite element simulations are presented, which allow to quantify the impact of bilayer patches on the homogeneity of the current density.

The Drude model is a semiclassical description of charge transport in a solid state body caused by an external electric field. In this diffusive model, the current density is given by

$$j = -en\vec{v}_D = \frac{ne^2\tau}{m}E = \sigma \cdot E \qquad \text{and} \qquad \sigma = \frac{ne^2\tau}{m} \tag{1.6}$$

with the momentum relaxation time τ and the charge carrier density n. Although this model is rather simple, it allows to draw an important conclusion: defects cause an increase in resistance and a decrease in conductivity because of the decrease in momentum relaxation time.

The limitations of this simple model become apparent when considering, e.g., the Pauli principle. In the Drude model all electrons contribute to the electric current, which is in conflict with the Pauli principle. Furthermore, it neglects the fact that electrons do not scatter at positively charged lattice atoms. In 1933 the Drude model was extended by Sommerfeld [66], who combined it with quantum-mechanical Fermi-Dirac statistics obeying the Pauli principle. This extension is known as the Drude-Sommerfeld model.

By applying an external cross voltage to the sample, the electrochemical potential is driven to a non-equilibrium state (see section 1.5.3 for details on the electrochemical potential). Within the Drude-Sommerfeld model, an electric field causes

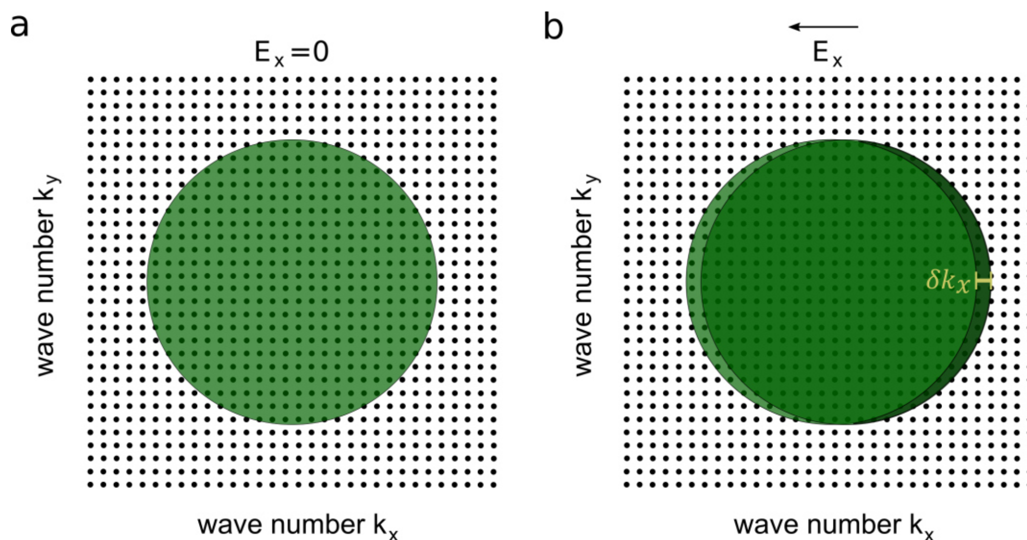

Figure 1.10 Distorted Fermi-surface. Fermi-surface with and without applied electric field in (a) and (b), respectively. The electric field shifts the electron distribution by δk_x. Graphic inspired by [67].

a shift of the Fermi surface in k-space along the direction of the electric field [67] as shown in Figure 1.10. Only very few electrons change from a $\mathbf{k}^-$ state to a $\mathbf{k}^+$ state, thereby causing a displacement of the Fermi surface by δk_x. The Fermi distributions of the $\mathbf{k}^-$ and $\mathbf{k}^+$ states are different, hence their distribution functions are described by two different distribution functions $f(\mathbf{k}^+)$ and $f(\mathbf{k}^-)$.

1.5.1 Electronic Transport in 2D

In the following, well-known quantities that characterize charge transport in three-dimensions are defined for the two-dimensional case, which is particularly important for the discussion of charge transport in our sample system graphene. This section follows the discussion in Ref. [68].

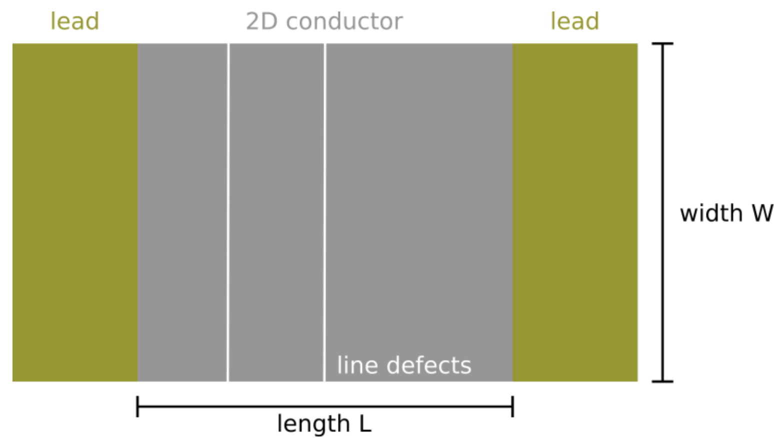

Figure 1.11 Schematics of a 2D conductor with length L, width W, metallic leads and local defects. The conductor is assumed to be a macroscopic system. Consequently, its dimensions are larger than all other length scales relevant for transport, e.g. the phase coherence length or the Fermi wavelength.

The starting point for our discussion is a 2D conductor with width W, length L and two metallic leads as schematically shown in Figure 1.11. For this system, the macroscopic sheet resistance is defined by $\rho_{macro} = R \cdot \frac{W}{L}$, where R denotes the macroscopic resistance of a sample. The resistance can be expressed according to Ohm's law $R = \frac{V}{I}$, with I being the total electric current and V the voltage difference, which is measured between the two leads. For a homogeneous diffusive conductor (without localized defects), a homogeneous electric field across the conductor is expected. However, this situation does not resemble the reality in most experiments. In the case of epitaxial graphene, local inhomogeneities in the sheet resistance arise by e.g. different number of graphene layers or due to the presence

of SiC substrate steps as indicated in Figure 1.11. In the framework of the Landauer formalism these localized defects exhibit a finite transmission probability for charge carriers, which invalidates the assumption of an overall homogeneous electric field. Nevertheless, it is possible to find a region of length δL without localized defects. A homogeneous electric field is present over this length, hence, it is useful to define a local sheet resistance as follows

$$\rho_{local} = \frac{\delta V}{I} \cdot \frac{W}{\delta L} = \frac{E_{local}}{j}. \tag{1.7}$$

For a simple sample geometry as shown in Figure 1.11 the macroscopic current density $j = \frac{I}{W}$ is a good approximation for the local current density, thereby assuming translational invariance in y-direction. Although we will stick with the assumption of a homogeneous current density for now, this does not capture the experimental situation accurately in many cases as will be discussed in section 1.5.3 and section 4.2.

With the definition of the local sheet resistance, areas without localized defects can be described in an appropriate manner. In contrast to this, one-dimensional defects, such as substrate steps, cause a localized voltage drop ΔV. The basic mechanism behind this is discussed in section 1.5.3. Based on this localized voltage drop ΔV, a defect resistance is defined

$$\rho_{defect} = \frac{\Delta V}{j}. \tag{1.8}$$

Introducing the transmission T, the conductivity σ_{defect} can then be written as [68]

$$\sigma_{defect} = \frac{2e^2}{h} \cdot \frac{k_F}{\pi} \cdot T = \frac{1}{\rho_{defect}}. \tag{1.9}$$

These elaborations demonstrate that the macroscopic sheet resistance[ii] for a real sample is composed of several local components as follows

$$\rho_{macro} = \sum_i x^i \cdot \rho_{local}^i + \sum_i n^i \cdot \rho_{defect} \tag{1.10}$$

[ii] In the framework of this description, ρ_{macro} contains contributions from localized defects as well as local sheet resistances and, therefore, it could be argued that it is no longer a sheet resistance. Since it reflects the experimental situation in (most) large scale transport experiments, this nomenclature is still common.

with $x^i = \frac{\delta L_i}{L}$ and δL_i the length over which the local sheet resistance does not vary. n^i represents the defect concentration, which can be written as $n^i = \frac{N_i}{L}$ with the total number of defects of each type N. This issue is addressed experimentally in 3.2, where we use local measurements of sheet resistance and step resistance to understand the remaining anisotropy of high-quality pure monolayer epitaxial graphene.

1.5.2 Inelastic Scattering in Graphene

Inelastic scattering processes such as electron-electron scattering and electron-phonon scattering are the main contributions to the sheet resistance. They are characterized by a loss of phase information. The phase coherence length is typically in the range of a few 100 nm for epitaxial graphene on SiC [69]. In this section, we summarize electron-electron and electron-phonon scattering in graphene with emphasis on the case of graphene on SiC.

Electron-Electron Scattering | The process of electron-electron scattering in graphene becomes dominant at high temperatures accompanied by low doping [70]. However, as discussed in section 1.3.2, graphene on SiC always exhibits strong n-type doping, resulting in electron-electron scattering often being negligible. Experimental detection of electron-electron scattering is, therefore, rare in this system and often requires certain geometries as in the case of the fractional quantum Hall effect [71], or becomes relevant only under certain experimental conditions as in the case of weak (anti) localization, which can be observed in the context of magnetic fields [72]. In contrast to conventional two dimensional electron systems [73], in graphene electrons end up in opposite phase when moving clockwise or anticlockwise around a closed loop, which is a consequence of the unique band structure of graphene and the Berry phase of π of the wave function [74]. This opposite phase leads to destructive interference and a suppression of backscattering, which is known as weak antilocalization.

Electron-Phonon Scattering | There are two possible origins for electron-phonon scattering in graphene on SiC, firstly, intrinsic phonon modes, i.e. acoustic and optical phonon modes of the graphene itself, and, secondly, remote interfacial phonons of the substrate and the buffer layer. As intrinsic optical phonon modes do not couple strongly to the electrons due to their out-of-plane nature [75], electron-

phonon scattering is governed by the contribution from remote interfacial phonons [16,76,77]. This scattering mechanism [78] is not only relevant for electron-phonon scattering in graphene on SiC, but is also observed, e.g., in carbon nanotubes on SiO_2 [79]. Furthermore, we discussed this scattering process in Ref. [80] for graphene on SiO_2.

If only a single phonon mode is considered, the temperature dependence of the resistance due to remote-phonon scattering can be described by [16]

$$\rho = \rho_0 + \chi \left(e^{\frac{E_{ph}}{k_B T}} - 1 \right)^{-1} \tag{1.11}$$

where χ is the coupling strength of the phonon mode to charge carriers in the graphene and E_{ph} is the energy of the considered phonon mode. ρ_0 decribes the residual resistance at $T = 0$ K.

An experimental example of remote-phonon scattering for graphene on SiC is shown in Figure 1.12. Jobst el al. find a residual resistance ρ_0 of about $400\ \Omega$ and $\rho(T = 300\ \mathrm{K}) - \rho_0 \approx 500\ \Omega$ [9]. These numbers are questioned in section 4.2.

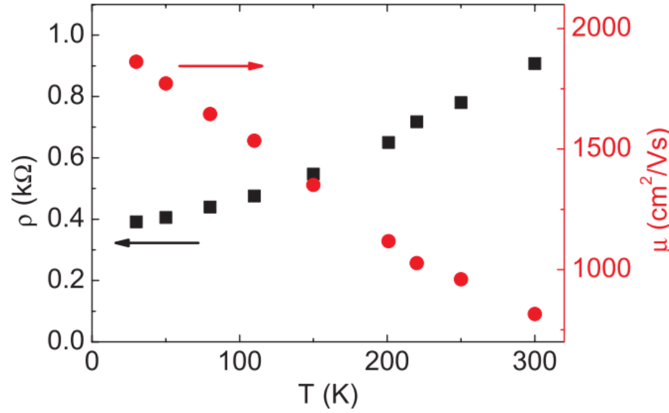

Figure 1.12 Temperature dependence of the sheet resistance in graphene on SiC attributed to electron-phonon scattering. Reprinted figure with permission from Jobst *et al.* Quantum oscillations and quantum Hall effect in epitaxial graphene. *Phys. Rev. B* **81**, 195434 (2010) [9]. Copyright (2010) by the American Physical Society.

1.5.3 Finite Transmission in Graphene at SiC Substrate Steps

Besides diffusive scattering processes in the sense of electron-electron interaction or electron-phonon interaction, scattering at localized defects plays an important

role as discussed in section 1.5.1. However, the average scattering time τ introduced in the Drude model does not describe electron transport across a defect, because localized defects cause a drastic change in the electronic structure and give rise to a localized scattering potential. This was realized by Landauer in 1957 in his description of electron transport in the vicinity of a localized defect [81].

Generally, when charge carriers pass a localized scatterer, backscattering occurs resulting in an accumulation of charge in front of the scatterer and a depletion behind it. In other words, a dipole forms referred to as Landauer residual resistivity dipole [81].

This dipole induces an electric field and changes the chemical potential μ, which describes the energy that is needed to add an electron to the system in the absence of an external electrostatic field. The electrochemical potential μ_{ec} defined in equilibrium

$$\mu_{ec} = \mu - e\phi, \tag{1.12}$$

captures both changes. Charge transport across a localized scatterer results in a change in the electrochemical potential.

If a system is not in thermodynamic equilibrium, strictly speaking neither the chemical potential nor the electrochemical potential is defined. In order to be able to describe charge transport spatially resolved, these quantities are transformed into local quantities $\mu(x)$ and $\mu_{ec}(x)$. The idea behind this is to divide the entire system into small areas in which the equilibrium state can be approximated locally [82]. Under the condition of stationary time-independent states, a local electrochemical potential can be defined [83]

$$\mu_{ec}(x) := \mu(x) - e\phi(x) \tag{1.13}$$

This definition of the local electrochemical potential is the basis for the description of charge transport on the local scale as in the case of scanning tunneling potentiometry (section 2.3.1).

The concepts of the Landauer residual resistivity dipole find application in the context of monolayer bilayer transitions and also for SiC substrate steps [84]. Ji et al. first demonstrated this by mapping the associated step resistance of SiC substrate steps in graphene using scanning tunneling potentiometry [85]. Moreover, they find a linear dependence of this step resistance on the step height [85].

Detailed considerations and calculations of the step resistance in graphene on SiC were carried out in 2012 by Low et al. [86]. In their work, they investigate two possible causes for the step resistance in monolayer graphene, firstly, the influence of the curvature of the graphene layer across the step and resulting strain and, secondly, a change in the electronic coupling of the graphene and the substrate.

The basic mechanism is that the graphene layer detaches from the substrate at the position of the substrate step. However, the resistance resulting from this deformation is <0.01 $\Omega\mu m$ and, thus, cannot be the main cause of the experimentally observed step resistances in the range of 5-10 $\Omega\mu m$. If strain in the graphene layer

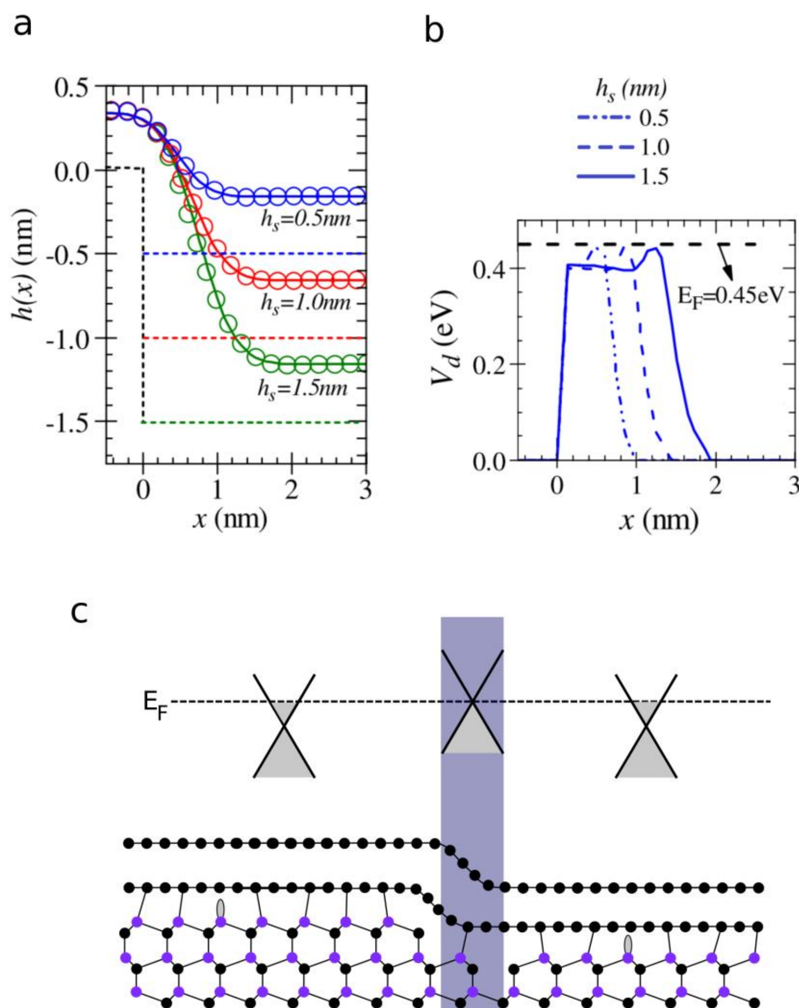

Figure 1.13 Step resistance according to Low et al. [86] (a) graphene geometry for different step heights and (b) corresponding potential profile. Reprinted figures with permission from Low, Perebeinos, Tersoff & Avouris. Deformation and scattering in graphene over substrate steps. *Phys. Rev. Lett.* **108**, 096601 (2012) [86]. Copyright (2012) by the American Physical Society. (c) Schematic illustration of the charge carrier depletion at the position of the SiC substrate step.

is included in the calculations, the resulting step resistance is still <1 $\Omega\mu m$. According to Low et al. the dominant contribution to the step resistance stems from an electronic coupling between the graphene and the substrate: the detachment of the graphene layer from the substrate results in a local change of the doping at the position of the substrate step (see Figure 1.13).

Figure 1.13a shows the calculated detachment of the graphene layer over the substrate step, which can be described with an analytical function of the form

$$h(x) \approx -\frac{h_{step}}{2}\left[\mathrm{erf}\left(\frac{x - x_s}{d_s}\right) + 1\right] + h_{eq}, \tag{1.14}$$

where h_{step} is the step height of the substrate step, h_{eq} is the equilibrium distance between graphene and substrate, and x_s and d_s are step height-dependent parameters [86]. Away from the substrate step, the graphene layer is at an equilibrium distance from the substrate and shows a strong n-type doping (as discussed in section 1.3.1). However, at the position of the step, the graphene detaches, the distance between the graphene and the substrate increases, and the doping induced in the graphene layer decreases significantly.

Table 1: Review of published step resistances for substrate steps in graphene on SiC. For comparability, all step resistances are normalized to a step height of 250 pm based on the linear dependence of the step resistance on step height.

Publication	Normalized defect resistance $[\Omega\mu m]$
Clark et al. [87]	1.2
Willke et al. [80]	3.6
Ji et al. [85]	3.9 / 4.0
Ciuk et al. [88]	4.8 / 6.8
Willke et al. [89]	7.8

Figure 1.13b shows that the graphene layer is indeed almost completely depleted of charge carriers at the position of the step, resulting in an almost box-shaped scattering potential, which becomes wider as a function of increasing step height. The charge carrier depletion at the position of the substrate step is sketched in Figure 1.13c. The linear dependence of the step resistance on the width of this scattering potential and, thus, on the step height is due to the band structure of

graphene, which causes a pseudo-diffusive behavior in the depleted region [86]. Note that it remains to be questioned whether the concept of pseudo-diffusive behavior is applicable on the local scale.

In Table 1, based on [68], a summary of published results on step resistances in graphene on SiC is provided. Although the different studies show a qualitative agreement, the extracted values differ quantitatively. This aspect will be investigated in detail in section 6.2.

1.5.4 Current Density Simulations

The assumption of a homogeneous current density may be justified for some sample systems, but this cannot be assumed a priori for graphene on SiC even in very simple sample geometries. It is known, e.g., that monolayer-bilayer boundaries show a rather large defect resistance [84,85] and, thus, induce local variations in the current density. For this reason, simulations were carried out with the aim of quantifying current density variations and, thus, ultimately enabling quantitative local transport measurements.

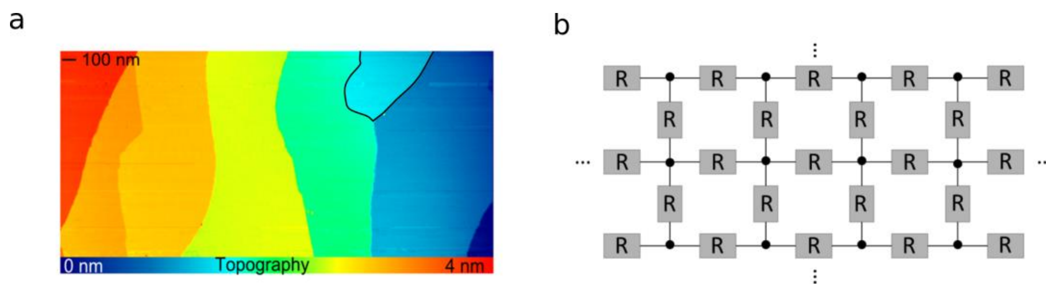

Figure 1.14 The current density calculations are based on modeling a (a) large-scale constant current topography ($V_{Bias} = 0.5\ V, I_T = 0.03\ nA$) using a (b) resistive network. The area marked with black lines in (a) is monolayer graphene just like the rest of the depicted sample surface. In order to determine the influence of a bilayer on the homogeneity of the current density, this region is first considered as a monolayer in the simulations and then assumed to be a bilayer. Graphic adapted from Sinterhauf et al. [33] licensed under CC BY 4.0.

To this end, finite element analysis was applied using the commercially available software package COMSOL multiphysics and the additional AC/DC Module. The main idea of these simulations is to model the surface morphology by a network of resistors (see Figure 1.14) and to calculate the current density using this resistor network [90]. Dirichlet boundary conditions can be used for the horizontal edges of

the simulation domain [90], and the right and left edges of the simulation domain are defined as terminal and ground, respectively.

As input parameters for the calculation of the current density, the macroscopic ohmic resistance and the global geometry of the sample, as well as additional topographic information like substrate steps, bilayer regions, and corresponding monolayer-bilayer transitions are included according to the structural information from constant current topographies. Step resistances are set to $6\,\Omega\mu\mathrm{m}$, $12\,\Omega\mu\mathrm{m}$, $18\,\Omega\mu\mathrm{m}$ for single, double, and triple substrate steps, respectively [33].

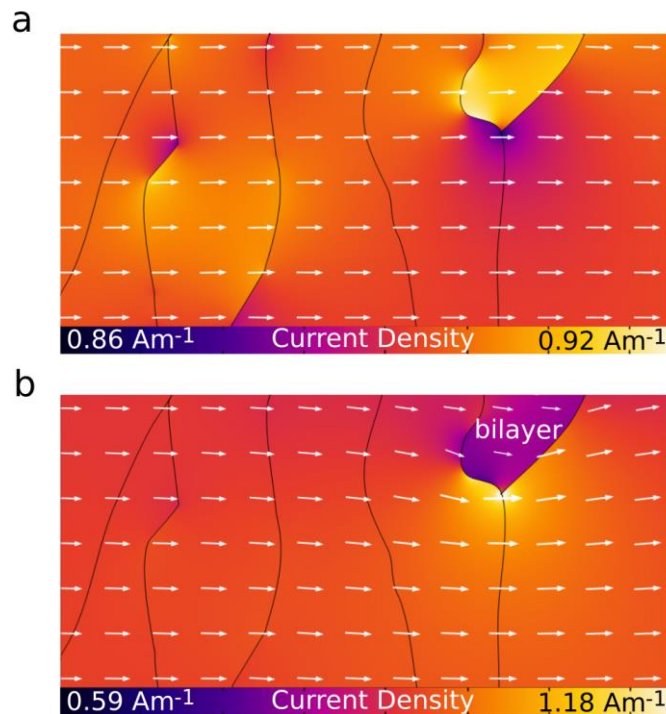

Figure 1.15 Influence of bilayer regions on the homogeneity of the current density. (a) local current density $j_{\mathrm{local}}(x, y)$ is calculated based on finite element simulations using COMSOL for a perfect monolayer grown by PASG. Arrows show current density as a vector plot. (b) for comparison, a bilayer region with corresponding monolayer-bilayer transition is included with otherwise fixed parameters. The increase by almost a factor of 10 in the quantitative local variations of the current density is clearly visible when comparing the color scales. Graphic adapted from Sinterhauf et al. [33] licensed under CC BY 4.0.

The resulting current density of the pure monolayer constant current topography (CCT) in Figure 1.14a is shown in Figure 1.15. It is rather homogeneous with variations in the range of $0.86\,\mathrm{A/m}$ to $0.92\,\mathrm{A/m}$ for a bias voltage of 1V (see Figure 1.15a). In order to estimate the impact of a small bilayer patch with corresponding monolayer-bilayer transition with a defect resistance of $25\,\Omega\mu\mathrm{m}$, a small bilayer

patch is added as indicated in Figure 1.15b. As a result, the local current density becomes highly inhomogeneous, showing an increase by almost a factor of 10 in its quantitative local variations.

These calculations illustrate the need for homogeneous samples, e.g. without bilayer areas, in order to be able to conduct quantitative local transport measurements. Further details on this topic will be addressed in 4.2.2.1.

2 Experimental Methods

This section introduces the theoretical background and basic concepts of the experimental techniques that have been applied in the experimental sections 3, 4, 5 and 6. In this context, the present thesis mainly relies on scanning tunneling microscopy (STM) (section 2.1.1), additionally, the related method of atomic force microscopy (AFM) is used (section 2.1.2). In order to connect the structural information with the electronic properties, we employ scanning tunneling spectroscopy (STS) (section 2.2.1). The tool of Kelvin probe force microscopy (KPFM) is introduced in section 2.2.2. In section 2.3 we turn to methods capable of determining the local transport properties. In this context, the most important method for this thesis is scanning tunneling potentiometry (STP), which we cover in section 2.3.1. Furthermore, an extension of KPFM for transport measurements is presented in section 2.3.2. This section ends with an introduction of the STM setup as well as the electronics in section 2.4.

2.1 Structural Analysis

In view of the 2D nature of the graphene sample system, the approach to characterize this material system by means of microscopy methods is rather obvious as in this case, and contrary to bulk materials, microscopy methods can yield a comprehensive picture of the sample under investigation. In very early experimental studies on graphene it has already been shown that monolayer graphene prepared by the scotch-tape method on a suitable substrate such as SiO_2 can be quickly and easily identified by optical microscopy based on the characteristic interference contrast [37].

In addition to optical microscopy, many other surface characterization tools are available and have been used to study graphene. Some examples include electron diffraction [57], electron microscopy [91,92], photoemission [93], x-ray diffraction [94], and scanning probe tools [62]. The zoo of different methods differs in the way the individual method interacts with the sample (e.g., excitation by photons, electrons, or ions), as well as in whether the technique provides information in real space or in

reciprocal space. For some techniques, it is even possible to switch between the different images in real space or reciprocal space. An example of this is low energy electron microscopy (LEEM), which will be addressed in section 5.2. Despite the versatility of this method, a crucial drawback of LEEM in the context of this work is the lack of height information, which prohibits the assignment of SiC terminations to graphene terraces (as introduced in section 1.3 and applied in section 4.2) beyond doubt.

In scanning probe microscopy, this type of information is naturally included. In addition to the possibility of atomic-scale structural analysis, scanning probe microscopy offers various other measurement modes beyond topographic imaging allowing for a comprehensive analysis at a specific position on the sample regarding its structural as well as its electrical and transport properties.

2.1.1 Scanning Tunneling Microscopy

Scanning tunneling microscopy (STM) is based on the quantum mechanical effect called quantum tunneling, where an electron passes through a barrier that it could not overcome classically. In an STM, quantum tunneling is realized with a sharp tip that is brought very close ($< 1\mathrm{nm}$, as the tunneling current decreases exponentially with distance) to the surface of a sample. Applying a bias voltage V to the tunneling junction a current flows, which passes the vacuum barrier between tip and sample.

In the following, different approaches are shown to describe the tunneling current between tip and sample. Firstly, the Bardeen theory and secondly, the Tersoff-Hamann theory as well as the Hamers model are presented. For an in-depth introduction we refer to [95]. Finally, the constant current topography (CCT) imaging mode is introduced.

Bardeen Theory | A theoretical approach to describe electron tunneling is the time-dependent perturbation approach developed by Bardeen already in 1961 [95]. It is based on electron tunneling in metal-insulator-metal tunneling junctions. In this approach, the Schrödinger equations of the two subsystems, sample and tip, are solved separately. The tunneling current is then calculated from the overlap of the wave functions.

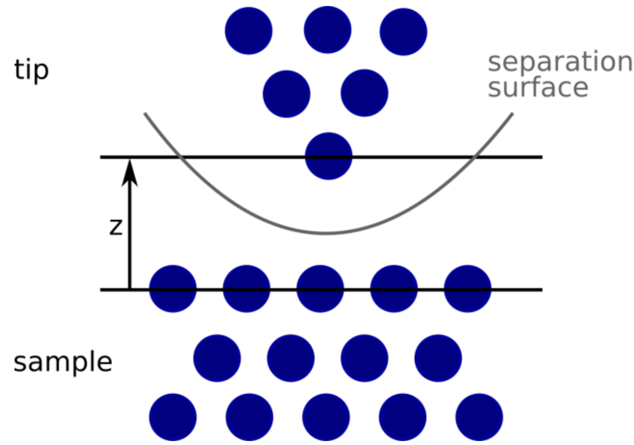

Figure 2.1 Bardeen theory for electron tunneling. Schematic of a tip sample system separated by the separation surface. Graphic inspired by [95].

Assuming a set of wave functions ψ and χ for sample and tip, respectively, the transition matrix element between two states μ and ν is given by

$$M_{\mu\nu} = \frac{\hbar^2}{2m}\int_{\mathbf{S}} \left(\psi_\mu \nabla \chi_\nu^* - \chi_\nu^* \nabla \psi_\mu d\mathbf{S}\right) \tag{2.1}$$

where $\mathbf{S}$ denotes the separation surface between tip and sample (Figure 2.1). The tunneling current, which is driven by a bias voltage V, can be written as follows

$$I_T = \frac{2\pi e}{\hbar}\sum_{\mu,\nu}\left[f(E_\mu) - f(E_\nu)\right]\left|M_{\mu\nu}\right|^2 \delta\left(E_\nu + eV - E_\mu\right). \tag{2.2}$$

Tunneling is only possible from occupied states to unoccupied states $\left[f(E_\mu) - f(E_\nu)\right]$ with the same energy regarding the applied bias voltage, which is ensured by the delta function. The transfer probability is given by the transfer matrix element $M_{\mu\nu}$. In the limit of low temperatures and small bias voltages, equation 2.2 can further be approximated by replacing the Fermi distributions with step functions resulting in [95,96]

$$I_T = \frac{2\pi e^2}{\hbar} V \sum_{\mu,\nu}\left|M_{\mu\nu}\right|^2 \delta(E_\nu - E_F)\delta\left(E_\mu - E_F\right). \tag{2.3}$$

Tersoff-Hamann Theory and Hamers Model | In 1983 Tersoff and Hamann introduced a new model based on Bardeen's theory of electron tunneling. In their approach, the tip was described as a spherical s-wave function with a radius of curvature R as shown in Figure 2.2.

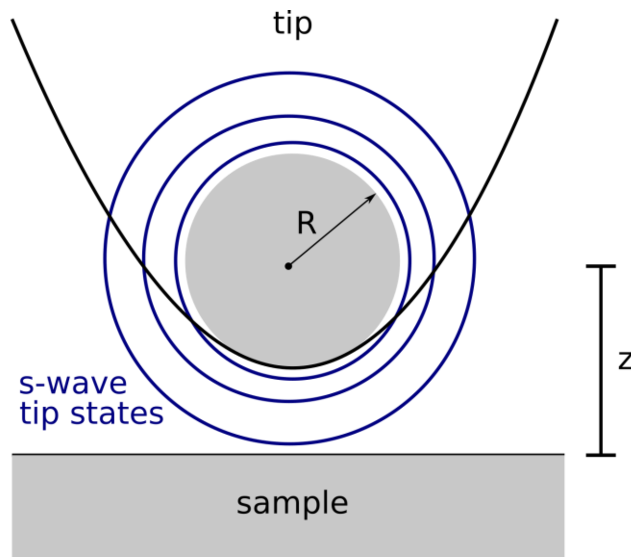

Figure 2.2 Tunneling junction in the theory of Tersoff and Hamann, tip modeled as a spherical potential well with radius of curvature R. Graphic inspired by [95].

For small bias voltages, the transfer matrix elements $M_{\mu\nu}$ in equation 2.3 can be assumed to be constant and, thus, the tunneling current in the model of Tersoff and Hamann can be expressed in a very simple form [95]. It is proportional to the applied bias voltage and the sample's local density of states (LDOS) $\rho_S(\mathbf{r}_0, E_F)$, where $\mathbf{r}_0$ denotes the center of the curvature of the tip. The tunneling current then reads

$$I_T = eV\rho_S(\mathbf{r}_0, E_F). \tag{2.4}$$

However, the assumption of constant transfer matrix elements does not hold for higher voltages. In this case, the Hamers model has shown to be useful, where the transfer matrix element is replaced by a distance- and energy-dependent transmission $T(E, eV, z)$. Equation 2.3 then reads

$$I_T \approx \int_0^{eV} \rho_S(E - eV, r)\, \rho_T(E) T(E, eV, z) dE \tag{2.5}$$

with the tip's LDOS $\rho_T(E)$ [97]. Using the Wentzel-Kramers-Brillouin approximation, the transmission can be written as

$$T(E) = \exp\left(-\frac{2\sqrt{2m}}{\hbar} \cdot \sqrt{\frac{\phi_S + \phi_T}{2} + \frac{eV}{2} - E} \cdot z\right), \tag{2.6}$$

where ϕ_s and ϕ_T represent the work functions of sample and tip, respectively. Equation 2.6 reflects the exponential decay of the tunneling current with distance z between tip and sample.

Constant Current Imaging | For acquiring so-called constant current topographies (CCT), a constant bias voltage V_{bias} is applied to the sample causing a tunneling current flow between tip and sample. By changing the height of the tip above the sample surface, I_T is adjusted to a certain setpoint value. The tip is scanned using piezo crystals that vary the spatial coordinates (x, y), and at each point the tunneling current is regulated by a closed feedback loop. Showing the tip height as a function of the spatial coordinates (x, y) yields the CCT in this specific sample region. However, it has to be kept in mind that this type of topographic imaging does not (necessarily) show the topographic surface structure. For a flat and topographically featureless sample, the CCT might still show spatial modulation as it captures contours of a constant integrated LDOS in the range of $[0, eV]$ at a certain distance from the sample, which can be seen by recalling equation 2.5. If the surface structure is not flat and featureless, but exhibits height variations, a non-trivial superposition of the spatial height variations and the spatial changes of the electronic properties of the sample surface is measured. CCT measurements form one of the core parts of this work and are used in sections 4 and 6 to analyze the structural properties of PASG graphene on the nanoscale.

2.1.2 Atomic Force Microscopy

Atomic force microscopy (AFM), just like STM, is a scanning probe method. However, in contrast to STM, the important quantity in AFM is the force interaction between tip and sample. In order to obtain an image of the surface of the sample, the tip (mounted on a cantilever) is brought very close to the surface. Different forces act on the tip resulting in a deflection of the cantilever. This deflection is measured with the help of a laser, which is reflected by the cantilever and then detected by a photodiode (Figure 2.3). In order to obtain spatially resolved information, the tip is scanned over the sample by using piezo elements keeping a control variable (e.g. the deflection of the cantilever) constant using a feedback loop [98].

At large distances, the interaction between tip and sample is typically dominating by attractive Van der Waals forces, whereas in close proximity to the sample, Pauli repulsion is strongest. The interaction between these two contributions is described by the Lennard-Jones-potential. However, the method of AFM is not limited to these types of tip sample interaction, any kind of force that is able to change the oscillation of the cantilever can be measured [99].

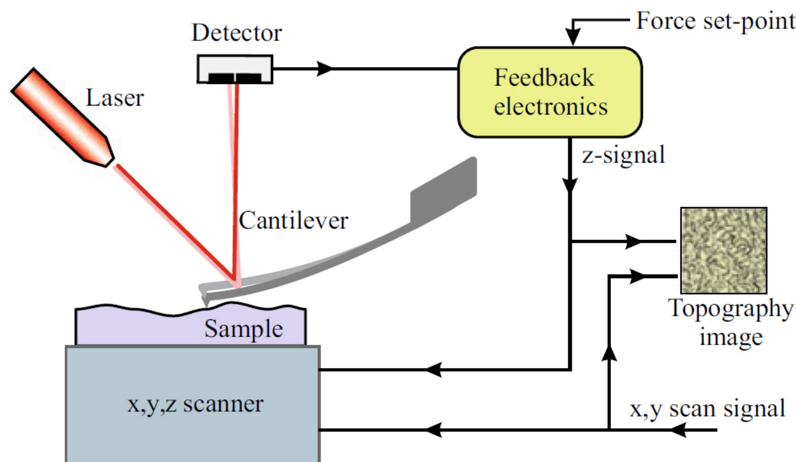

Figure 2.3 Schematics of an AFM setup operating in static mode. Preprinted by permission from Springer Nature, Atomic force microscopy by B. Voigtländer [98]. Copyright (2019) by Springer Nature.

Generally, in AFM one differentiates between static (contact mode) and dynamic (non-contact, intermittent contact mode) measurement methods. In static mode, the deflection of the cantilever is measured directly via the deflection of the laser, whereas in dynamic modes the cantilever is excited to oscillate near its resonance frequency and changes in the oscillation frequency, phase or amplitude are detected [99]. In this thesis, the standard measurement mode for topographic imaging is the tapping mode.

Tapping mode AFM | In tapping mode, also referred to as intermittent contact mode, the cantilever is excited to oscillate with a large amplitude such that the tip periodically touches the sample. The cantilever is excited to oscillate at a defined frequency and amplitude. The interaction with the sample leads to a shift in the oscillation frequency shift, which in turn results in a change of the oscillation amplitude. By adjusting the distance of the tip from the sample surface, the oscillation amplitude is kept constant. A topographic image is obtained by mapping the readjustment of the distance between tip and sample as a function of position. This

measurement mode is called AM-AFM, because the control parameter is the amplitude. It is used in section 3.2 for an in-depth analysis of the step sequence of PASG graphene.

2.2 Analysis of Electronic Properties

One of the standard methods for characterizing the electronic properties is probably angle-resolved photoemission spectroscopy (ARPES). This method gives direct access to the band structure of a material averaged over a rather large sample area. Using ARPES, e.g., the linear dispersion of graphene was experimentally demonstrated [93].

In this work, a real-space approach to the electronic properties of graphene is chosen based on the methods of STM and AFM. The advantage of this is that the electronic properties can be resolved locally and linked directly to the structural properties. In the context of STM, the most commonly used method for electronic structure analysis is scanning tunneling spectroscopy (STS), which provides access to the energy-resolved density of states with the lateral resolution of an STM. Details on this are provided in section 2.2.1. Moreover, based on AFM, Kelvin probe force microscopy (KPFM) gives access to local changes in the work function of a sample (section 2.2.2).

2.2.1 Scanning Tunneling Spectroscopy

Rewriting the derivative of equation 2.5 in the limit of low temperatures and assuming a constant transmission probability T as well as a constant tip local density of states (LDOS) ρ_{T} yields [97]

$$\frac{\mathrm{dI_T}}{\mathrm{dV}}(\mathrm{V}) \propto \rho_{\mathrm{S}}(\mathrm{eV}). \tag{2.7}$$

Thus, the differential conductance measured in STS is proportional to the LDOS of the sample.

Due to the assumption of, e.g. a constant tip LDOS, the absolute value of STS measurements is often complicated to interpret. For this reason, it is often useful to compare different STS features qualitatively.

In order to determine the differential conductivity, the topography is first adjusted at each measurement point at a fixed tunneling current I_T and bias voltage V_{bias} and then the differential conductance is recorded at each measurement point individually. The $\frac{dI_T}{dV}(V)$ spectra can be obtained numerically by deriving $I_T(V_{bias})$-curves, or by using lock-in technique. In this thesis, spectroscopic measurements are carried out by lock-in technique. Details on the implementation are given in [100].

2.2.2 Kelvin Probe Force Microscopy

Kelvin probe force microscopy is an AFM-based imaging mode, which measures the so-called contact potential difference between tip and sample that is reflected in an electrostatic force between the two. When a conductive tip is brought in close contact with a conductive sample, the Fermi levels of tip and sample align and it holds for the contact potential difference

$$V_{CPD}(x, y) = \frac{1}{e}\left[\phi_{tip} - \phi_{sample}(x, y)\right] \tag{2.8}$$

where e is the elementary charge and ϕ_{tip} and ϕ_{sample} denote the work functions of the tip and the sample, respectively [80,101]. Thus, $V_{CPD}(x, y)$ is a measure for changes in the sample's work function. Although this quantity is difficult to interpret, in some cases it can provide indirect insight into the local electronic structure of the sample under investigation [102,103].

In the static case, V_{CPD} is determined by applying an external voltage V_{DC} between tip and sample such that the force resulting from the contact potential is nullified. Specifically, in our setup, the sample is grounded and the potential of the tip is varied. In the dynamic case, both a DC voltage as well as a small AC modulation are applied to the tip. The AC component creates an oscillating electrostatic force which excites the cantilever to oscillate. Tip and sample behave like a capacitor and the force between tip and sample can be written as

$$F = \frac{1}{2}\frac{dC}{dz}V^2 \tag{2.9}$$

where C is the capacity. Using lock-in technique, different components of the force can be detected separately.

The electrical excitation can either be measured in amplitude modulation mode (AM-KPFM) or in frequency modulation mode (FM-KPFM). In the latter case, the signal is proportional to the gradient of the force between tip and sample. According to Zerweck et al., of these two modes, the FM-KPFM mode provides more quantitative results [104]. In this thesis, both modes were compared on graphene on Ge/Si(001) with the result that the FM-KPFM mode provides better resolution in V_{CPD} in agreement with [104]. It was even possible to resolve the fingerprint of the individual topographic facets of graphene on Ge/Si(001) (compare Figure 1.4) in the KPFM map in Figure 2.4. The FM-KPFM mode was used in section 5 for the analysis of work function changes of PASG graphene.

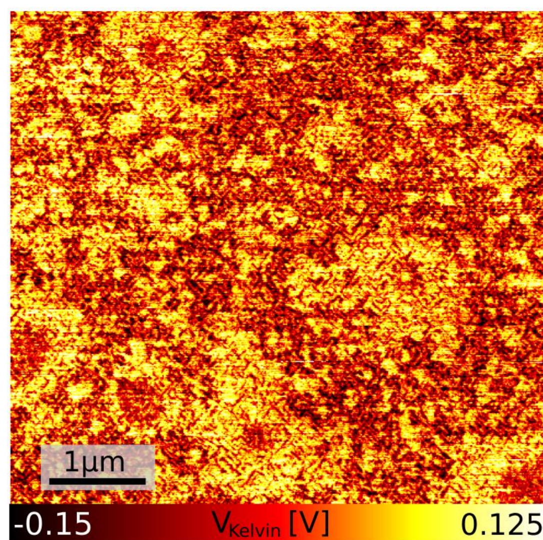

Figure 2.4 FM-KPFM map of work function changes of graphene on Ge/Si(001).

2.3 Transport Properties on a Local Scale

A well-established method for the determination of local transport properties is the nano 4-point probe method (N4PP) measurements presented in section 3 were conducted in the group of Prof. Tegenkamp in Chemnitz. Based on the idea of using 4 probes as in classical 4-point measurements to avoid the problem of contact resistance in resistivity measurements [105], four STM tips are placed in a square arrangement with a defined distance to each other as shown in Figure 2.5. The tip positioning is done by means of an integrated scanning electron microscopy setup. Two of the tips conduct a current through the sample, the remaining tips are used to measure the potential. In this way, it is possible to determine quantities such as the sheet resistance or the anisotropy.

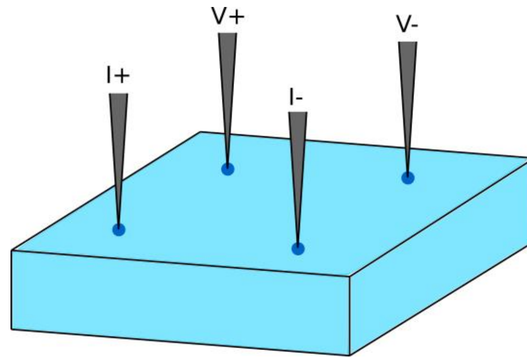

Figure 2.5 Schematics of a N4PP setup for mesoscopic transport measurements. For tip positioning, an integrated SEM setup is used.

N4PP measurements are an excellent tool for anisotropy measurements down to the scale of the minimum tip spacing of a few 100 nm. Combining N4PP with scanning tunneling potentiometry, which is able to differentiate between diffusive and localized scattering processes [90], allows for a comprehensive characterization from the mesoscopic to the local scale.

2.3.1 Scanning Tunneling Potentiometry

Scanning tunneling potentiometry (STP) is a tool that connects the local transport properties, i.e. the local potential, to the topographic information on the nanoscale. The idea of STP is to measure the electrochemical potential μ_{ec} locally in the sense that was defined in equation 1.13 in section 1.5.3 with the resolution of an STM. This is achieved by using the tip as a non-invasive voltage probe to measure μ_{ec} at a defined tip height. The method of STP has been suggested and experimentally implemented in 1986 by Muralt and Pohl [106].

In our setup, the samples are ex-situ contacted with two gold contacts in a shadow mask procedure such that an additional bias voltage V_{cross} can be applied, see Figure 2.6. This additional voltage induces an electric current in the sample. The measurement of the local potential is realized by switching off the bias voltage V_{bias} at a fixed tip height defined by the setpoint current, and applying a variable voltage V_{STP} to the tunneling junction such that no tunneling current flows. For $I_T = 0$, tip and sample are locally on the same potential in the sense that the measurement procedure defines the local electrochemical potential $\mu_{ec}(x, y)$ of the sample in terms of a non-equilibrium quantity as introduced in section 1.5.3. The adjustment

of the voltage V_{STP} is done at every position (x, y) and recorded in a map, the STP map, also called potential map.

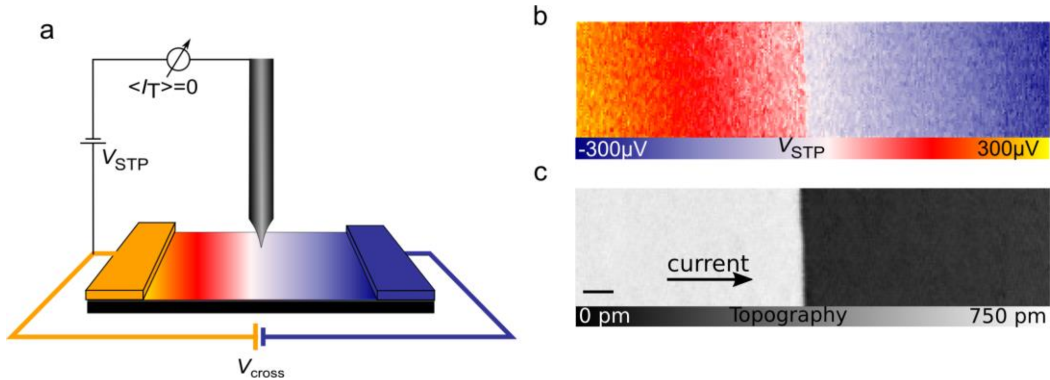

Figure 2.6 Working principle of the STP setup**.** (a) Sketch of the STP setup, the bias voltage V_{bias} is switched off at every position (x, y) and the tunneling current is nullified $I_T = 0$. The required voltage V_{STP} is recorded and mapped as a function of position. (b) Potential map and (c) corresponding $(200 \times 50)\ nm^2$ topography (imaging conditions: $V_{Bias} = 0.03\ V, I_T = 0.15\ nA, j = 3.56\ Am^{-1}$) of monolayer graphene on SiC crossing a triple substrate step. The scale bar is 10 nm. Graphic taken from Sinterhauf et al. [33] licensed under CC BY 4.0.

In addition to the electrostatic transport field, thermovoltage contributes to the tunneling current in STP measurements. Thermovoltage can be seen as a microscopic analogue to the thermoelectric Seebeck effect, which describes the diffusion current that emerges in a circuit of conductors of different materials driven by a temperature gradient. In an STM tunneling junction, thermovoltage occurs due to the temperature difference between tip and sample [96]. For symmetric transport ($V_{Cross}^{+} = -V_{Cross}^{-}$), the pure transport signal can be reconstructed from measurements of reverse current directions [84,96].

2.3.2 Kelvin Probe Force Microscopy for Transport Measurements

Based on KPFM, charge transport studies are feasible by extending the setup with the possibility to apply a voltage V_{Cross} across a sample [80,101]. If $V_{Cross} \neq 0$, the evolution of the electrostatic potential across the sample superimposes on V_{CPD} introduced in section 2.2.2. Similar to the cancellation of the thermovoltage in STP measurements, also here the transport signal can be determined from measurements of reverse current direction. The validity of this reconstruction method has been demonstrated for charge transport in graphene on SiO_2 [80].

This type of extension of the KPFM setup for charge transport measurements has been used in this thesis to study charge transport in Au-contacted graphene on Ge/Si(001) in a comprehensive manner [46]. Thereby, we could reveal a significant influence of the two materials Au and Ge in close proximity to the graphene sheet on graphene's transport properties.

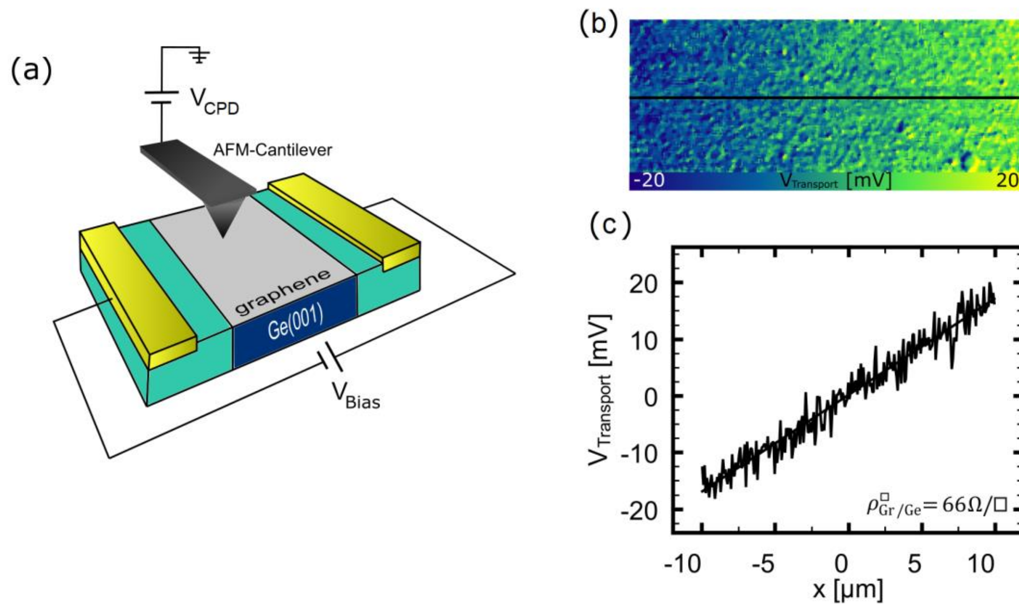

Figure 2.7 (a) Extension of a (commercial Agilent 6500LS) AFM operating under ambient conditions for transport measurements. The graphene on Ge is contacted with two gold contacts. Each one is connected to a voltage supply operating in the range of ± 10 V. The inversion of the polarity of the voltage is necessary to induce opposite current flow through the sample. In addition, the macroscopic current is measured in series. (b) Transport map of pristine graphene/Ge/Si(00) (c) from which the local sheet resistance of pristine graphene/Ge/Si(001) is extracted. Graphic adapted from Sinterhauf et al. [46] licensed under CC BY 4.0.

2.4 Experimental STM Setup

STM experiments, where a sharp metal tip is brought very close to a sample surface, require high stability of the tunneling junction and precise spatial positioning. In the framework of this thesis, experiments have been conducted in two different home-built STM setups operating at base pressures $\approx 5 \cdot 10^{-11}$mbar. The STM setups are designed in a modified beetle type originally developed by Besocke [107]. Details of our STM setup can be found in [90].

The heart of our design consists of four tube piezos. Three of these piezos are arranged in a triangle around the sample support. On top of each piezo there is a sapphire ball supporting the STM head including the tip, the fourth piezo used for z-movement, and a ramp. The tips are fabricated of a polycrystalline tungsten wire with a diameter of 250µm, which is electrochemically etched, in-situ annealed, sputtered with Ar^+-ions and characterized by field emission. By applying specific voltages to the tube piezos, the entire STM head slides up or down the ramp on the sapphire balls. This movement causes a change in tip height and is called slip-stick-movement. Movement of the tip (and therefore of the entire STM head) in x- and y-direction is also realized with the three tubes piezos. In order to apply a bias voltage between tip and sample, as well as a cross voltage across the sample for transport measurements, the sample support consists of six segments, which are electronically separated. The entire STM head is mounted at the bottom of a liquid helium cryostat operating at a temperature of 8K. In addition to low-temperature measurements, it is feasible to operate the very same setup using liquid nitrogen cooling (77K) or even without cooling at room temperature.

To achieve atomic resolution as well as stable and low-noise potentiometry measurements, precisely working electronics play an important role. The electronic setup developed and used in our group over the last years is shown in Figure 2.8. On the sample side, the bias voltage is applied using a 16-bit digital-analogue-converter (DAC). Our setup is equipped with a second and identical DAC, which is

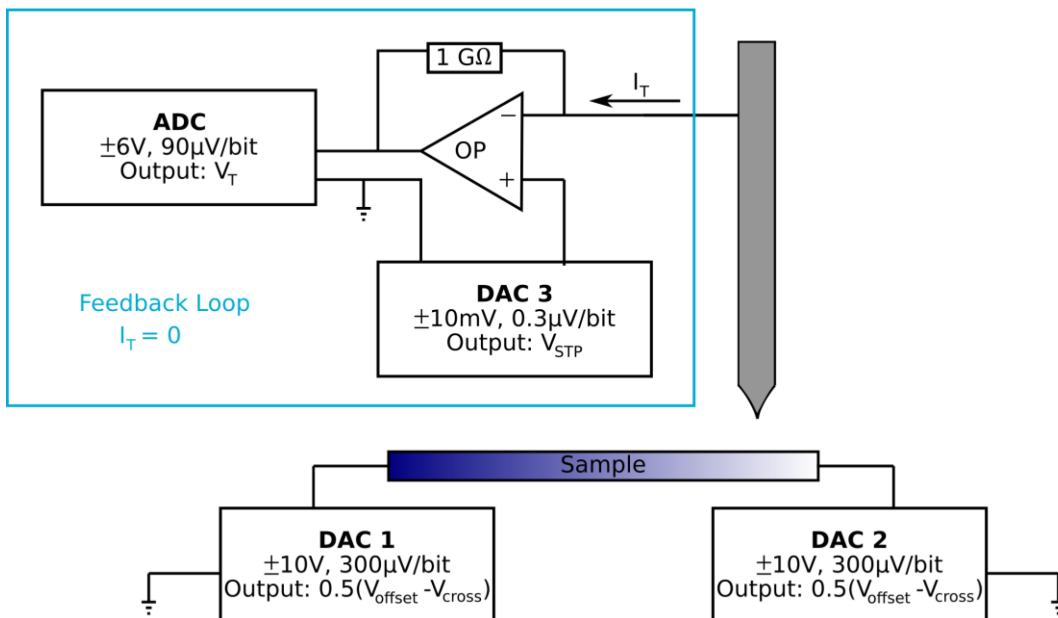

Figure 2.8 Electronic circuit for an STP experiment with microvolt resolution implemented in a standard STM electronics. In our setup, we use 16-bit DACs.

controlled separately so that the two DACs can be set to different values. This peculiarity of the electronic setup becomes particularly important for STP measurements. The DACs can drive a current with a resistance of roughly 200Ω, for higher currents additional current amplifiers are implemented. On the tip side, the tunneling current is converted by an I/V converter and then passes a 16-bit analogue-digital converter (ADC) before it is fed into the topographic feedback loop, which calculates the z-position of the tip. For potentiometry measurements, also on the tip side an additional DAC is needed as shown in Figure 2.8. A voltage V_{STP} is fed into the non-inverting input of the I/V converter and the potentiometry feedback loop modifies this voltage until it cancels out the tunneling current. Details and performance limits of the STP setup are given in [108].

3 Charge Transport in Graphene from Mesoscopic to Microscopic

Anisotropy of a solid describes that this solid shows different properties along different crystallographic axes. The anisotropy is therefore an important parameter to characterize a solid in its entirety and is, e.g., important in the context of magnetoresistance [109]. In the case of graphene, anisotropic behavior is observed, e.g., for excitation and relaxation of photo-generated charge carriers [110], or in friction force microscopy [111].

The anisotropy of a system also plays an important role in the description of the electrical resistance. Usually, this quantity is determined by rotational square measurements based on N4PP methods. Due to the finite spacing of the 4 probes, such measurements provide a mesoscopic picture of the conductance. In order to understand the conductance of a system and its anisotropy, it is often important to distinguish between the different contributions to the resistance and to analyze them individually. A beneficial approach is the combination of macroscopic / mesoscopic and local transport measurements. Based on this, e.g., the macroscopic resistivity of the Si(111)($\sqrt{3} \times \sqrt{3}$)-Ag reconstruction could be unraveled. It is composed of diffusive electron-phonon and electron-electron scattering as well as localized scattering processes at step edges and domain boundaries [90,112].

In the following, we use this approach (a combination of mesoscopic rotational square measurements and local transport measurements) to understand the residual anisotropy of the resistance in high-quality graphene on SiC.

3.1 Author Contributions

In collaboration with G.A.T. and M. W., A.S. performed the STP measurements, analyzed the STP results, linked them to the results of the N4PP measurements and developed the model for $\mathrm{A_{STP}}$.

3.2 Minimum Resistance Anisotropy of Epitaxial Graphene on SiC

D. Momeni Pakdehi, J. Aprojanz, A. Sinterhauf, K. Pierz, M. Kruskopf, P. Willke, J. Baringhaus, J. P. Stöckmann, G. A. Traeger, F. Hohls, C. Tegenkamp, M. Wenderoth, F. J. Ahlers, H. W. Schumacher

ACS Appl. Mater. Interfaces **10**, 6039-6045, 2018

DOI: 10.1021/acsami.7b18641

Further permissions related to this material should be directed to the ACS.

We report on electronic transport measurements in rotational square probe configuration in combination with scanning tunneling potentiometry of epitaxial graphene monolayers which were fabricated by polymer-assisted sublimation growth on SiC substrates. The absence of bilayer graphene on the ultralow step edges of below 0.75 nm scrutinized by atomic force microscopy and scanning tunneling microscopy result in a not yet observed resistance isotropy of graphene on 4H- and 6H-SiC(0001) substrates as low as 2%. We combine microscopic electronic properties with nanoscale transport experiments and thereby disentangle the underlying microscopic scattering mechanism to explain the remaining resistance anisotropy. Eventually, this can be entirely attributed to the resistance and the number of substrate steps which induce local scattering. Thereby, our data represent the ultimate limit for resistance isotropy of epitaxial graphene on SiC for the given miscut of the substrate.

3.2.1 Introduction

Epitaxially grown graphene monolayers on SiC substrates have the potential to be used as a basis for future electronic applications [62,94,113]. The main advantage is the capability of waferscale graphene manufacturing directly on the insulating SiC substrate. Desirable for device fabrication is a high crystal quality over large areas with coherent electronic properties of the graphene layer. However, this is challenging for epitaxial growth. The substrate morphology, in particular SiC terrace steps, are known to strongly deteriorate the performance of graphene-based electronics, e.g., by limiting the geometry of devices, lowering the cutoff frequency in high-speed electronics [114], degrading carrier mobility [115] in FET devices [116,117] or leading to anisotropies in the quantum Hall effect (QHE) [118,119]. Rotational square

probe measurements have quantified a conductance anisotropy of about 70% for epitaxial graphene layers grown on the Si-face of 6H-SiC [120]. Other 4-terminal electronic transport measurements showed a pronounced resistance anisotropy of approximately 60% and even more than 100% for epitaxial graphene produced by sublimation growth (SG) methods and chemical vapor deposition (CVD), respectively [88,117]. In all cases, higher resistance values were observed for transport perpendicular to the SiC surface terraces, which indicates a correlation with the terrace step edges of the SiC substrate.

The impact of individual step edges of the substrate on the electrical resistance of the epitaxial graphene layer was investigated by various local scanning tunneling potentiometry (STP) studies which revealed an additional step-induced resistance contribution for charge carrier transport in monolayer graphene across the step edges [85,87,89]. Various physical scattering sources were discussed, e.g., detachment from the underlying substrate leading to a potential barrier, induced by a doping variation [86,89]. Also, local scattering by charge built up, graphene defects, as well as local strain at step edges, were addressed as potential origins [120–122]. Another more considerable contribution arises from the transition region between mono- and bilayer (ML–BL) graphene due to a wave function mismatch [84,85,123,124]. In particular, a ML–BL transition at a SiC step edge causes a significant increase in the local resistance. Moreover, magnetotransport measurements in bilayer-patched monolayer graphene showed that bilayers could cause anomalies in the quantum Hall effect [125]. The influence of bilayer regions on charge magnetotransport also depends on the bilayer position and its carrier density, which later determines the metallic or insulating behavior of the bilayer. Accordingly, magnetotransport in graphene can be interfered, either shunted by the bilayer or constricted through the monolayer graphene regions in case of metallic or insulating bilayer's characteristic, respectively [126]. This suggests that bilayers can have a substantial impact on the transport properties of graphene devices, and an impact on the resistance anisotropy is expected. Because the formation of bilayer graphene is very often observed at step edges higher than three Si-C bilayers [52,127] it is highly favorable to keep SiC step heights below 0.75 nm to prevent bilayer formation during epitaxial graphene growth.

In this study, we present the successful realization of such ultrasmooth monolayer graphene sheets on 4H-and 6H-SiC polytype substrates by the so-called polymer-

assisted sublimation growth (PASG) technique [11]. Rotational square probe measurements of the monolayer graphene reveal nearly vanishing resistance anisotropies of only about 3%. This value is in good agreement with the anisotropy determined from STP measurements at individual terrace steps. It can hence be regarded as the ultimate lower limit of resistance anisotropy only given by step induced resistance contributions. This study shows that nearly perfect resistance isotropy of epitaxial graphene sheets can be achieved by careful control of the growth conditions.

3.2.2 Sample Preparation

The growth of epitaxial graphene was performed on the Si-terminated face of SiC substrates ($5 \times 10\ \mathrm{mm}^2$) cut from semi-insulating 6H- and 4H-polytype wafers (nominally 0.06° toward $[1\bar{1}00]$), in the following referred to as sample S1 and S2, respectively. A low miscut angle of the wafer is an important prerequisite to obtain smooth graphene layers [11,52]. The epi-ready surface conditioning allows high-quality epitaxial growth without hydrogen pre-etching. A particular growth procedure was applied, including the PASG technique and special temperature ramps, as described in the following, see also Supplementary Information in section 3.2.6. Polymer adsorbates were deposited on the samples by liquid phase deposition from diluted isopropanol-photoresist (AZ5214E) introduced to an ultrasonic bath that was followed by a short isopropanol rinsing, see Ref. [11] for details. The subsequent high-temperature growth process was identically carried out on both polytype substrates in a horizontal inductively heated furnace [128]. Three initial annealing steps at lower temperatures of 900 °C (vacuum, 30 min), 1200 °C (Ar atmosphere, 900 mbar, 10 min), and 1400 °C (Ar atmosphere, 900 mbar, 2 min) were carried out before the graphene growth at 1750 °C (Ar atmosphere, 900 mbar, 6 min). After the vacuum annealing step, the samples were first allowed to cool to room temperature (no argon gas flow) for adjusting the pressure to 900 mbar by argon for the later graphene growth. This intermediate cooling for carbon condensation was introduced to increase the number of nucleation sites on the SiC surface for accelerated buffer layer growth.

For comparison, three other graphene samples (S3–S5) were used in this study, listed in Table 2. Graphene sample S3 was grown by conventional sublimation growth (SG) after preannealing in Ar atmosphere (1000 mbar) on a small miscut

6H-SiC substrate (≈0.06°) [127]. S4 is a PASG graphene sample on a 6H-SiC substrate with a large miscut angle of ≈0.37° [11]. The graphene of S5 was fabricated by sublimation growth on a hydrogen pre-etched 6H-SiC substrate [127]. The main parameters (1750 °C, ≈1 bar Ar atmosphere, 6 min) of the graphene growth were kept the same for all samples.

3.2.3 Results and Discussion

Surface Morphology | The atomic force microscopy (AFM) topography images of the graphene monolayers grown on 6H- and 4H-SiC substrates, samples S1 and S2, are shown in Figure 3.1a and d. The very smooth and homogeneous surface morphology is a typical result and can be found on the entire surface of the samples. This is confirmed by multiple AFM measurements at different positions in the center and near the edges of the samples, as well as by optical microscopy inspection throughout the surface. The corresponding histograms in Figure 3.1c and f are the results of AFM inspection of about 200 steps collected from 9 different positions on the substrates, including edge regions. For most of the terrace steps on both polytypes, we found heights below 0.75 nm.

Table 2: Samples used in this study and the results from AFM, N4PP measurements, and STP.

			AFM		N4PP				STP	
sample	SiC-polytype/ miscut	process	h_{step} (nm)	bilayer	R_0 (Ω)	ρ_{par} (Ω/sq)	ρ_{perp} (Ω/sq)	anisotropy ratio	anisotropy ratio	ρ_{sheet} (Ω/sq)
S1	6H/0.06°	PASG	0.25–0.75	no	68	629 ± 1	647 ± 1	1.03 ± 0.002	1.03 ± 0.02	570 ± 20
S2	4H/0.06°	PASG	0.25–1.0	no	67	611 ± 2	620 ± 2	1.02 ± 0.005	1.04 ± 0.02	615 ± 20
S3	6H/0.06°	SG	0.75	small	184	1755 ± 13	2046 ± 15	1.17 ± 0.01		
S4	6H/0.37°	PASG	0.75–3.5	scattered	112	1339 ± 39	2397 ± 56	1.79 ± 0.04		
S5	6H /0.37°	H_2/SG	3–15	extended	202	2121 ± 48	3531 ± 54	1.66 ± 0.03		

A closer inspection of the topography in Figure 3.1a reveals a regular and alternating sequence of terraces with a 0.25 nm high step in front of a terrace with 0.5 nm step-height for the 6H-SiC sample. This situation is depicted in the height profile of Figure 3.1b. The clear majority of the terrace steps (≈90%) exhibit such a sequential pattern and only occasionally (10%) steps with 0.75 nm height are observed, see the histogram in Figure 3.1c. Higher steps were not found, which confirms that step bunching is effectively suppressed by the PASG technique.

For the graphene on the 4H-SiC polytype, no such repeating sequence of steps is observed, Figure 3.1e. The step height histogram in Figure 3.1f. shows a different and somewhat wider height distribution compared to the 6H polytype. Although the majority (50%) of steps are 0.5 nm high as before, a smaller percentage (20%) of 0.25 nm steps and a higher proportion (25%) of 0.75 nm steps are measured. Here,

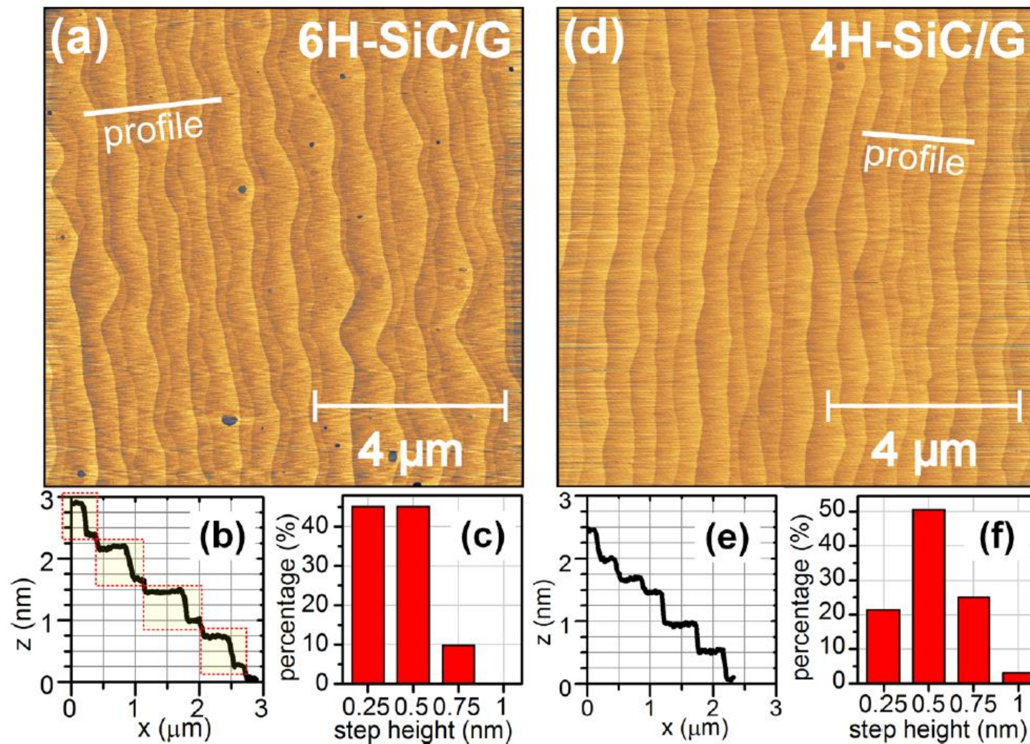

Figure 3.1 AFM measurements of monolayer graphene grown by the PASG method on 6H-SiC (sample S1) and 4H-SiC (sample S2). (a) Surface topography of S1. (b) Height profile along the profile line in panel a showing the pairwise sequence of 0.25 and 0.5 nm steps (marked by red dotted rectangles) typical when using 6H-SiC substrates. (c) Statistical evaluation of nine AFM images from the center, edges, and corners of the sample indicating the remarkable homogeneity all over the sample. (d) Surface topography of S2 using 4H-SiC substrates as well as (e) the corresponding height profile and (f) the step height distribution.

a tiny portion (≈3%) of 1 nm high steps is observed. Nevertheless, the high percentage (70%) of low steps with heights of 0.25 and 0.5 nm is remarkable and exceeds the results for conventional sublimation growth on 4H-SiC [52,129]. Such ultrasmooth graphene layers found on both SiC polytypes are a unique feature of the PASG technique. It is comparable to graphene layers grown on 3C-SiC(111) surfaces [52]. A second typical property of PASG graphene layers is the suppression of graphene bilayer formation which can be regarded as a result of the very low SiC step heights ≤0.75 nm, in agreement with Raman mappings [11]. The observed formation of the 0.25/0.5 nm step-pairs on the 6H-SiC substrate is related to the specific surface-energy sequence of the SiC bilayer planes of the 6H polytype. Surface restructuring and step bunching can be understood as retraction of Si-C bilayers with different velocities which are related to distinct terrace energies [52,130].

This retraction process is effectively slowed by the additional carbon supplied from the cracked polymer because the large area homogeneous carbon nucleation on the terraces accelerates the growth of the buffer layer whose covalent bonds to the SiC stabilizes the terrace structure [11]. This enables step bunching only for fast retracting Si-C bilayers, which can catch up a slower one before the surface topography is ‘frozen in’ by the buffer layer. For 6H-SiC, which has three distinct terrace energies per unit cell, this results in three different retracting velocities and finally to a periodic sequence of 0.25 and 0.5 nm steps. A similar pattern cannot develop on 4H-SiC surfaces which exhibit only two distinct terrace energies per unit cell [52,130]. However, it is evident that an overall reduction of the step heights is achieved by the PASG technique compared to SG growth on 4H-SiC substrates [11,129].

Resistance Anisotropy Measurement | The electronic properties of the graphene samples were investigated by angle-dependent nano four-point probe (N4PP) measurements in an Omicron UHV nanoprobe system [131]. The samples were kept in UHV at room temperature after a thermal cleaning procedure by heating up to 300 °C. The scanning tunneling microscopy (STM) tips were placed in a square arrangement with 100 μm spacing, and electrical current was flowing between two adjacent tips while the voltage drop was measured between the two opposite ones, Figure 3.2c. From the ohmic I-V-curves which were measured in the current range from −10 μA to +10 μA, the absolute resistance values R were calculated. The N4PP measurements were carried out for different angles between the direction of the current probes and the step edges. The angles of 0° and 180° (90°) correspond

to current flow parallel (perpendicular) to the steps, and R_0 denotes the averaged absolute resistance from the parallel (0 and 180°) measurements, see Table 2.

The measured resistances R_θ for a given angle θ are adequately described by

$$R_\theta = \frac{1}{2\pi\sqrt{\sigma_\parallel\sigma_\perp}} \times \ln\sqrt{\frac{(\sigma_\parallel/\sigma_\perp + 1)^2 - 4\cos^2\theta\sin^2\theta(\sigma_\parallel/\sigma_\perp - 1)^2}{(\sin^2\theta + \sigma_\parallel/\sigma_\perp\cos^2\theta)^2}} \quad (3.1)$$

and perpendicular to the step direction, respectively, assuming an anisotropic 2D sheet with different conductivities in x- and y-direction [132]. From the fitting procedure, finally the resistivity values perpendicular $(\rho_{\mathrm{perp}} = \sigma_\perp^{-1})$ and parallel $(\rho_{\mathrm{par}} = \sigma_\parallel^{-1})$ to the step edges are obtained [105], and the anisotropy ratio is calculated as $\mathrm{A} = \rho_{\mathrm{perp}}/\rho_{\mathrm{par}}$, see Table 2.

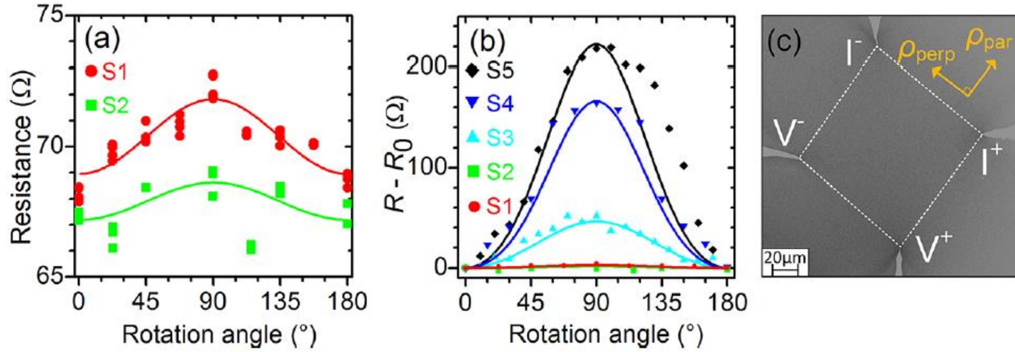

Figure 3.2 Results from rotational square probe measurements of five epitaxial graphene samples produced under different growth conditions, see Table 2. (a) Resistance variation as a function of the rotation angle for the PASG graphene sample S1 on 6H-SiC and S2 on 4H-SiC. (b) Anisotropy related resistance contribution $R - R_0$ as a function of the rotation angle of all five graphene samples S1–S5. The fitted curves (solid lines in a and b) are calculated by using a model for anisotropic 2D sheets, as explained in the literature [132]. (c) Schematic diagram of the rotational squared N4PP method. The SEM image shows the STM tips on a graphene sample for the N4PP measurement at a rotation angle of 90°.

Because the current flow via the semi-insulating SiC substrate and the buffer layer is negligible, the measured resistance is related to the 2D graphene sheet on top. For the applied rotational square method, it was shown that it is sensitive to both, a possible intrinsic anisotropy of the graphene, and additional superimposed effects (extrinsic anisotropy), e.g., step edges [132]. Due to the isotropic dispersion of the density of states near the Fermi level, an isotropic resistivity for graphene is expected [39,120]. Any measured anisotropy is therefore related to extrinsic effects.

Figure 3.2a shows the measured resistance R as a function of the rotation angle for the PASG graphene samples S1 and S2. A very slight resistance increase of a few Ohm is observed at angles around 90° which indicates that step related effects are noticeable also from these very flat surfaces. However, they are of minimal impact on the resistance anisotropy which is expressed by the obtained very small values of $\mathrm{A_{S1}} = 1.03$ and $\mathrm{A_{S2}} = 1.02$. This is underlined by the comparison to anisotropies of about 1.7 for epitaxial graphene growth in vacuum using H-etched SiC substrates [120]. To understand better the impact of the substrate preparation, N4PP measurements were performed on the other samples S3 and S4.

Figure 3.2b shows the anisotropy related resistance contribution $R - R_0$ as a function of the rotation angle of all samples S1–S5. The calculated curves and the experimental data agree very well except for S5, where higher resistance values for angles >110° are probably due to tip-induced defects.

The $R - R_0$ curves in Figure 3.2b show for samples S3, S4, and S5 an apparent maximum at an angle of 90°, which corresponds to transport perpendicular to the step edges. This indicates that step related sources are responsible for the extrinsic anisotropy in these epitaxial graphene layers. The resistance anisotropy increases to $\mathrm{A_{S3}} = 1.17$, $\mathrm{A_{S4}} = 1.79$, and $\mathrm{A_{S5}} = 1.66$, respectively. Thus, the values $\mathrm{A_{S1}}$ and $\mathrm{A_{S2}}$ of the PASG samples S1 and S2 can be regarded as practically isotropic, which verifies the assumption of an intrinsic isotropy of the graphene monolayer. This also demonstrates that extrinsic effects can be reduced to a level where they practically play no role when refined graphene growth procedures are applied as the presented PASG method on low miscut 4H- and 6H-SiC substrates. The N4PP measurements also show that the resistivity on the terraces is significantly reduced by the PASG method, which is demonstrated by the lower values of R_0 and ρ_{par} for S1, S2, and S4 compared to the other samples. Hall measurements show that this is due to an increased electron mobility, see Supplementary Information in section 3.2.6 and Ref. [11].

Local Resistance Measurements | The assignment of the very small resistance anisotropies of the PASG samples S1 and S2 to step related effects was further investigated by STM and STP measurements at room temperature, which give an insight into the local sheet resistance and the defect resistance induced by substrate steps [68,85,96].

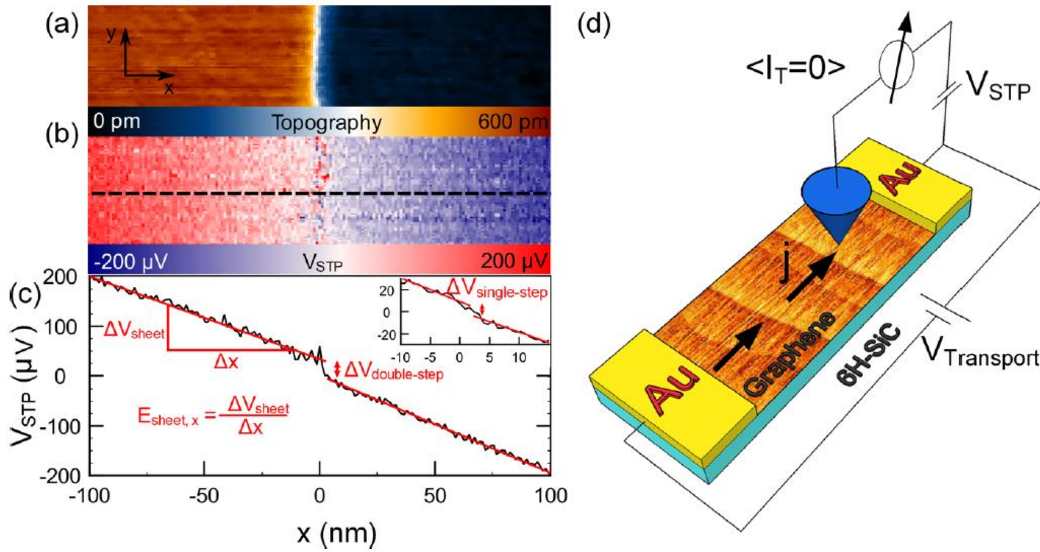

Figure 3.3 Scanning tunneling potentiometry inspection of step-induced resistance in epitaxial graphene on SiC. (a) Constant current topography of monolayer graphene sheet with a 0.5 nm step in the center, (tunnel conditions: I = 150 pA, $V_{bias} = 30\ mV$= 30 mV). (b) The simultaneously acquired potential map with an average current density of $j = 3.6\ A/m$. (c) The cross-section along the line in panel b, averaged over all potential values perpendicular to the dashed line in b. The local electric field component in x-direction $E_{sheet,x}$ is calculated from linear fits to the monolayer area (solid red lines in panel c). The step causes an additional local voltage drop $\Delta V \approx 36\ \mu V$. The inset represents the equivalent situation of a monolayer graphene sheet covering a single SiC-bilayer substrate step with a height of 0.25 nm. (d) Schematic of the setup of the scanning tunneling potentiometry experiment.

Figure 3.3a shows an example of a monolayer graphene sheet crossing a substrate step with a height of 0.5 nm which is located in the center (x=0 nm) of the STM topography image taken in an area of $200 \times 50\ nm^2$. The accompanied potential jump is clearly visible at the same position in the simultaneously acquired potential map plotted in Figure 3.3b. Figure 3.3c shows the averaged potential across the flat graphene monolayer regions and the substrate step, from which we deduced the local electric field $E_{sheet,x}$ in the x-direction[iii] as well as the voltage drop ΔV caused by the step. Using the macroscopic current density, we find an almost linear increase in resistances (details on the nomenclature can be found elsewhere [68]) with step heights: $\varrho_1 = (4 \pm 2)\ \Omega\mu m$, $\varrho_2 = (10 \pm 2)\ \Omega\mu m$ and $\varrho_1 = (13 \pm 2)\ \Omega\mu m$ for monolayer graphene crossing a substrate step with heights of

[iii] Analyzing the STP data, it was noticed that the sheet resistance to the left and right of a single or double substrate step is not identical, but shows deviations in the range of about 15% at room temperature. This issue will be investigated in a systematic study in section 4.

0.25 nm, 0.5 nm, or 0.75 nm, respectively, which is in good agreement with literature values [68,85,96]. The step resistance values are independent of the overall crystal morphology of the 4H- and 6H-SiC surface. The STP results can be compared with the N4PP measurements by setting the additional voltage drop at steps and their relative frequency c_i [#/µm] in relation to the electric field $\langle E_{sheet} \rangle$ on the terraces, accordingly, $A_{STP} = (\langle E_{sheet} \rangle + \sum c_i \langle \Delta V_i \rangle)/\langle E_{sheet} \rangle$, resulting in an anisotropy of 1.03 ± 0.02 for S1 and 1.04 ± 0.02 for S2. The good agreement with the anisotropy value close to 1.0 from the N4PP measurements demonstrates that we reached the ultimate lower limit where the resistance contribution of the substrate steps is the sole cause for the measured anisotropy.

Two implications follow from the linear relation between the step height and the local defect resistance at the step. When using SiC substrates with a same miscut angle, a similar step related resistance anisotropy value is expected because step density and step height can commensurate each other during the surface restructuring processes. A more significant anisotropy is expected for larger substrate miscut angles which increase the number of steps, its height, or both. These conclusions are valid if only step related resistances in monolayer graphene are considered. Additional extrinsic effects can cause higher resistances and larger anisotropies.

An important source for the resistance anisotropies of our samples S3–S5 is attributed to graphene bilayer domains. Local STP measurements have found that the electronic transition from monolayer to bilayer graphene results in an elevated resistance value which approximately corresponds to that of monolayer graphene over a 0.75 nm high SiC step [84,85,87,89]. Moreover, when the ML–BL transition is accompanied by a topographic height change, the resistance again drastically increases, e.g., by a factor of 4 at a 1 nm substrate step [85]. These bilayer-related local resistance increases can result in a macroscopic resistance directional dependency, according to the shape and distribution of the bilayer inclusions. Because the bilayer inclusions are not symmetric but show an elongated shape at terraces and are very often embodied as bilayer stripes along the terrace step edges, their presence results in a higher resistance for current flow perpendicular to the terrace step edges compared to current flow on the terraces parallel to the step edges.

For the graphene sample S3, a larger anisotropy (A_{S3} = 1.17) was obtained compared to S1 and S2 ($A_{S1,S2} \approx$ 1) although all were grown on low miscut substrates. As discussed above, this discrepancy is not clear if only step related contributions are considered. The additional resistance anisotropy is attributed to the scattered, micrometer-sized, asymmetric bilayer spots, which are located mainly at the terraces edges of sample S3, see Figure 1a, b in [127]. This comparison clearly shows that the nearly vanishing resistance anisotropy of the PASG samples S1 and S2 is related to the absence of bilayer graphene.

The significantly increased resistance anisotropy of the samples S4 and S5 compared to S1, S2, and S3 is expected because of the six-times larger SiC miscut angle. Under the assumption of a linear correlation between step height and step resistance, according to the above-mentioned STP anisotropy equation, one can estimate for pure monolayer graphene an anisotropy of $A_{STP} \approx$ 1.2. The measured anisotropy values of A_{S4} =1.79 and A_{S5} =1.66 are much higher and are attributed again to bilayer graphene on the terraces. Both samples show larger bilayer coverages compared to S3, and by taking into account the much higher step concentration in S4 and the giant step edges in S5, respectively, this should drastically increase ρ_{perp} and the anisotropy. On the other hand, the transport along the terraces can vary, e.g., caused by local planar ML-BL transitions. This is reflected by the higher ρ_{par} value of S5 compared to that of S4, which results in a smaller anisotropy value, $A_{S5} < A_{S4}$, although ρ_{perp} of S5 shows the highest value of all samples. This is probably due to the very high terrace steps in S5, which cause extensive graphene bilayer stripes along the upper side of the step edges.

3.2.4 Conclusion

In summary, we studied the resistance anisotropy in epitaxial graphene grown by different sample preparation and growth methods on 4H- and 6H-SiC(0001) substrates with small and large miscut angles. In agreement with STP measurements, the rotational square probe measurements reveal very small resistance anisotropies of ≈3% for graphene layers grown by PASG on SiC substrates with a small miscut angle. This anisotropy value is traced back to the step resistances of the monolayer graphene across the SiC steps measured by STP on the nanoscale. The main reason for the vanishing small resistance anisotropy was identified to be the absence of bilayer domains while the specific step resistances are similar to

other graphene. The PASG and fine growth optimization methods allow the uniform fabrication of ultrasmooth graphene with most of the terrace step edges being 0.5 nm or lower, which prevent the formation of graphene bilayer domains. In particular, on the 6H-SiC substrate, a very high percentage of 90% is achieved with a typical pattern of alternating steps of 0.25 and 0.5 nm in height, which is related to the SiC layer sequence in this polytype. This study shows that graphene growth using the PASG method and fine-tuning of the growth parameters bears the potential to reduce the terrace step heights down to an ultimate level of a single Si-C bilayer. Because SiC substrate steps cannot be entirely avoided, it is impossible to achieve perfect resistance isotropy for epitaxial graphene. However, for the produced bilayer-free graphene on ultralow terraces, negligible small deviations from isotropy can be obtained. In general, this study highlights the importance of bilayer-free graphene growth for all kinds of epitaxial growth techniques, whenever isotropic properties are demanded for perfect device performance. It makes the device orientation independent of step direction and improves the freedom for designing device layouts, thereby promoting the potential for future device applications of epitaxial graphene.

3.2.5 Acknowledgement

D.M.P. acknowledges support from the School for Contacts in Nanosystems (NTH nano). M.K. acknowledges support from the Braunschweig International Graduate School of Metrology (B-IGSM) and NanoMet. J.A. and J.P.S. thank the support from DFG project Te386/12-1, and P.W. acknowledges the support from DFG priority program 1459 Graphene.

3.2.6 Supplementary Information

Growth procedure | The graphene growth of samples S1 (6H-SiC) and S2 (4H-SiC) by means of the PASG method was performed by a special protocol which is shown in detail in Figure 3.4. During the temperature ramp, an intermediate interruption of the growth process was performed by cooling the system to room temperature after an initial annealing in vacuum ($p \approx 4 \times 10^{-7}$ mbar, 900°C, 30min). The system then was vented by introducing argon gas to change the pressure to ≈900 mbar. This additional cooling step was performed for two main reasons: (i) avoiding the possible influence of the argon flux on the sample during pressure

change (vacuum to ≈900 mbar), (ii) increasing the carbon condensation on the substrate. The process was proceeded by intermediate annealing at 1200 °C and 1400 °C for 10 and 2 minutes, respectively. Afterwards, the samples were heated directly up to 1750 °C and annealed (6 min) while argon flux was kept at 0 sccm. All the temperature ramps were applied at the same heating rate of ≈7 °C/s. Finally, the heater was switched off, and the samples were allowed to cool down to ≈400 °C (no Ar flow), then to room temperature under Ar flow of 500 sccm.

The special growth protocol has led primarily to a reduced step bunching behavior with rather low steps in particular for S1 which shows step heights of 0.25 nm and 0.5 nm in sequential pairs. For other aspects of the graphene quality (carrier density and mobility as well as defect density, bilayer coverage and homogeneity determined by Raman spectroscopy) we do not expect and we found no indication of a significant change in quality compared to 'normal' PASG graphene described in Ref. [11].

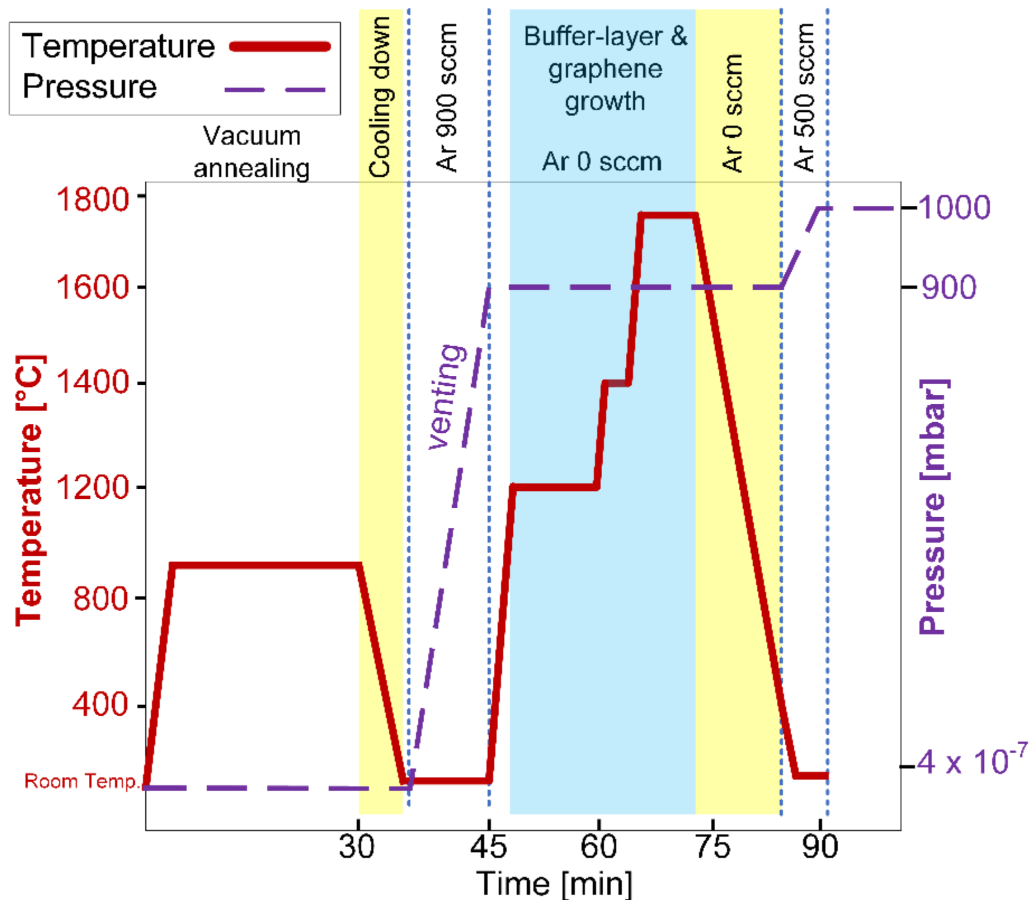

Figure 3.4 PASG epitaxial graphene growth process performed on S1 (6H-SiC) and S2 (4H-SiC).

Electronic transport | Electron density and mobility of graphene samples of 5 mm x 5 mm were measured by Van der Pauw measurements using Au pins which were softly pressed onto the sample surface close to its corners. Before the graphene at the surface was decoupled from the rest on the edges and the rear side by scratching lines close to the edges of the samples. The measurements were performed in vacuum after growth without lithographical processing. The ohmic characteristic of the samples between -50 µA and 50 µA was checked. For a graphene sample grown by the PASG method and the described growth protocol (S1 on 6H-SiC) the following data were measured at room temperature after annealing at 200 °C in vacuum: electron density $n = 7 \pm 2 \times 10^{11} \mathrm{cm}^{-2}$ [11] and mobility $\mu = 2800 \pm 100\,\mathrm{cm}^2/\mathrm{Vs}$. We are aware that those measurements are susceptible to surface contaminations which can arise from the environment or surface treatment.

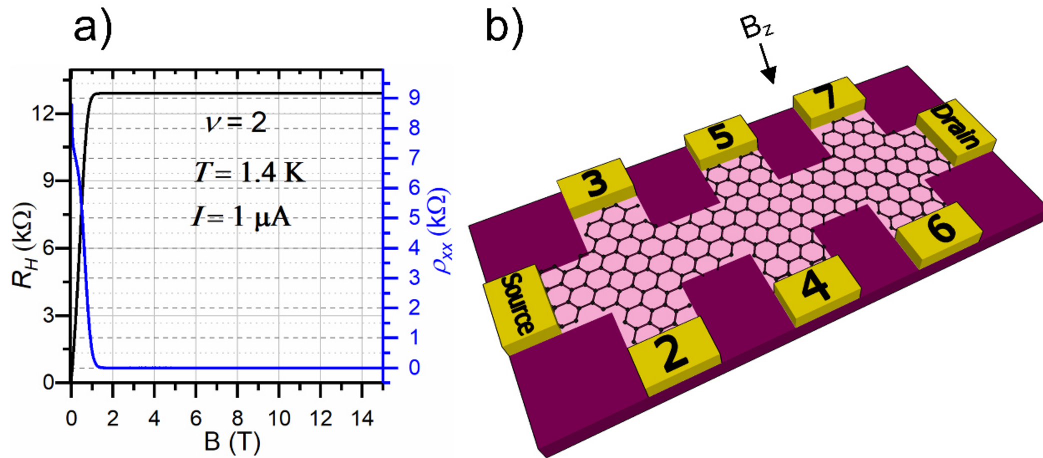

Figure 3.5 Magneto-transport measurements of PASG graphene. (a) QHE measurement result on 6H-SiC/G (S1) with an electron concentration of $n = 5.8 \times 10^{10} \mathrm{cm}^{-2}$ using photochemical-gating technique [133]. (b) Schematic of 8-terminal resistance measurement on a graphene Hall-bar with the size of 100 µm x 400 µm. Current is driven through Source to Drain at the two ends of the Hall-bar. The quantum Hall resistance (measured between the contacts 4 and 5) exhibits a broad plateau at filling factor v = 2 with a value of $R_{\mathrm{H}} \approx 12.9\,\mathrm{k\Omega}$ (half of the von Klitzing constant R_{K}). The longitudinal resistivity ρ_{xx} (measured between the contacts 3 and 7) approaches zero Ohm at about *B* = 2 T.

Magneto-transport measurements | The quantum Hall effect (QHE) measurement was performed on Hall bars with a size of 100 µm x 400 µm which were lithographically fabricated on a 6H-SiC graphene sample similar to S1 described in the manuscript. Before the QHE measurement, a photochemical-gating technique [133] was used to reduce the carrier concentration in the graphene layer down to of $n = 5.8 \times$

$10^{10}\mathrm{cm}^{-2}$. This reduced electron density allows a mobility value of $\mu = 13200\,\mathrm{cm}^2/\mathrm{Vs}$, which demonstrates the very good graphene quality. Figure 3.5 shows the measured Hall resistance R_H and the longitudinal resistivity ρ_xx as functions of the magnetic field *B* at 1.4 K. For *B* ≥ 1.5 T a wide resistance plateau at $\approx 12.9\,\mathrm{k\Omega}$ (corresponding to $R_\mathrm{K}/2$) is observed and simultaneously ρ_xx approaches zero Ohm indicating a good and homogenous quantization.

Raman Spectroscopy. The PASG method allows very smooth graphene growth which suppresses the formation of bilayer graphene. This is proven by the small linewidths (full width at half maximum, FWHM) of the characteristic 2D peak. Typical 2D mappings which were presented in a study of PASG graphene [11] are very similar to the Raman spectra of the graphene samples produced by the growth protocol described in this publication, see Raman spectra in Figure 3.6b. The Raman 2D-FWHM mapping of an area of 20 µm x 20 µm is shown in Figure 3.6. The narrow FWHM value of $33.5 \pm 2.6\,\mathrm{cm}^{-1}$ indicates the presence of pure homogenously distributed monolayer graphene without bilayer inclusions [134].

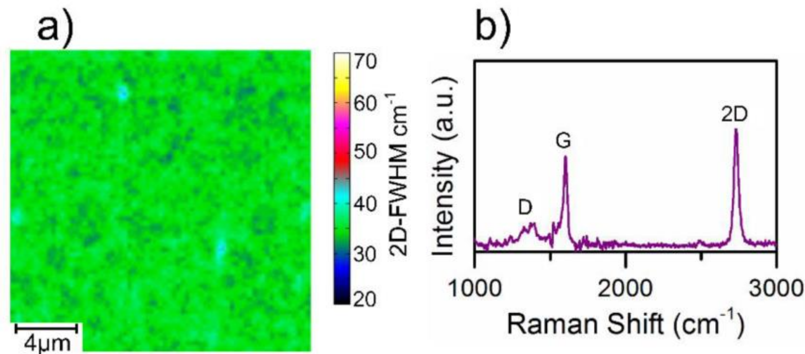

Figure 3.6 Raman spectroscopy of the PASG graphene S1. (a) Raman mapping (20 µm x 20 µm) of the linewidth FWHM of the 2D-peak measured on the PASG graphene sample S1. (b) Average Raman spectrum recorded from the mapping area (20 µm x 20 µm) indicating the G-peak at $1599\,\mathrm{cm}^{-1}$ and the 2D-peak at $2728\,\mathrm{cm}^{-1}$ with a small 2D-FWHM $= 33.5\,\mathrm{cm}^{-1}$proving monolayer graphene on the sample S1.

4 Sheet Resistance on a Local Scale

Analyzing the STP data shown in the previous section 3.2.3, it was noticed that the sheet resistance to the left and right of a substrate step is not identical, but shows deviations in the range of about 15% at room temperature. Therefore, in this section, scanning tunneling potentiometry is used to specifically address the question 'How homogeneous is epitaxial monolayer graphene regarding charge transport on a truly atomic scale?' in a systematic and quantitative study.

Originally, much of the research on graphene was fueled by the fact that it was seen as a candidate for future applications, particularly in electronic devices. As a result, charge transport in graphene has been the subject of countless studies (see e.g. Ref. [36] for a thorough review on epitaxial graphene on SiC). Initially, it was argued that the pseudo-relativistic behavior, which is a consequence of the linear dispersion (see section 1.1.1), cannot be observed in epitaxial graphene on SiC due to the strong coupling to the substrate [6]. However, this issue was resolved when the 'half-integer quantum Hall effect' was experimentally observed in graphene on SiC, which is a unique feature of monolayer graphene [7–9]. These early works mainly rely on macroscopic transport measurements and despite the significant conclusions that can be drawn regarding the pseudo-relativistic behavior of the charge carriers, the graphene samples investigated in the different studies show variations in their charge carrier densities and mobilities. Comparing different studies with each other, the origin of these variations may lie in differences in the growth process and the subsequent processing. However, deviations in mobility and charge carrier density can also be found within a specific study (see e.g. [9]).

From 2012, in addition to the macroscopic approach, charge transport in graphene on SiC was also studied on the local scale using scanning probe methods. Ji et al. determined the sheet resistance at $\mathrm{T} = 72\ \mathrm{K}$ to be $\approx 200\ \Omega$ [85], whereas Clark et al. reported a local sheet resistance of $833\ \Omega$ at $\mathrm{T} = 81\ \mathrm{K}$ [87]. In the study by Ji et al, the macroscopic current density was used to calculate the local sheet resistance from the evolution of the electrochemical potential. However, this assumption is not valid for inhomogeneous samples, e.g. samples with bilayer areas [33]. Clark et al. used a 4-point probe method in which the two probes that induce the voltage

drop across the sample are placed at a distance of about 2µm. This method should, in principle, provide a more accurate estimate for the current density compared to the approach by Ji and coworkers. In Druga's work, the local current density is determined using self-consistent modeling [82], however, the monolayer sheet resistance still shows significant variations ranging from $340\ \Omega$ to $680\ \Omega$ at $\mathrm{T} = 6\ \mathrm{K}$. For the sheet resistance of bilayer graphene, an even larger spread of $190\ \Omega$ to $950\ \Omega$ is obtained. Using atomic-scale magnetotransport experiments based on scanning tunneling potentiometry, Willke et al. determine a monolayer sheet resistance of $230\ \Omega$ and a bilayer sheet resistance of $175\ \Omega$ at $\mathrm{T} = 6\ \mathrm{K}$ [89]. Finally, the incorporation of dopant atoms such as boron or nitrogen can result in a change in the sheet resistance by more than one order of magnitude [69].

In the following publication, we systematically rule out different processes that could lead to local variations in the sheet resistance, such as a locally varying current density, by combining the method of STP with high-quality pure monolayer epitaxial graphene grown by polymer-assisted sublimation growth. Thereby, we reveal a direct correlation of the local transport properties of the graphene sheet with the distance to the substrate as well as with the stacking order of the SiC.

4.1 Author Contributions

A.S., P.W., M.W. planned the experiments. D.M.P. and K.P. prepared the samples. A.S. and G.A.T. performed the room temperature STM measurements, A.S. acquired the low-temperature data. A.S. carried out the main part of the data analysis, G.A.T. assisted in the analysis of the room temperature data. A.S. performed the COMSOL calculations. P.S. and F.S. conducted the ARPES measurements. Interpretation of ARPES results was done by P.S., F.S. and T.S.. A.S. produced the van der Pauw device and performed the macroscopic transport measurements. A.S. and M.W. wrote the manuscript. A.S., G.A.T., D.M.P., P.S., P.W., F.S., T.S., C.T., K.P., H.W.S. and M.W. discussed the results and commented on the manuscript.

4.2 Substrate Induced Nanoscale Resistance Variation in Epitaxial Graphene

A. Sinterhauf, G. A. Traeger, D. Momeni Pakdehi, P. Schädlich, P. Willke, F. Speck, T. Seyller, C. Tegenkamp, K. Pierz, H. W. Schumacher, Martin Wenderoth

Nature Commun. **11**: 555, 2020

DOI: 10.1038/s41467-019-14192-0

Licensed under CC BY 4.0

Graphene, the first true two-dimensional material, still reveals the most remarkable transport properties among the growing class of two-dimensional materials. Although many studies have investigated fundamental scattering processes, the surprisingly large variation in the experimentally determined resistances is still an open issue. Here, we quantitatively investigate local transport properties of graphene prepared by polymer-assisted sublimation growth using scanning tunneling potentiometry. These samples exhibit a spatially homogeneous current density, which allows to analyze variations in the local electrochemical potential with high precision. We utilize this possibility by examining the local sheet resistance finding a significant variation of up to 270% at low temperatures. We identify a correlation of the sheet resistance with the stacking sequence of the 6H silicon carbide substrate and with the distance between the graphene and the substrate. Our results experimentally quantify the impact of the graphene-substrate interaction on the local transport properties of graphene.

4.2.1 Introduction

Charge transport in epitaxial graphene has been subject of theoretical and experimental investigation since its first electronic characterization [62]. The high quality and its 2D nature make epitaxial graphene the perfect system to study fundamental transport properties on the nanometer scale. Consequently, in a series of experiments - based on scanning tunneling potentiometry (STP) [106] or four-point-probe microscopy [105] - several groups have focused on local properties like the sheet resistance and the impact of scattering centers like single substrate steps [68,85] or the transition from monolayer to bilayer graphene on transport [84,87]. From these results, it is qualitatively well understood that the transport properties of epitaxial

graphene are not homogeneous on the nanometer scale. Substrate steps or monolayer-bilayer junctions act as local scattering centers. In addition, for epitaxial graphene on SiC(0001) it is well known that interaction with the substrate drastically affects graphene's transport properties. In order to reduce this inherent proximity effect, i.e., to improve the transport properties of the graphene sheet, different strategies were pursued such as the refinement of the growth process [11,135], the use of suitable dielectric substrates like boron nitride [12], the decoupling of the substrate by intercalation [15], or the preparation of suspended graphene [13]. Moreover, the proximity effect can be deliberately exploited to specifically tune the properties of a graphene sheet [13,23–27]. For example, the almost negligible spin-orbit coupling can be significantly increased by bringing the graphene layer into contact with transition metal dichalcogenides [23,24] and proximity superconductivity can be observed in graphene in the vicinity of superconducting materials [30].

In the context of charge transport in epitaxial graphene, a locally varying potential landscape and a spatially inhomogeneous current density are induced by local defects like substrate steps and local variations of the coupling between the graphene layer and the substrate. Analyzing the published results for resistances assigned to specific defects in epitaxial graphene, one finds a large spread [68,80,84,85,87,123,124,136–138]. The strong variation in the experimental values of sheet or defect resistances determined by local probe measurements is likely due to the lack of information about the actual local current density. Replacing the probe by a single-electron transistor allows simultaneous measurement of local voltage drop and current distribution in 2D materials [139] with a lateral resolution in the range of 350 nm [139]. In comparison, STP has an angstrom resolution [108] and measures the local electrochemical potential with high accuracy, but local variations in the current density are experimentally not accessible and are indistinguishable from spatial variations of the sheet resistance. For conventionally grown graphene on SiC(0001), typically monolayers as well as bilayers are present. Monolayer-bilayer transitions represent strong scattering centers and cause a significant variation of the local current density. Having no better approach, so far local transport properties have been determined using an averaged (sometimes even macroscopic) current density for the whole sheet.

In this study, we show that the high quality of epitaxial monolayer graphene samples grown by polymer-assisted sublimation growth (PASG) opens a promising way to quantify also delicate local transport properties with high precision. Applying

the PASG method, it is possible to grow large-scale monolayer graphene sheets without bilayer formation [11,32] on SiC substrates with ultra-low step heights. This allows for local transport investigations of monolayer graphene on terraces with different SiC terminations free from bilayer and step edge effects. The aim of this work is to test for local variations in the sheet resistance of epitaxial graphene and to unravel possible intrinsic proximity effects induced by the presence of the substrate.

4.2.2 Results

4.2.2.1 Homogeneity of the Current Density

The local electric field as well as the local current density are needed to determine the local sheet resistance. While STP measures the local voltage drop, the local current density is a priori unknown. In STP studies, it is replaced by an averaged value, e.g., given by the total current and the geometry of the sample. While this approximation has severe limits for locally inhomogeneous samples, the excellent lateral homogeneity of the PASG graphene parallel to the steps, the absence of bilayer graphene and the low impact of steps on the overall resistance [32], drastically reduce lateral current density variations [81]. In our STP setup, the current flow was deliberately driven parallel to the miscut of the SiC sample, resulting in an overall voltage drop perpendicular to the substrate steps ($[1\bar{1}00]$ direction). The experimental geometry and the assumption that graphene terraces have a constant sheet resistance parallel to the steps result in a constant average current density on all terraces. To estimate the remaining variation in $\mathrm{j_{local}(x, y)}$, we have modeled the local current density for a given surface geometry (Figure 4.1a) taken from constant current topographies (CCT) with a resistor network [80,84,112] and find that the resulting current density exhibits a maximum variation of up to 7% (Figure 4.1b). By carefully selecting regions away from complex step configurations, e.g., convergence of two steps, the current density can be considered as highly homogeneous (compare Supplementary Table 3). It is $\mathrm{j_{local}(x, y) \approx j_{local} = (0.89 \pm 0.01)\ Am^{-1}}$ for an applied voltage along the graphene layer perpendicular to the substrate steps of 1V at $\mathrm{T = 300\ K}$. Comparing the lateral variation of the current density in PASG graphene samples with conventionally grown epitaxial graphene,

it becomes obvious that local variations in ρ_{sheet} from monolayer and bilayer graphene and monolayer-bilayer junctions in conventionally grown epitaxial graphene induce a strong variation of $j_{local}(x, y)$ (Supplementary Figure 4.5).

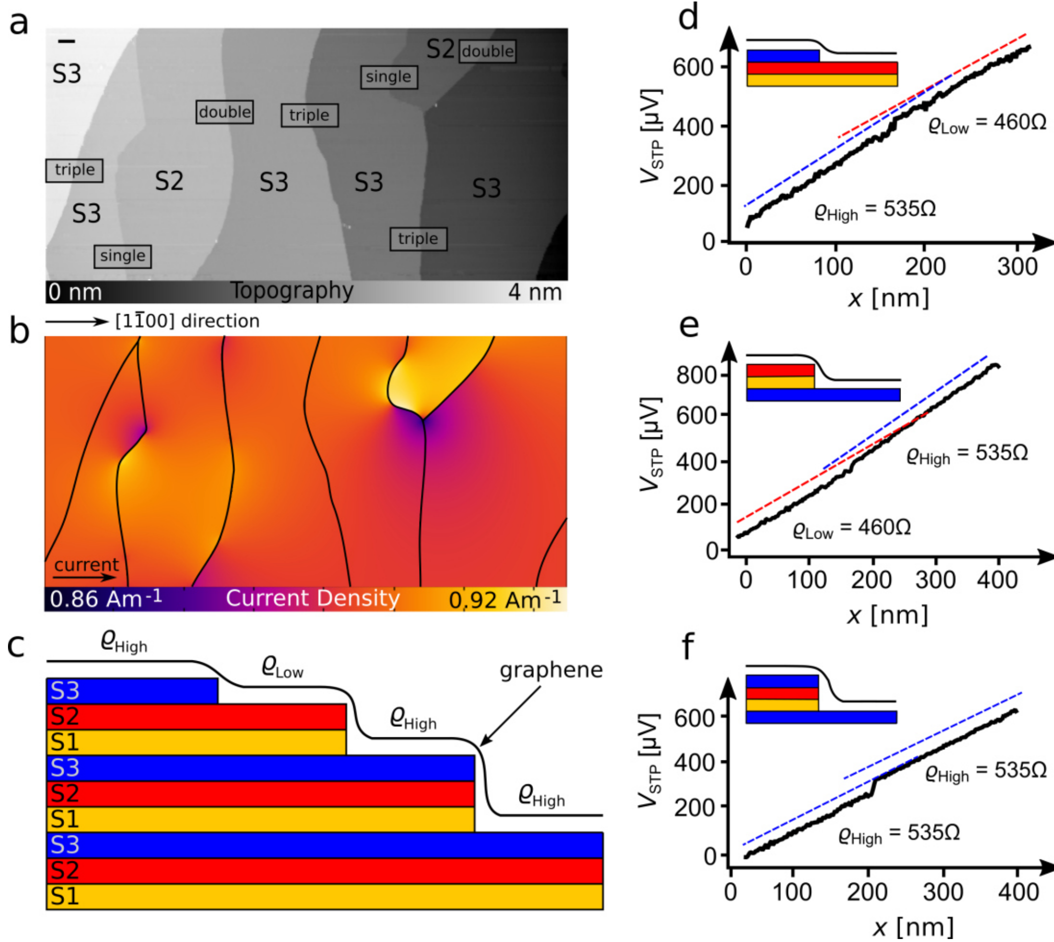

Figure 4.1 Current density and evaluation of the local sheet resistance at room temperature. **a** large-scale constant current topography (2 µm x 1 µm, $V_{Bias} = 0.5\ \mathrm{V}, I_T = 0.03\ \mathrm{nA}$). S1, S2 and S3 indicate the fundamental bilayers (and thus the stacking) of the SiC substrate, details are given in the discussion. STP measurements were performed in the marked areas (black boxes). The height of the steps is denoted in the marked areas. Using the macroscopic ohmic resistance, the sample geometry shown in a and step resistances of $6\ \Omega\mu\mathrm{m}$, $12\ \Omega\mu\mathrm{m}$, $18\ \Omega\mu\mathrm{m}$ for single, double and triple steps, respectively, the scale bar is 100 nm. **b** the $[1\bar{1}00]$ component of the local current density $j_{local}(x, y)$ is calculated with a finite element simulation. **c** schematic side view of the crystal structure of 6H-SiC. **d** example of the measured voltage drop along the graphene layer induced by the cross voltage V_{cross} when crossing a single step. Dashed lines represent the slope of the voltage drop (shifted for clarity). **e** example line profiles for a double step and **f** for a triple step.

4.2.2.2 Variation of ρ_{sheet} at Temperature $T = 300\ \mathrm{K}$

Large scale constant current topographies (Figure 4.1a) reveal a surface with single, double as well as triple substrate steps and no bilayer regions as expected for

epitaxial graphene grown by PASG [11,32,135]. STP measurements investigating ρ_{sheet} are performed across all step configurations in Figure 4.1a, the corresponding voltage drops V_{STP} are shown in Figure 4.1d–f. Interestingly, to the left and to the right of single substrate steps we find a different gradient of V_{STP} (Figure 4.1d), indicated by the dashed blue and red lines representing the slope to the left and to the right of the step, respectively. Since the current density is constant, this directly proves that the top and bottom terrace have different sheet resistances. This finding also holds for terraces connected by a double substrate step (Figure 4.1e), whereas the identical ρ_{sheet} is measured when crossing a triple substrate step (Figure 4.1f). For all step configurations, an additional voltage drop at the topographic position of the step is observed, which is commonly explained by a potential barrier induced by the step due to detachment of the graphene sheet from the substrate [68,85,86].

In order to further investigate spatial variations of ρ_{sheet}, we have measured large sequences of steps. The topographic analysis has shown that instead of a random distribution of step heights, a well-defined sequence of the step heights shows up: along the $[1\bar{1}00]$ direction, either a triple substrate step is present or a single substrate step and a double substrate step are observed. These characteristic step patterns for PASG graphene on 6H-SiC have recently been reported in an Atomic Force Microscopy (AFM) study and have been attributed to the growth process [32]. The detailed STP analysis of large sequences of substrate steps allows deducing two implications: firstly, the evaluation shows that at 300K the sheet resistance across a given terrace is constant (Supplementary Figure 4.6). Secondly, from STP measurements on more than 40 terraces, we extract two clearly distinct sheet resistances, which we refer to as ρ_{High} and ρ_{Low}. The mean ρ_{High} is $535\ \Omega$ and the mean ρ_{Low} is $460\ \Omega$. The mean ρ_{High} and ρ_{Low} deviate by $(14 \pm 1)\%$ from each other at room temperature. Moreover, ρ_{High} as well as ρ_{Low} show a variation from terrace to terrace of $\pm 20\ \Omega$.

4.2.2.3 Temperature-dependence of ρ_{sheet}

In order to disentangle possible scattering processes and to understand the difference between ρ_{High} and ρ_{Low}, we performed further temperature-dependent STP measurements at 77K and 8K (Figure 4.2a). In this study two different samples, both prepared using the PASG method, from two different batches were analyzed

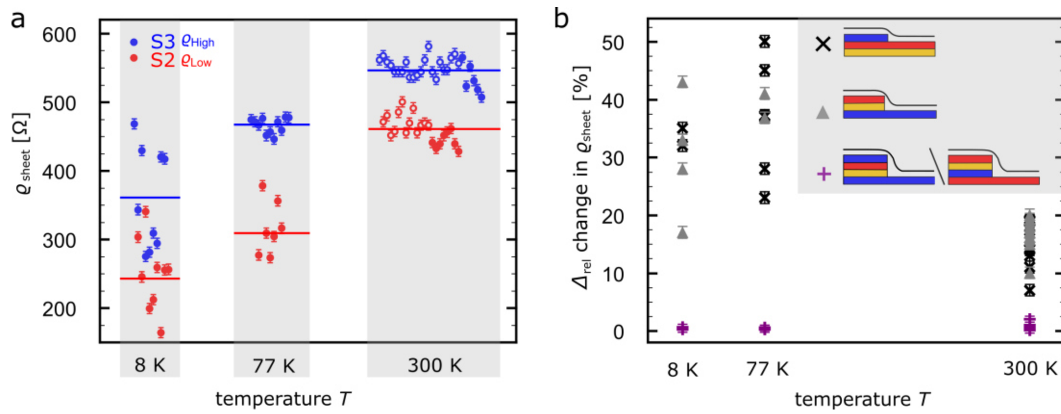

Figure 4.2 Temperature-dependence of the sheet resistance. **a** sheet resistance at 8 K, 77 K and 300 K acquired on more than 80 terraces for two samples (indicated by open and filled symbols), solid horizontal lines indicate the mean value for a given terrace and temperature. **b** change in sheet resistance for adjacent terraces for all three cases S3→S2, S2→S3 and S3→S3 / S2→S2 as a function of temperature. Error bars indicate the experimental measurement uncertainty of the individual data points.

as summarized in Figure 4.2a. Both samples show good quantitative and qualitative agreement at room temperature, low-temperature measurements were carried out on one of the two samples. This allows on the one hand to compare results for different samples and on the other hand to discuss the temperature dependence of the sheet resistance for one given sample. We find an overall decrease in the sheet resistance with decreasing temperature, which is supported by macroscopic transport measurements in four-point van der Pauw geometry (Supplementary Figure 4.7) and in agreement with published results [9,140]. The relative reduction in ρ_{High} with decreasing temperature is slightly smaller, i.e., it reduces by 32%, from $535\ \Omega$ to approximately $365\ \Omega$ at 8 K, compared with the temperature-dependence of ρ_{Low}, which declines from $460\ \Omega$ to an average value of 250Ω at 8 K, i.e., it reduces by 45%. Besides the overall reduction of ρ_{sheet}, a surprising large increase in the spread in the data is observed with decreasing temperature. At 8 K, a maximum variation in ρ_{sheet} of $\approx 270\%$ between the lowest value for ρ_{Low} and the highest value for ρ_{High} is observed. On adjacent terraces a maximum variation of 178% (Supplementary Figure 4.8) is measured. In the following, we will use $\triangle_{\mathrm{rel}} = (\rho_{\mathrm{sheet1}} - \rho_{\mathrm{sheet2}})/(\rho_{\mathrm{sheet1}} + \rho_{\mathrm{sheet2}})/2$ to quantify the relative change in the sheet resistance for adjacent terraces (Figure 4.2b). Regardless of the temperature, when crossing a triple substrate step, the variation in ρ_{sheet} is small, i.e., $\triangle_{\mathrm{rel}} < 3\%$. In contrast to this, the relative variation in ρ_{sheet} to the left and to the right of single

and double substrate steps increases when going from 300 K to 77 K. In particular, for terraces connected by single or double substrate steps a mean relative change of more than 30% is measured. In both cases $\triangle_{\mathrm{rel}}$ slightly decreases from 77 K to 8 K.

4.2.2.4 Analysis of the Surface Morphology of Steps and Terraces

To further investigate the local variation of the transport properties, structural and electronic properties of PASG graphene have been analyzed on different length scales on the same samples. On a mesoscopic scale the surface is characterized by single, double, and triple steps, resulting from the miscut of the SiC substrate. Surprisingly, we rarely found the expected height of the substrate steps, i.e., multiple of 0.25 nm [52]. Instead, we observed deviations of the step height with smaller as well as larger values for both single and double steps. As an example, Figure 4.3a displays a line profile across a step sequence consisting of a single substrate step and a double substrate step.

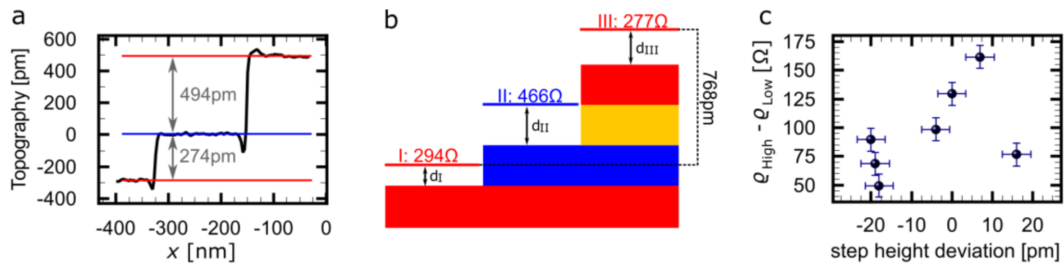

Figure 4.3 Analysis of the step height of single and double steps. **a** Line profile through a constant current topography showing adjacent terraces S2, S3, S2, connected by a single substrate step followed by a double substrate step recorded at 77 K. The line profile reveals a deviation from the step heights of the SiC substrate steps. **b** schematic representation of the correlation between step height and sheet resistance illustrating a locally varying distance d between the graphene layer and the substrate. **c** difference in the sheet resistance for adjacent terraces for single and double steps measured at 8 K as a function of the deviation of the step height. Details are given in the discussion. Error bars indicate the experimental measurement uncertainty of the individual data points.

For this specific step configuration, the analysis reveals a step height >0.25 nm for the single substrate step and a step height <0.5 nm for the double substrate step, i.e., also the combined step height does not fit to the expected value of three times 0.25 nm. Assuming that different step heights correspond to different distances between the graphene monolayer and the substrate, step sequences (Figure 4.3) allow to study the relation between distance and sheet resistance. As usual for

graphene on SiC, also for PASG graphene a buffer layer forms between the SiC surface and the graphene sheet [11]. However, since we cannot pin down the vertical position of the height variation, we use the wording ‘distance to the substrate’.

The corresponding STP measurement reveals a higher conductivity on terrace III compared with terrace I (see Figure 4.3b), indicating that a larger distance results in a smaller resistance. Details on the dependence of ρ_{sheet} on the step height are summarized in Supplementary Figure 4.9, the general trend is that larger distances result in higher conductivities. Moreover, comparing terraces connected by steps with almost identical step height (e.g., Supplementary Figure 4.9 black: 507 pm and pink: 500 pm), we find a large spread of the sheet resistances: 304Ω vs. 365Ω and $165\ \Omega$ vs. $294\ \Omega$ for the black and pink configuration, respectively (see also Supplementary Figure 4.10a–c). Height deviations are found for all temperatures (Figure 4.3a, Supplementary Figure 4.9) and the topographic nature of the observed height deviation in CCT is supported by AFM topographies (Supplementary Figure 4.11). Details of the height analysis are given in Supplementary Figure 4.12 and Figure 4.13.

In order to take the atomic-scale structure of the sample into account, we acquired higher resolved CCTs on terraces connected by single and double substrate steps as shown in Figure 4.4a and Supplementary Figure 4.14b, respectively. On all terraces the 6×6-quasi corrugation is visible. (The wording “quasi” modulation is used, because it consists of two types of ring like structures with slightly different size. One large and two smaller rings together form the superstructure [141].) It is induced by a lattice mismatch of the graphene sheet and the substrate and originates from actual height corrugation as well as from electronic contrast [13,36,141,142]. However, this 6×6-quasi corrugation is structurally not perfect (compare Figure 4.4a). In order to analyze deviations from a perfect ordering, we disentangle the constant current topographies using Fourier analysis (Supplementary Figure 4.15). Applying this type of evaluation for each terrace separately, we disentangle three different contributions to the topographic contrast. Firstly, the 6×6-quasi corrugation itself, secondly short-range noise and thirdly, long-range spatial modulations, which can be understood as perturbations of the 6×6-quasi corrugation. The latter contributions are shown in Figure 4.4b, c for the terraces to the left and to the right of the single substrate step in Figure 4.4a, respectively. We determine the dominant wavelength of these modulations as shown in Supplementary Figure 4.17 and

find a clear difference between the two terraces. The terrace to the left of the single substrate step (Figure 4.4c) shows a spatial modulation with a shorter wavelength of 4.2 nm compared with the wavelength of the spatial modulations on the terrace to the right of the single substrate step (Figure 4.4c) with 8.1 nm. The corresponding, i.e., reversed finding, holds for terraces connected by a double substrate step (Supplementary Figure 4.14b) for which comparable wavelengths of the spatial modulations are extracted. Besides differences in the dominant wavelength, the spatial modulations also exhibit different amplitudes.

In summary, the analysis of the surface morphology allows two conclusions. Firstly, the deviation of the step heights indicates a locally varying distance between the graphene layer and the substrate. Secondly, the 6×6-quasi corrugation does not show a perfect ordering.

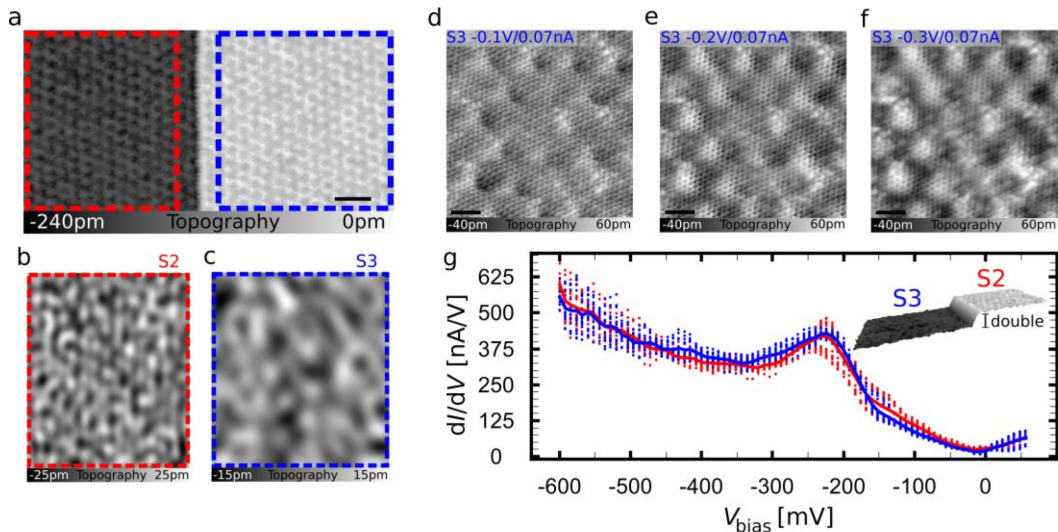

Figure 4.4 Analysis of the local defect structure on terraces S2 and S3**. a** 50 nm x 25 nm constant current topography of terraces connected by a single substrate step. The scale bar is 5 nm. On both terraces the 6×6 modulation is well resolved. The topographic contrast is disentangled into its spectral components (as shown in Supplementary Figure 4.15) using Fourier analysis**.** In **b** and **c** only the long-range contributions to the constant current topography are shown for the areas in a marked with dashed red and blue boxes, respectively. **d** CCT (8 nm x 8 nm, $\mathrm{I_T} = 0.07\ \mathrm{nA}$) to the left of a double step on a terrace S3 acquired with a bias voltage of $\mathrm{V_{Bias}} = -0.1\ \mathrm{V}$, **e** with a bias voltage of $\mathrm{V_{Bias}} = -0.2\ \mathrm{V}$ and **f** with a bias voltage of $\mathrm{V_{Bias}} = -0.3\ \mathrm{V}$ representing the integral local density of states in the energy interval $\mathrm{E_F} \pm \mathrm{V_{bias}}$. For d, e, f the scale bar is 1 nm. **g** Scanning tunneling spectroscopy at $8\mathrm{K}$ on terraces S2 and S3 separated by a double substrate step as indicated in the constant current topography in the inset ($\mathrm{V_{Bias}} = -0.6\ \mathrm{V}, \mathrm{I_T} = 0.15\ \mathrm{nA}$). The solid blue line shows the averaging of all spectra recorded on S3 and the solid red line shows the averaging of all spectra recorded on S2.

4.2.2.5 Analysis of the Local Electronic Structure

CCTs taken at different bias voltages have additionally been used to gain insight into the local density of states of the combined graphene / buffer layer / SiC substrate system in a given energy interval $E_F \pm eV_{bias}$. Since we cannot separate electronic states originating from the buffer layer from states originating from the SiC substrate, we refer to this part as 'interface layer'. For epitaxial graphene on SiC it is known that for larger voltages V_{bias} electronic states of the interface layer become visible in CCTs [58]. In Figure 4.4d–f, we show high-resolution, quasi-simultaneous CCTs recorded at $V_{bias} = -0.1$ V, $V_{bias} = -0.2$ V, and $V_{bias} = -0.3$ V. In all images the graphene honeycomb lattice as well as the 6×6-quasi corrugation are well resolved. They dominate the topographic contrast at $V_{bias} = -0.1$ V. In contrast, at higher voltages additional states of the interface are visible as non-periodic defect structures, which agrees with published results [58,143]. An example for defects of the SiC substrate is disorder. It has recently been shown by X-ray standing wave analysis [144] that the top layer of the SiC substrate is Si depleted. This result is in qualitative agreement with a recent HRTEM study [145] revealing a gradual depletion of Si across the topmost three bilayers. The depletion is due to the partial decomposition of the top SiC layers during the growth process leading to a varying Si concentration. This type of substrate disorder might also be present in PASG graphene.

Spectroscopic measurements using scanning tunneling spectroscopy (STS) at 8K provide insight into the local electronic structure. dI/dV spectra of graphene on SiC show two prominent minima, firstly the so-called pseudogap at 0 meV and secondly a minimum at the position of the Dirac point [69]. The position of the latter minimum gives a hint to the local charge carrier density [146]. In Figure 4.4g the STS data acquired on two terraces connected by a double substrate step are shown. The dI/dV spectra in Figure 4.4g are very similar and in agreement with ARPES measurements (Supplementary Figure 4.16) and published results [69,147]. Quantitative deviations between STS and ARPES measurements may be due to different measurement conditions such as the temperature, the addressability of electronic states in the different techniques and due to the presence of the probe itself in STS measurements. In addition to the two prominent minima, we find a pronounced maximum between −200 mV and −250 mV, which we assign to the interface states observed in CCT.

On closer inspection of the individual $\mathrm{dI/dV}$ spectra it can be seen that the electronic properties on the two terraces are not identical and even on a given terrace we find local deviations (Figure 4.4g). In order to quantify these deviations, we describe each individual $\mathrm{dI/dV}$ spectrum in the region of the minimum at negative voltages with a polynomial fit (Supplementary Figure 4.18). From the minima of these fits we obtain the position of the Dirac point for each spectrum separately. The variations on a given terrace regarding the position of the Dirac point are comparable to the differences in $\mathrm{dI/dV}$ spectra on the two different terraces (Supplementary Figure 4.18). For the terrace to the left we find an average value of $\mathrm{E_D} = (-360 \pm 17)\ \mathrm{meV}$, for the terrace to the right the mean value is $\mathrm{E_D} = (-355 \pm 13)\ \mathrm{meV}$. The error interval is the standard deviation.

4.2.3 Discussion

In order to interpret the local transport properties of PASG graphene, we correlate the structural and electronic STM / STS information with the local STP measurement and thereby address a number of questions. Firstly, can we assign the two distinct sheet resistances ρ_{Low} and ρ_{High} unambiguously to characteristics of the sample? Secondly, what causes the huge spread in the sheet resistance at low temperature found for both ρ_{Low} and ρ_{High}? And finally, can both effects, the differences in ρ_{Low} and ρ_{High} as well as the spread at low temperature, be traced back to the same origin?

In a first step, we assign the specific step structure revealed in large scale topographies (Figure 4.1a) to the stacking sequence of the 6H-SiC(0001) substrate. All SiC crystals consist of fundamental layers of silicon and carbon atoms, arranged in tetrahedral coordination [48–50], referred to as fundamental bilayers. Although the 6H-SiC(0001) exhibits six different (crystal) terminations (labeled as S1, S2, S3 and S1*, S2*, S3* [51] in Supplementary Figure 4.19), only four out of the six possible 6H-SiC terminations are found [32], because the terraces S1/S1* have a higher decomposition velocity [52,53] compared with the other terraces and therefore disappear during the growth process. We label the graphene terraces according to the substrate terminations as S2/S2* and S3/S3*. It directly follows, that graphene on terraces S2/S2* exhibits a low sheet resistance and a short-wave spatial modulation of the 6×6-quasi corrugation. In contrast, a larger sheet resistance ρ_{High} and long-wave perturbations of the 6×6-quasi corrugation are measured on terraces

S3/S3*. A systematic difference in ρ_{High} for S3 compared with S3* and in ρ_{Low} for S2 compared with S2* was not observed (Supplementary Figure 4.13). Therefore, we refer to S3/S3* as S3 and S2/S2* as S2 in the following (compare Figure 4.1c). In summary, we conclude that S2 and S3 are characterized by sheet resistances, which differ by their absolute values as well as by their temperature dependence.

We continue our discussion with a more detailed comparison of the local structural and electronic properties of PASG graphene. In general, a variation in the sheet resistance can be caused by a modified charge carrier density, e.g., in the framework of polarization doping [5,31] as well as a variation in mobility. STS data allow to estimate a difference in the local doping on adjacent terraces. In order to cause the variation in the sheet resistance of 140% for the given terraces, the change in the doping level is expected to become visible as a significant shift of the position of the Dirac point in the STS data of terrace S2 compared with terrace S3. Since the mean Dirac energy on terrace S2 compared with terrace S3 is only shifted by $\approx 5\ \mathrm{meV}$ [iv] (Figure 4.4g, Supplementary Figure 4.18), we discard a locally varying polarization doping [5,31] as the main reason for the observed variation of the sheet resistance. Consequently, the local sheet resistance ρ_{sheet} is predominantly governed by the mobility. The latter is the result of a variety of possible scattering mechanisms like e.g., electron-phonon, electron-electron, or electron-defect interaction, which all could be modified by the local structural and electronic properties of the sample.

To disentangle possible scattering processes in PASG graphene, we first take the measured step heights into account assuming that they reflect the distance of the graphene layer to the substrate and correlate them with the local transport properties of S2 or S3 (see Figure 4.3b and Supplementary Figure 4.10e). Data sets like the one presented in Figure 4.3b allow for a comparison of two terraces with the same substrate termination, yet different distances of the graphene to the substrate. They directly show that a larger distance results in a reduced sheet resistance. To further test this hypothesis, we sort the sheet resistances according to the step heights (Supplementary Figure 4.9, datasets determined at 8K)

[iv] This shift is not significant compared to the experimental uncertainty in the determination of the Dirac energy.

and, with a single exception, find a match that larger distances result in a reduced sheet resistance. This finding holds for S2 as well as S3 termination.

While the step height variation is not a priori expected, the observed correlation is not surprising. For epitaxial graphene on SiC(0001), the buffer layer is partially covalently bonded and thus strongly coupled to the SiC substrate [55], whereas the graphene layer is only weakly coupled [148] by van der Waals interaction. Nevertheless, the electronic properties of epitaxial graphene are known to be strongly influenced by the substrate. Epitaxial graphene shows a strong n-type doping [62,142] from interface states [31] and a limited charge carrier mobility [119] due to substrate induced scattering [9,140]. Already a decoupling of the substrate by intercalation leads to an increase in mobility [14], suspended/freestanding graphene shows the highest mobility [13] and a reduced charge carrier density [149]. We suggest that for a larger distance the graphene layer decouples from the substrate resulting in a reduced impact of the defect states of the interface. Thus, these terraces exhibit an increased mobility and a reduced sheet resistance compared with terraces where the graphene layer is closer, i.e., more strongly coupled to the substrate.

Within the proposed model, we now discuss the temperature-dependence of the sheet resistance, i.e., an increasing conductivity with decreasing temperature. In the semi-classical Boltzmann transport, an increase in the conductivity with decreasing temperature is attributed to freezing out of electron-phonon [150,151] and electron-electron scattering [152]. In addition, potential scattering, screening, and their interplay have to be considered in the discussion. While all these processes depend on the charge carrier density, the electron-electron scattering has been found to be most dominant at high temperatures and low doping [70]. ARPES measurements reveal a high charge carrier concentration of $\mathrm{n} \approx 1 \cdot 10^{13}\ \mathrm{cm}^{-2}$ (Supplementary Figure 4.16) and moreover, our STS results imply a mainly homogeneous carrier density. Thus, the impact of electron-electron scattering can be assumed to be constant on all terraces, i.e., it cannot explain the experimentally observed spread of ρ_{sheet}.

Since the Fermi wavelength of the electrons roughly corresponds to the wavelength of the potential modulations, we have additionally considered phase-coherent transport phenomena. We predominantly observed classical Lorentz magnetoresistance in macroscopic magnetotransport measurements (Supplementary Figure 4.7b), therefore we conclude that weak localization (and phase coherent

transport in general) is only weakly pronounced. Therefore, we do not further consider this effect.

Electron-phonon scattering in graphene on SiC is governed by the contribution from remote interfacial phonons [75,76]. Since the temperature-dependence of the resistance associated with electron-phonon scattering is consistent with our measurements, we attribute a part of the general temperature-dependence to scattering with substrate phonons. Assuming that electron-phonon scattering causes a monotonous decrease of the sheet resistance with decreasing temperature [9,140], we estimate the phonon contribution $\rho^{\mathrm{el-phonon}}(\mathrm{T})$ as the difference between the mean sheet resistance at 300K and the highest measured values at 8K on terraces S3. This estimation yields a phonon contribution of < 100 Ω. Besides the general decrease in the sheet resistance, our data show an increase in the spread of the individual measurements at low temperature (Figure 4.2a) accompanied by a reduction in the sheet resistance of up to $\approx 250\ \Omega$ when going from 300 K to 8 K. Within our model, the spread in the data primarily originates from the dependence of the sheet resistance on the distance d to the substrate. From this, it directly follows that a local modification of the interaction between the graphene sheet and the substrate results in a locally varying mobility. For electron-phonon scattering, one would expect stronger electron-phonon scattering for smaller d, which does not agree with the observed behavior (Supplementary Figure 4.9). This strongly indicates an additional relevant scattering mechanism besides electron-phonon scattering, explicitly depending on d.

Triggered by the observations from CCT, i.e., spatial modulations like the ones observed in Figure 4.4a-c, we propose scattering at local defects and potential fluctuations as the additional scattering mechanism: $\rho(\mathrm{T,d}) = \rho^{\mathrm{el-phonon}}(\mathrm{T}) + \rho^{\mathrm{el-defect}}(\mathrm{T,d})$. The topographic contrast in highly resolved CCT is dominated by the 6×6-quasi corrugation. It is randomly perturbed (Figure 4.4) and consequently, each terrace is unique with respect to its defect structure. This deviation from the perfect ordering of the 6×6-quasi corrugation induces a random potential scattering. A temperature-dependent impact of potential scattering on the resistivity has been studied for charged impurities [153]. At low temperatures, the impact of Coulomb scattering at charged impurities is reduced due to localization of electrons and associated screening. We propose that the basics of this concept can be transferred to our system, replacing the charged defects by the non-periodic potential

fluctuations of the 6×6-quasi corrugation (Figure 4.4a-c) as well as interface states (Figure 4.4d-f). At low temperatures, electrons are trapped in the random potential, thereby screening the spatial modulations of the potential landscape. This results in a weaker potential landscape for the remaining transport electrons, thus contributing to the general reduction in the sheet resistance.

Within the framework of potential scattering it is reasonable that the localization of electrons and associated screening depends on the structural characteristics of the respective terrace, i.e., the exact shape of the random potential landscape. Therefore, the defect structure that is expected to change from terrace to terrace leads to a variation in the potential as well as the screening. This becomes visible as the large spread in the sheet resistance at low temperatures.

Having identified the distance between the graphene and the substrate as an important parameter that controls the sheet resistance in general, the question arises whether this parameter also explains the different sheet resistances of the graphene sheet on terraces S2 compared with terraces S3. Figure 4.3c shows the difference in the sheet resistance for adjacent terraces S2 and S3 with respect to the experimentally determined step height deviation. It reveals no clear dependence of the variation in the sheet resistance for adjacent terraces S2 and S3 on the height deviation and thus implies that, in addition to the distance dependence of the sheet resistance, intrinsic differences between S2 and S3 exist. Although not providing a comprehensive picture, first indications of these intrinsic differences can be found in the wavelength of the structural modulation (Figure 4.4) of S2 and S3, in the local defect structure of the interface layer and by comparing the local I(V) spectra acquired on S2 and S3 that show slight differences in the spectra at e.g., -300 mV.

In summary, the spatial homogeneity of PASG graphene allows for a quantitative analysis of electronic transport on a local scale. We have shown a direct correlation of the structural as well as the electronic transport properties with the substrate. In particular, PASG graphene shows a locally inhomogeneous sheet resistance, which is governed by both the substrate termination of the SiC and the distance between the graphene layer and the substrate. A locally varying distance to the substrate is accompanied by a variation of the impact of the interface states such that a larger distance leads to a reduced resistance. By analyzing the temperature-dependence of the sheet resistance we have disentangled different scattering

mechanisms and have thereby revealed a large inhomogeneity in the sheet resistance at low temperatures associated with the imperfections of the 6×6-quasi corrugation and localized defects.

Besides the investigation of fundamental processes in the interaction between substrate and graphene, the reported anisotropy could be exploited in further transport experiments. For example, it is interesting to simply rotate the sample by 90° such that the current is applied parallel to the steps instead of perpendicular. Generally, terraces S2 with ρ_{Low} carry more current than terraces S3 with ρ_{High} depending on the ratio of the two sheet resistances (see Supplementary Figure 4.20) yielding transport channels with a minimum width of about ten times the Fermi wavelength. Thus, by selecting suitable narrow terraces, quasi 1D electronic transport might be accessible in a 2D sample. In addition, terraces S2 act as nanoscale heat sources and terraces S3 as heat sinks. This enables the investigation of thermal transport in low dimensions. Thus, PASG graphene can be a model system to study the interplay between electronic and heat transport with the aim of improving the performance of thermoelectric devices [154]. In this context, the question arises as to the limitations of the reported effect, i.e., a maximum variation in the sheet resistance of 270% at low temperatures. Such a strong local inhomogeneity of the electronic transport is an important quality in the field of epitaxial graphene. It e.g., implies that nanometer sized devices could exhibit a local variation in the mobility of up to 270%. We are convinced that the findings of this study can be generalized and should be considered for other 2D materials grown on and in proximity with a substrate.

4.2.4 Methods

4.2.4.1 Sample preparation

Graphene samples investigated in this study were grown on the (0001) Si-terminated face of semi-insulating 6H-SiC wafers with small nominal miscut angle of 0.06° toward $[1\bar{1}00]$ direction applying the PASG technique [11,32]. The idea of this method is to support the growth process with an external carbon source. A polymer is deposited on the substrate using liquid phase deposition before high-temperature sublimation growth is initialized [11,32,135]. The samples were initially annealed in vacuum ($\mathrm{p} \approx 4 \cdot 10^{-7}\,\mathrm{mbar}$, 900 °C, 30 min). The process was proceeded by intermediate annealing in argon ambient ($\mathrm{p} = 900\ \mathrm{mbar}$) at 1200°C and 1400°C for 10

min and 2 min, respectively. Afterward, the samples were heated directly up to 1750°C and annealed (6min) while argon flux was kept at 0 sccm [135]. Samples prepared with this method are almost defect- and bilayer-free and exhibit shallow step heights, as verified in Raman mapping and AFM topographies [11,32].

4.2.4.2 Scanning probe measurements

The experiments were performed in a custom-built low-temperature STM and in a custom-built room temperature STM under UHV conditions (base pressure $< 10^{-10}$ mbar at 300 K, 77 K, and 8K) using electrochemically etched tungsten tips. STS spectra were acquired using standard lock-in technique and a modulation amplitude of 10 mV. The concept of the STP setup is depicted in Supplementary Figure 4.21a. We electrically contact our samples (3 mm × 7 mm) with gold contacts of 50−100 nm thickness by thermal evaporation in a shadow mask procedure in a two-terminal geometry. In order to eliminate surface contamination, the samples are heated up to 400°C for 30 min after reinsertion into the UHV chamber. A voltage V_{cross} is applied across the sample via two gold contacts. The voltage $V_{STP}(x,y)$, which is a measure of the local electrochemical potential, is adjusted such that the net tunnel current I_T vanishes and is additionally recorded as a function of position. The resulting potential map (Supplementary Figure 4.21b) gives access to the voltage drop along the graphene sheet in the investigated sample area. The simultaneously acquired constant current topography (Supplementary Figure 4.21c) allows to directly connect transport and topographic information. The local sheet resistance of each terrace is determined from the potential gradient on the terrace and the current density j as follows [68] $\rho_{sheet} = \frac{dV_{STP}}{dx} \cdot \frac{1}{j} = \frac{E_x}{j}$

4.2.4.3 Finite element simulation with COMSOL

The local current density $j_{local}(x,y)$ was calculated using a finite element simulation based on COMSOL multiphysics® using the AC/DC module. As input parameters, we enter the macroscopic ohmic resistance and the global geometry of the sample. Additional topographic information like substrate steps, bilayer regions, and corresponding monolayer-bilayer transitions are included according to the structural information from constant current topographies. Step resistivities used in this study are set to $6\ \Omega\mu m$, $12\ \Omega\mu m$, $18\ \Omega\mu m$ for single, double, and triple substrate steps, respectively.

4.2.5 Acknowledgement

A.S. acknowledges financial support from the Deutsche Forschungsgemeinschaft (DFG) through project We 1889/13-1. D.M.P. acknowledges support from the School for Contacts in Nanosystems (NTH nano). P.W. acknowledges support from Institute for Basic Science IBS-R027-D1. We acknowledge support by the Open Access Publication Funds of the Göttingen University and from the Deutsche Forschungsgemeinschaft (DFG) through project TE 386/13-1.

4.2.6 Supplementary Information

4.2.6.1 Supplementary Figures

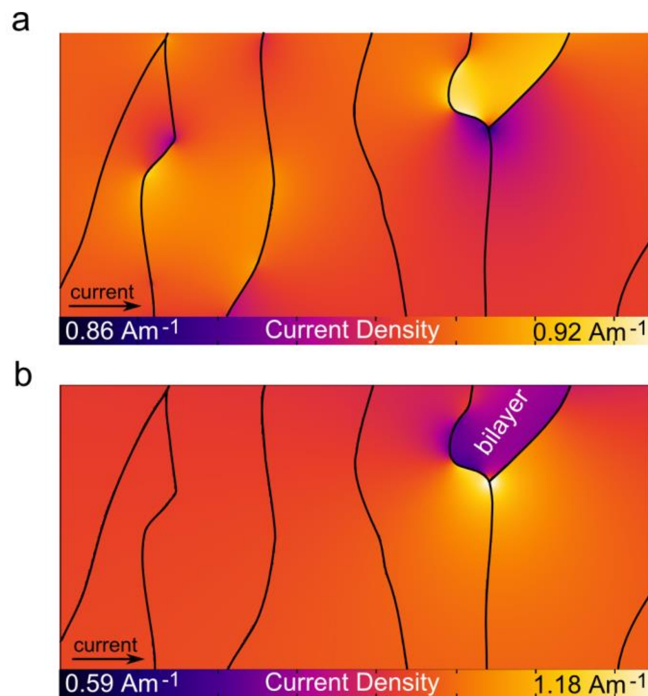

Figure 4.5 Influence of bilayer regions on the homogeneity of the current density. **a** Using the macroscopic ohmic resistance, the sample geometry and step resistivities of $6\ \Omega\mu\mathrm{m}, 12\ \Omega\mu\mathrm{m}, 18\ \Omega\mu\mathrm{m}$ for single, double and triple steps, respectively, as input parameters, the local current density $\mathrm{j}_{\mathrm{local}}(\mathrm{x},\mathrm{y})$ is calculated with finite element simulations using COMSOL for a perfect monolayer grown by PASG. **b** for comparison, a bilayer region with corresponding monolayer-bilayer transition [84] is included in the sample geometry used in a resulting in a highly inhomogeneous local current density. The local variation in the current density increases by almost a factor of ten compared to the pure monolayer case in a as can be seen from the color bars.

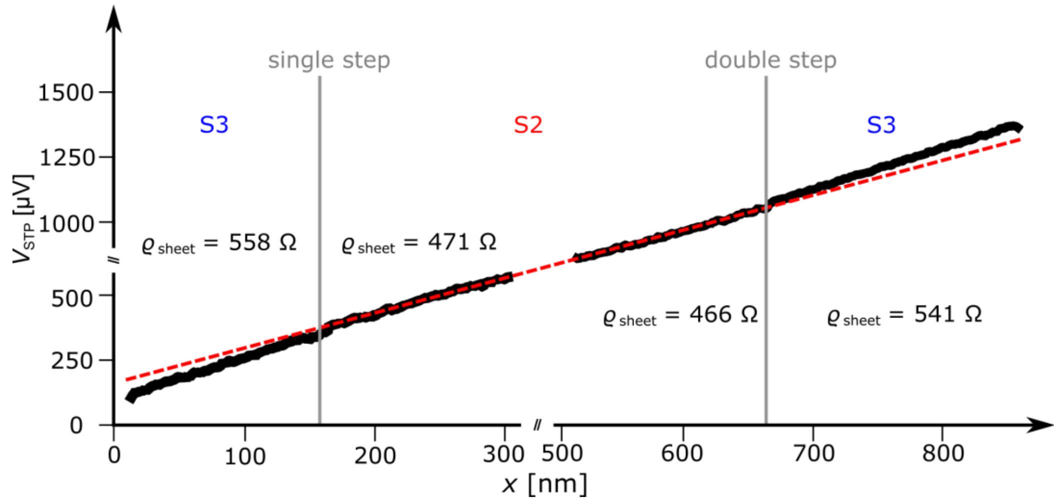

Figure 4.6 Constant sheet resistance across a given terrace. Voltage drop along the graphene layer for adjacent terraces S3, S2, S3 connected by a single step followed by a double step (left to right). The dashed line represents the slope of the potential in the center region, the variation in the slope in this region is $< 2\%$. Regardless of the measurement position, the sheet resistance can be regarded as constant on a given terrace.

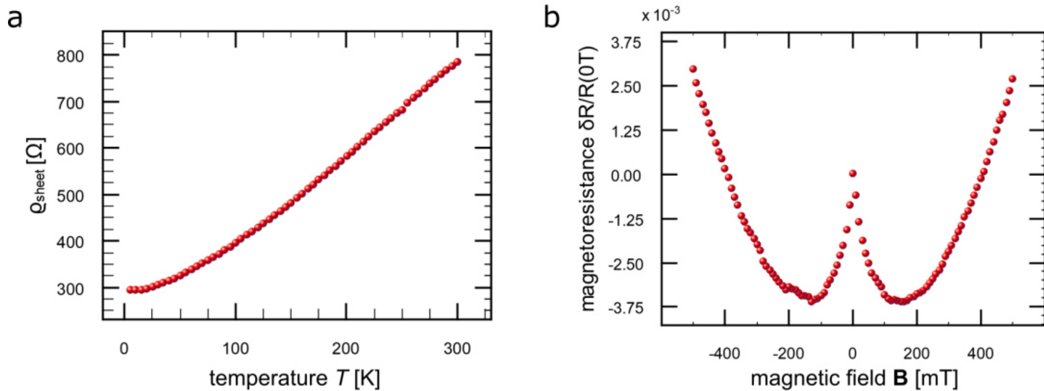

Figure 4.7 Macroscopic transport measurements in van der Pauw geometry. **a** sheet resistance as a function of temperature in the range of $4\ \mathrm{K}$ to $300\ \mathrm{K}$. **b** magnetoresistance for magnetic fields of $-500\ \mathrm{mT}$ to $+500\ \mathrm{mT}$ acquired at $4\ \mathrm{K}$. At small magnetic fields of up to $\pm 100\ \mathrm{mT}$ a negative magnetoresistance is measured, as also observed for conventionally grown epitaxial graphene [69], which then changes to a classical Lorentz magnetoresistance at larger magnetic fields. We attribute the presence of a negative magnetoresistance at small magnetic fields to weak localization. However, the effect of weak localization is significantly less pronounced than in conventionally grown epitaxial graphene [69]. From this we conclude that phase coherent transport phenomena only play a minor role in the samples investigated in this study.

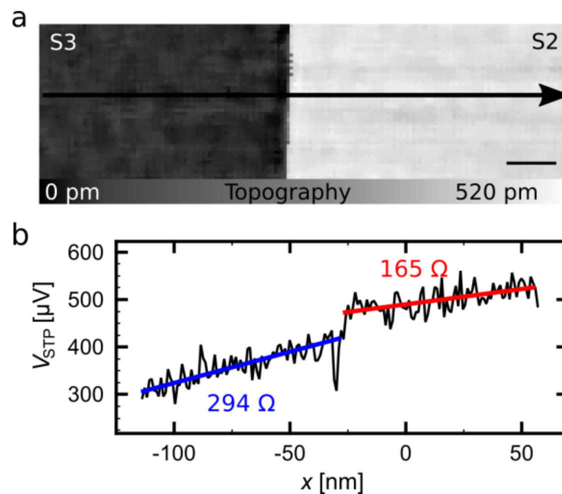

Figure 4.8 STP data set with a variation in the sheet resistance of 178%. **a** constant current topography (imaging conditions: $\mathrm{V_{Bias}} = 0.03\,\mathrm{V}, \mathrm{I_T} = 0.2\,\mathrm{nA}, \mathrm{j} = 4.07\,\mathrm{Am^{-1}}$) of monolayer graphene crossing a double substrate step. The scale bar is 15 nm. **b** averaged potential along the black arrow, solid red and blue lines indicate the slope of the potential from which the sheet resistance is calculated.

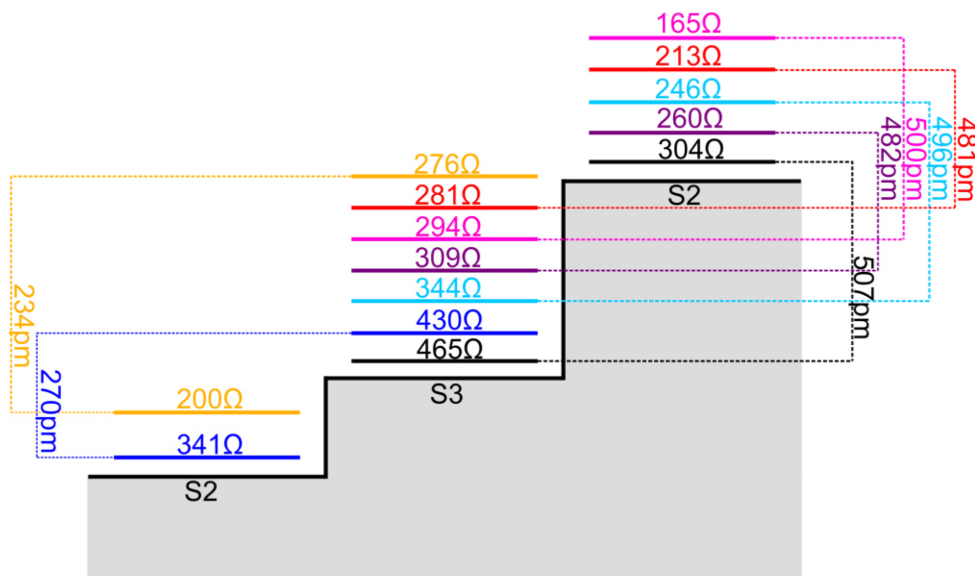

Figure 4.9 Sorting of the data acquired at $8\,\mathrm{K}$ under the assumption that a larger distance to the substrate leads to a reduction of the resistance. For each terrace, the measured sheet resistances are arranged such that for larger values the distance to the substrate decreases (not to scale). The dotted lines connect adjacent terraces and indicate the measured step height. By comparing different data sets, predictions for the step height can be made. The pink data set exhibits a step height of $500\,\mathrm{pm}$. Compared to the pink data set, the red data set shows a lower sheet resistance on terrace S3 and a higher sheet resistance on terrace S2. Thus, according to the proposed model, a step height $< 500\,\mathrm{pm}$ is expected for the red data set, which agrees with the measured step height of $481\,\mathrm{pm}$. The only exception is the yellow data set.

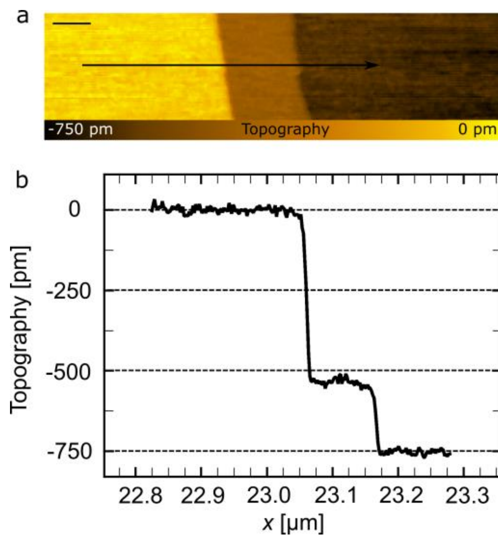

Figure 4.11 Topographic analysis using atomic force microscopy. **a** AFM topography and **b** line profile along the black line in a reveal a step height $< 0.25\ \mathrm{nm}$ for the single substrate step and a step height $> 0.5\ \mathrm{nm}$ for the double substrate step. The scale bar is 50 nm.

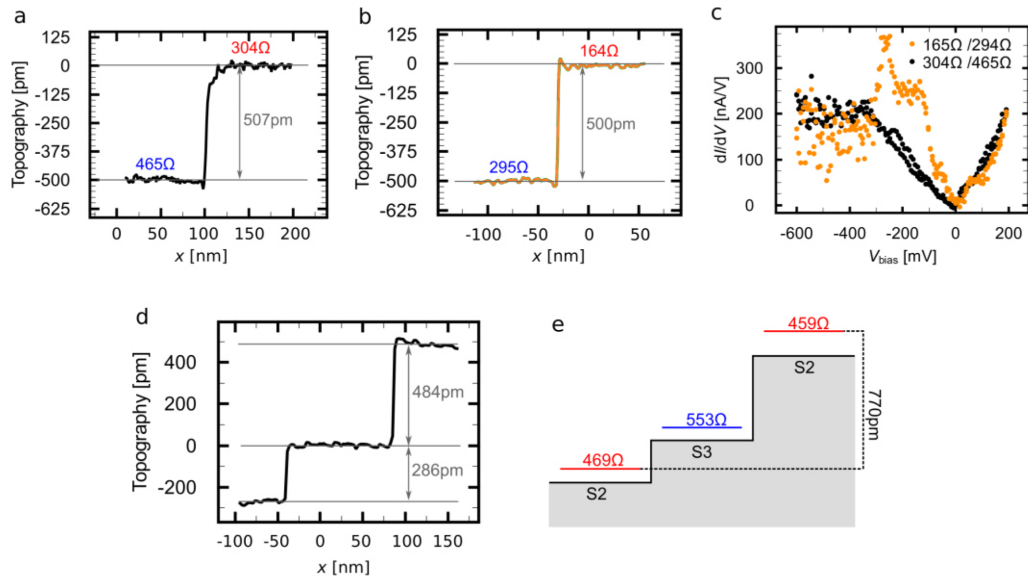

Figure 4.10 Sheet resistance and step height. **a** sheet resistance and step height for the largest sheet resistance measured at $8\ \mathrm{K}$ **b** sheet resistance and step height for the smallest sheet resistance measured at $8\ \mathrm{K}$. **c** Scanning tunneling spectroscopy corresponding to the data sets shown in a and b. **d** Line profile through a constant current topography ($\mathrm{V_{Bias}} = -0.03\ \mathrm{V}, \mathrm{I_T} = 0.2\ \mathrm{nA}$) showing adjacent terraces S2, S3, S2, connected by a single substrate step followed by a double substrate step recorded at $300\ \mathrm{K}$. The line profile reveals a deviation from the step heights of the SiC substrate steps. **e** schematic representation of the correlation between step height and sheet resistance illustrating a locally varying distance between the graphene layer and the substrate.

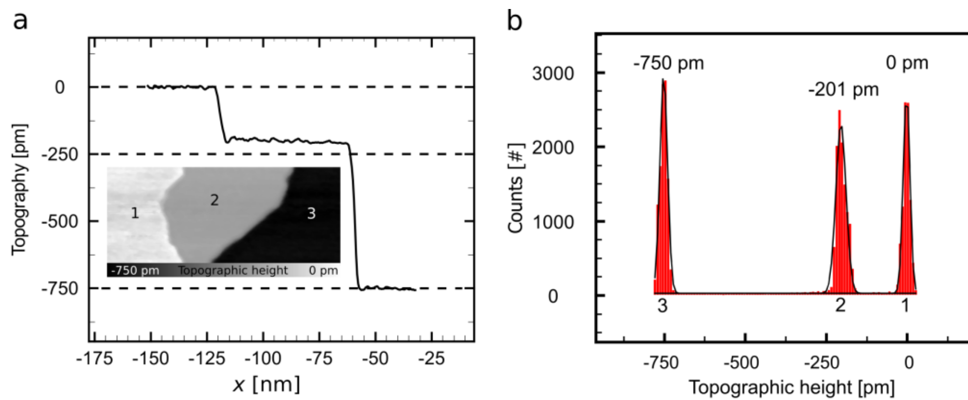

Figure 4.12 Step height analysis using a histogram method. **a** Line profile through a constant current topography (inset: 600 nm x 100 nm, $V_{Bias} = -0.03\ V, I_T = 0.2\ nA$, the scale bar is 5 nm) showing adjacent terraces S3, S2, S3, connected by a single substrate step followed by a double substrate step. **b** height analysis based on evaluating the height information of each pixel. Gaussian curves are fitted to the peaks; the center position of the individual fits are denoted.

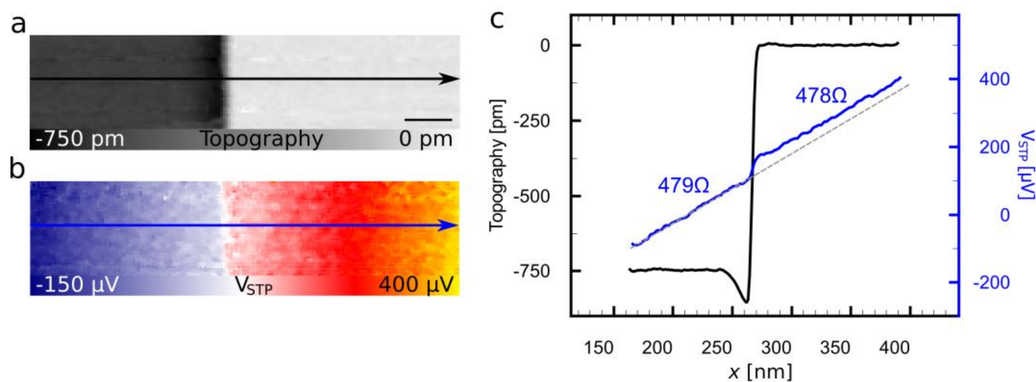

Figure 4.13 Height calibration using a triple substrate step with almost identical sheet resistance to the left and to the right. **a** constant current topography (imaging conditions: $V_{Bias} = 0.03\ V, I_T = 0.2\ nA, j = 4.08\ Am^{-1}$) of monolayer graphene crossing a triple substrate step, **b** simultaneously recorded potential map. The scale bar is 25 nm. **c** topographic height averaged along the black arrow in a and averaged potential along the blue arrow in b. The fact that triple steps show a step height of $750\ pm$ confirms the correct height calibration of the piezo. The calibration was checked for all examined temperatures at several triple substrate steps.

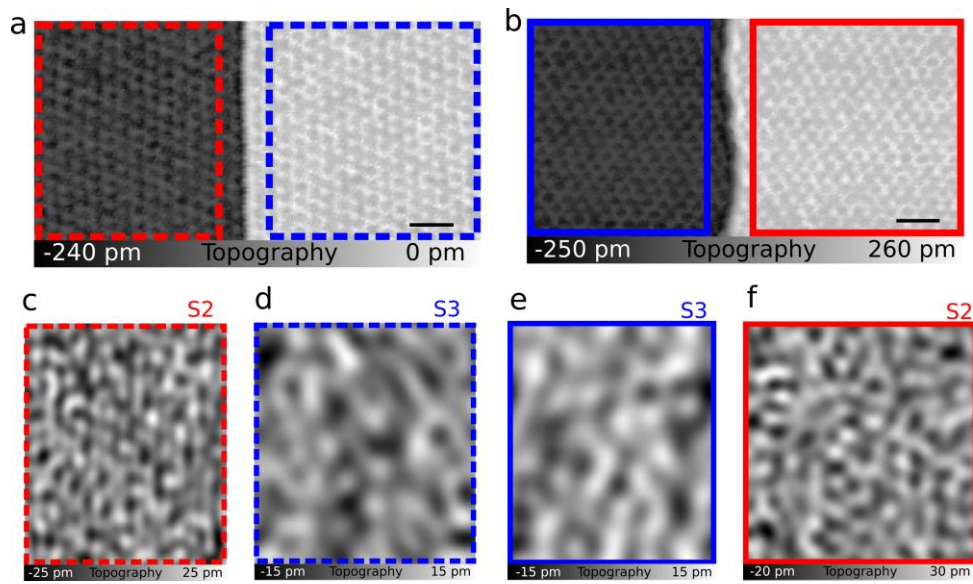

Figure 4.14 Analysis of the topographic contrast on terraces S2 and S3. **a** 50 nm x 25 nm constant current topography of terraces connected by a single substrate step and **b** connected by a double step ($V_{Bias} = -0.3$ V, $I_T = 0.15$ nA). On all four terraces the 6×6 modulation is well resolved. The topographic contrast is disentangled into its spectral components (as shown in Supplementary Figure 4.15) using Fourier analysis**.** The scale bar in a and b is 5 nm. In **c** and **d** only the long-range contributions to the constant current topography are shown for the areas in b marked with dashed red and blue boxes, respectively. **e** and **f** depict the corresponding long-range contributions for the areas in c marked with solid red and blue boxes.

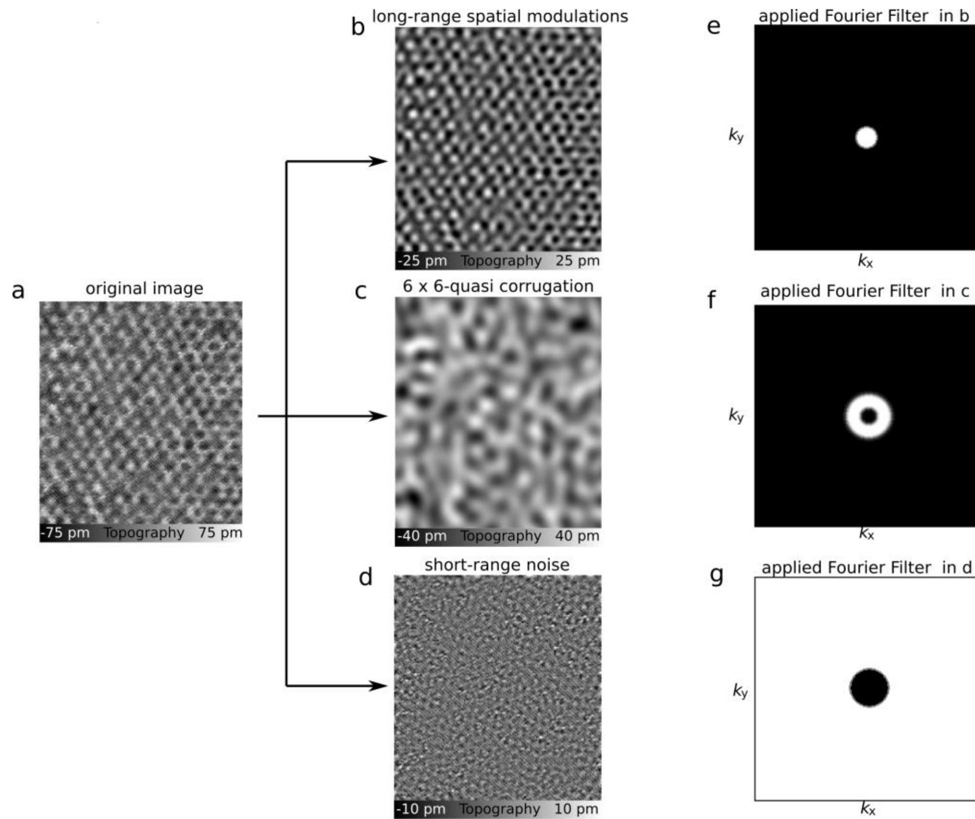

Figure 4.15 Spectral disentanglement of constant current topographies**.** **a** original image is disentangled into its spectral components using different Fourier filters: **b** long-range spatial modulation, **c** the 6×6-quasi corrugation, **d** and short-range noise. **e, f** and **g** applied Fourier filters in b, c and d, respectively. Dark regions indicate spectral components that are filtered out.

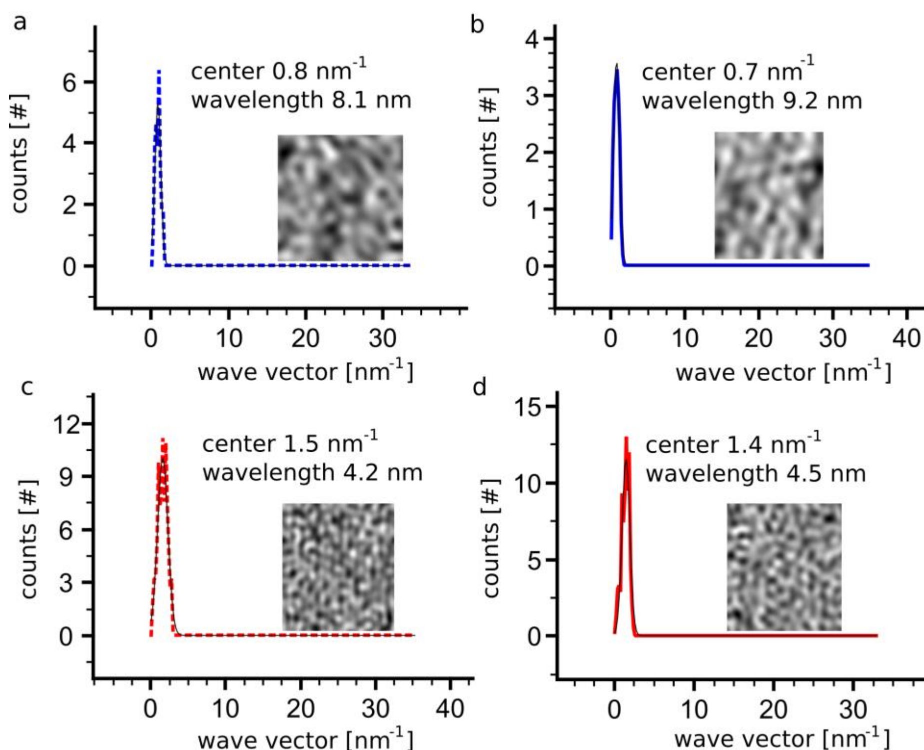

Figure 4.17 Spectral analysis of the long-range spatial modulations. **a** spectral analysis of the upper terrace in Figure 4.4a, **b** spectral analysis of the lower terrace in Figure 4.4a. **c,d**, spectral analysis of the topographic contrast in Supplementary Figure 4.14b. The original CCTs are Fourier filtered as shown in Supplementary Figure 4.15. The resulting long-range contributions are converted into powerspectra for each terrace separately. The wavelength of the spatial modulation is calculated from the center position of a Gauss-Fit adjusted to each powerspectrum.

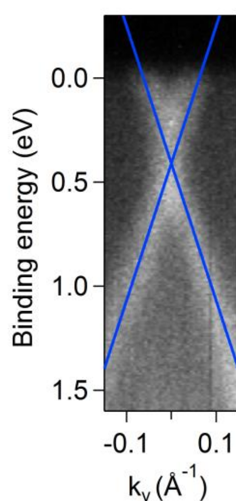

Figure 4.16 ARPES measurements of the π-bands near E_F at the K-point of the graphene Brillouin zone. The photon energy was $\hbar\omega = 40.81\ \mathrm{eV}$. The blue lines correspond to fitted tight-binding bands and the resulting Dirac energy is $E_D - E_F = 410\ \mathrm{meV}$.

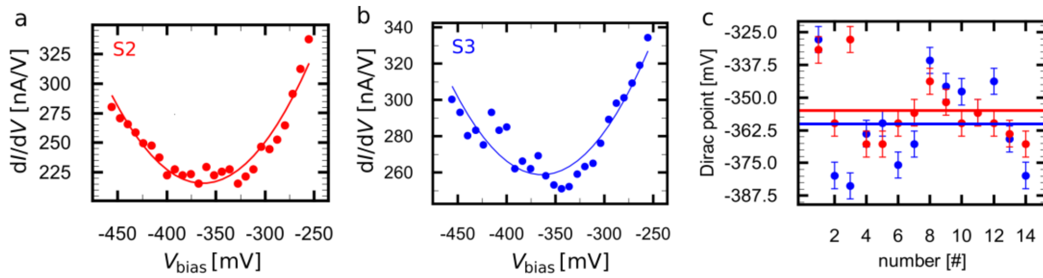

Figure 4.18 Evaluation of the position of the Dirac point. **a** close-up of a single spectrum recorded on a terrace S2 in the voltage range of $-250\ \mathrm{mV}$ to $-450\ \mathrm{mV}$. The solid line shows a polynomial fit. The position of the Dirac point is given by the position of the minimum of the polynomial fit. **b** close-up of a single spectrum acquired on a terrace S3 and corresponding fit. **c** determined Dirac points for all dI/dV spectra shown in Figure 4.4g. On terraces S2 we find an average value of $\mathrm{E_D^{S2}} = (-355 \pm 13)\ \mathrm{meV}$, on terraces S3 the mean value is $\mathrm{E_D^{S3}} = (-360 \pm 17)\ \mathrm{meV}$ as indicated by the solid lines. The denoted error interval is the standard deviation.

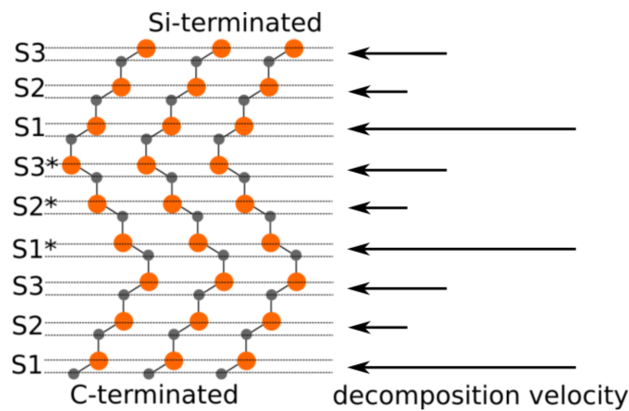

Figure 4.19 Crystal structure of 6H-SiC(0001). Schematic side view of the crystal structure of 6H-SiC and the decomposition velocity according to [52]. For the decomposition velocities, there are different conclusions in literature as to whether terraces S2/S2* or terraces S3/S3* show a higher decomposition velocity, compare [52] and [53]. However, there is agreement that S1/S1* are the terraces with the highest decomposition velocity and thus disappear first during the growth process.

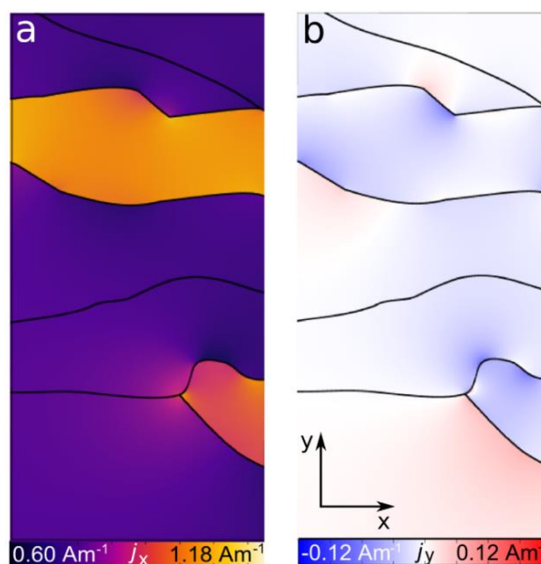

Figure 4.20 Intrinsic quasi 1D current channels. **a** x-component of the current density from finite element simulation with current flow parallel to the substrate steps. In addition to the sample geometry and the step resistances, each terrace has been assigned a sheet resistance ϱ_{sheet} according to the underlying SiC crystal surfaces. **b** y component of the current density.

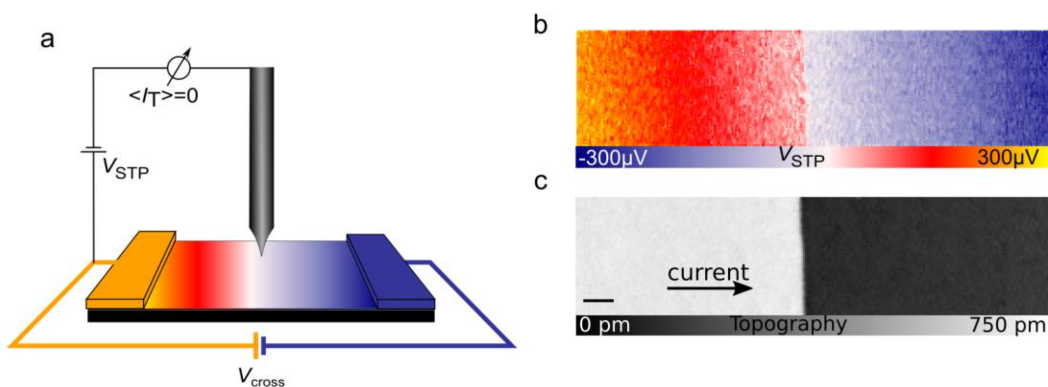

Figure 4.21 Working principle of our STP setup**.** **a** schematic drawing of the STP setup: a graphene sample is contacted in two-terminal geometry and a voltage $\mathrm{V_{cross}}$ is applied across the sample. The voltage $\mathrm{V_{STP}(x,y)}$ is adjusted such that the net tunnel current $\mathrm{I_T}$ vanishes. It is recorded at every position of the topography and represents the electrochemical potential of the sample at the position of the tip. **b** resulting potential map and **c** simultaneously recorded $(200 \times 50)\,\mathrm{nm^2}$ topography (imaging conditions: $\mathrm{V_{Bias}} = 0.03\,\mathrm{V}, \mathrm{I_T} = 0.15\,\mathrm{nA}, \mathrm{j} = 3.56\,\mathrm{Am^{-1}}$) of monolayer graphene crossing a triple substrate step. The scale bar is 10 nm.

4.2.6.2 Supplementary Tables

measure-ment	1	2	3	4	5	6	7
current density [$\mathbf{Am^{-1}}$]	0.880	0.885	0.885	0.880	0.882	0.882	0.891

Table 3 | Evaluation of the current density. Current densities for all marked areas in Figure 4.1a (from left to right) determined from finite element simulations. The macroscopic average current density is $\mathrm{j} = 0.89\ \mathrm{Am^{-1}}$ per applied volt cross voltage $\mathrm{V_{cross}}$.

5 SiC Stacking Order and Surface Potential

Shortly after the publication of the results related to the local variation of sheet resistance (section 4.2), another study was published that also reports on a local variation of graphene's properties directly related to the stacking sequence of the SiC substrate [54]. Momeni Pakdehi et al. use Kelvin Probe Force Microscopy (KPFM) under ambient conditions and Low Energy Electron Microscopy (LEEM) IV spectroscopy in vacuum to characterize PASG graphene. Using KPFM, they find a difference in the surface potential of graphene on S2 terminated surfaces compared to graphene on S3 terminated surfaces of about 10 mV. LEEM-IV curves show a systematic shift in the minimum, which is a characteristics of monolayer graphene in LEEM-IV curves [64], of about 60 meV for graphene on terraces S2 compared to graphene on terraces S3 [54]. Momeni Pakdehi et al. explain the variation in the surface potential with a stacking order-dependent doping of the graphene as sketched in Figure 5.1.

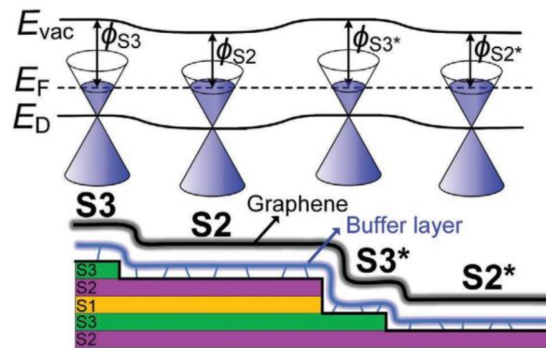

Figure 5.1 Schematic illustration of the main idea of a stacking order-induced doping variation as proposed in [54]. Graphic adapted from Momeni Pakdehi et al. [54] licensed under CC BY 4.0.

For graphene on SiC, two mechanisms are known to have a strong influence on the doping, first, a p-type polarization doping induced by the spontaneous polarization of the SiC substrate and, second, n-type overcompensation by charge transfer from donor states of the interface [31] as discussed in section 1.3.2. The latter mechanism is dominant in epitaxial graphene on SiC. The first mechanism dominates when the donor states are saturated with hydrogen by intercalation. In this case, the strong intrinsic polarization of SiC results in the formation of negative

charges at the interface, which in turn induce positive charges in the graphene to maintain the charge neutrality of the system. Experimentally, a p-type doping of about $4.2 \times 10^{12}\ \mathrm{cm}^{-2}$ is measured for quasi-free-standing graphene on 6H-SiC [5]. Considering that it has already been shown experimentally that the strength of this polarization doping depends on the polytype of the SiC substrate [5], it is in principle conceivable that the local doping of the graphene sheet depends on the termination of the SiC substrate. However, no evidence of this effect was found using spatially resolved scanning tunneling spectroscopy (as discussed in section 4.2.2.5).

5.1 Surface Potential from KPFM

KPFM measurements under ambient conditions on identically prepared samples as in [54] were also performed as part of this thesis. The simultaneous acquisition of the surface morphology allows to deduce the corresponding termination of the SiC substrate from the step sequence, analogous to the STM / STP results presented in section 4.2.2. Figure 5.2a,b clearly shows a significant variation of the surface potential at the step edges compared to the terraces, which is in agreement with the detachment of the graphene at the step edge discussed in section 1.5.3 and 6.2. However, analyzing the local surface potential using a histogram method as shown in Figure 5.2c, we do not find a systematic variation of the surface potential on the differently terminated SiC surfaces.

For a statistically valid statement, a total of 14 independent measurements were performed over different step configurations randomly distributed over a large sample area. The summary of the respective potential differences between the surface potential on terraces S3 compared to the surface potential on adjacent terraces S2 (Figure 5.2d) confirms the absence of a systematic variation of the surface potential with respect to the stacking order of the SiC substrate in our measurements. Instead, we find variations in the surface potential ranging from -10 mV to +10 mV independent of the stacking sequence of the SiC. More precisely, there are positions on the sample where the surface potential on the terrace S2 is 10 mV larger than on the adjacent terrace S3, and there are areas on the sample where we observe the reversed behavior.

Our results indicate no sign of a systematic variation of the surface potential with respect to the SiC stacking order (Figure 5.2). Instead, we suggest that the observed (apparently random) variation of the surface potential could be a consequence of the variation in the range of small negative bias voltages observed in the spectroscopic analysis of PASG graphene (section 4.2.2 and 6.2.3), which we assigned to interface states.

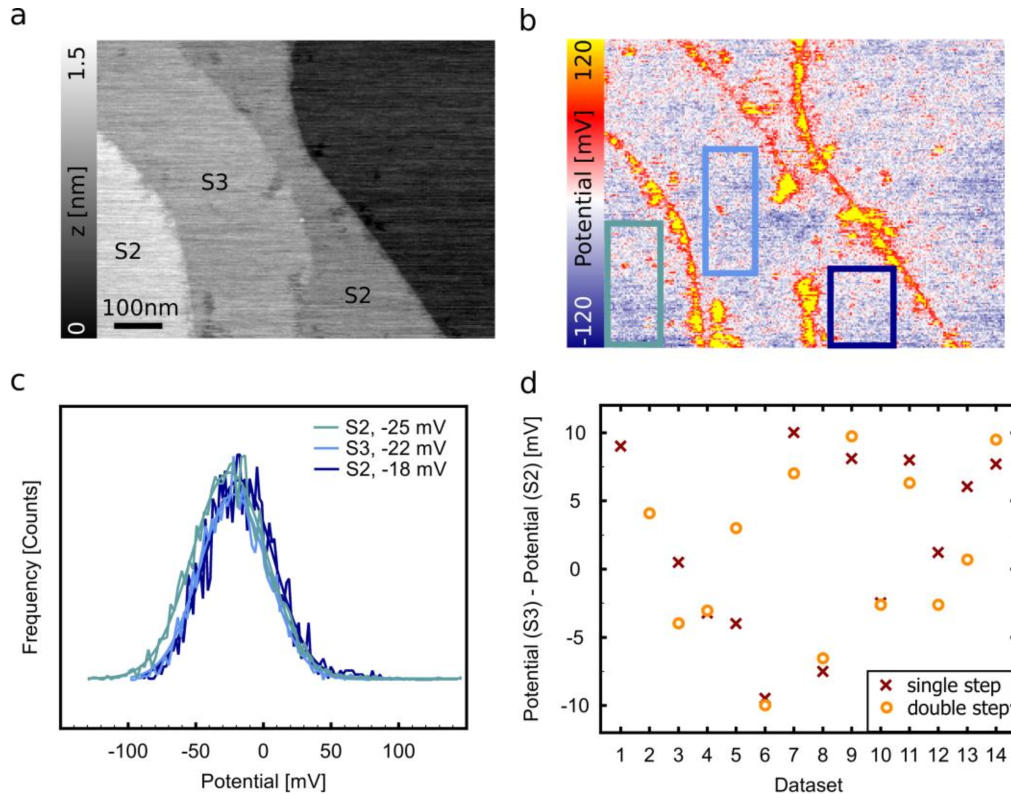

Figure 5.2 KPFM analysis of the surface potential of PASG graphene on SiC. (a) AFM topography and (b) simultaneously imaged surface potential applying FM-KPFM. A variation of the surface potential is measured at the step edges, however, (c) no systematic variation on the different SiC terraces is present as revealed by the histogram analysis in the areas marked with rectangles in (b). The histograms are fitted by Gauss curves and the respective center positions are denoted. (d) Summary of the surface potential on terraces S3 compared to terraces S2 for a total of 14 data sets. Differences in the surface potential on terraces S3 with respect to S2 in the range of -10 mV to +10 mV are found. This clearly demonstrates that there is indeed a local variation in the surface potential, however, this variation is not correlated with the termination of the SiC substrate.

5.2 Simulation of LEEM-IV Spectra

As a second method, LEEM-IV spectra are used in [54] to analyze the surface potential of PASG graphene. LEEM is based on characterizing a sample with an electron beam. The electrons interact with the sample and the image is then formed using the reflected electrons. The concept and the experimental tools, such as the use of electromagnetic lenses, are very similar to transmission electron microscopy (TEM), except that in TEM the transmitted beam is used to produce the image. In LEEM-IV spectroscopy, the intensity as a function of energy is recorded. Momeni Pakdehi et al. attribute the observed shift in the minimum in the LEEM-IV curves (Figure 5.3) to a doping variation [54].

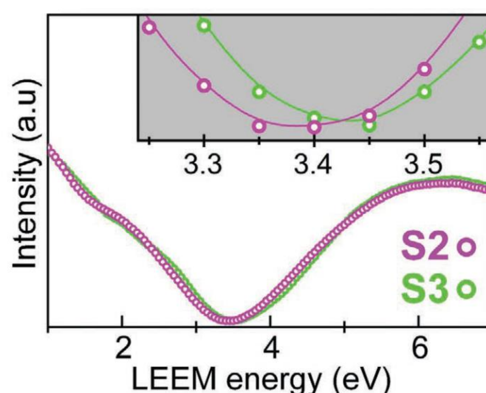

Figure 5.3 LEEM-IV spectra recorded on different graphene terraces S2 and S3 show a shift in the position of the minimum. Graphic adapted from Momeni Pakdehi et al. [54] licensed under CC BY 4.0.

Although a local doping variation is a possible explanation for a shift of the minimum, it is not the only possible explanation. To test for other origins, such as the observed variation in the distance between the graphene and the substrate (section 4.2.2), LEEM-IV spectra were simulated. According to [155], the propagation of a wave package in a potential landscape consisting of two identical potential wells (one representing the graphene and the other the buffer layer Figure 5.4a), can be considered for this purpose. We then propagate the wave package using the split step algorithm and calculate the corresponding reflectivity.

Applying this method, we are able to qualitatively reproduce the experimental LEEM-IV spectra including the minimum typical for monolayer graphene. Changing the distance between graphene and buffer layer as shown in Figure 5.4b (and observed experimentally for PASG graphene, section 4.2.2) with otherwise fixed parameters, results in a shift of our calculated LEEM-IV curves. This illustrates that a

stacking sequence-dependent doping cannot be deduced from LEEM-IV spectra alone.

Based on the results of our STS characterization of PASG graphene (section 4.2.2.5) in combination with work function measurements using KPFM and the presented separation-dependent position of the minimum in the calculated LEEM-IV spectra we conclude that we see no indications for a stacking-dependent doping variation.

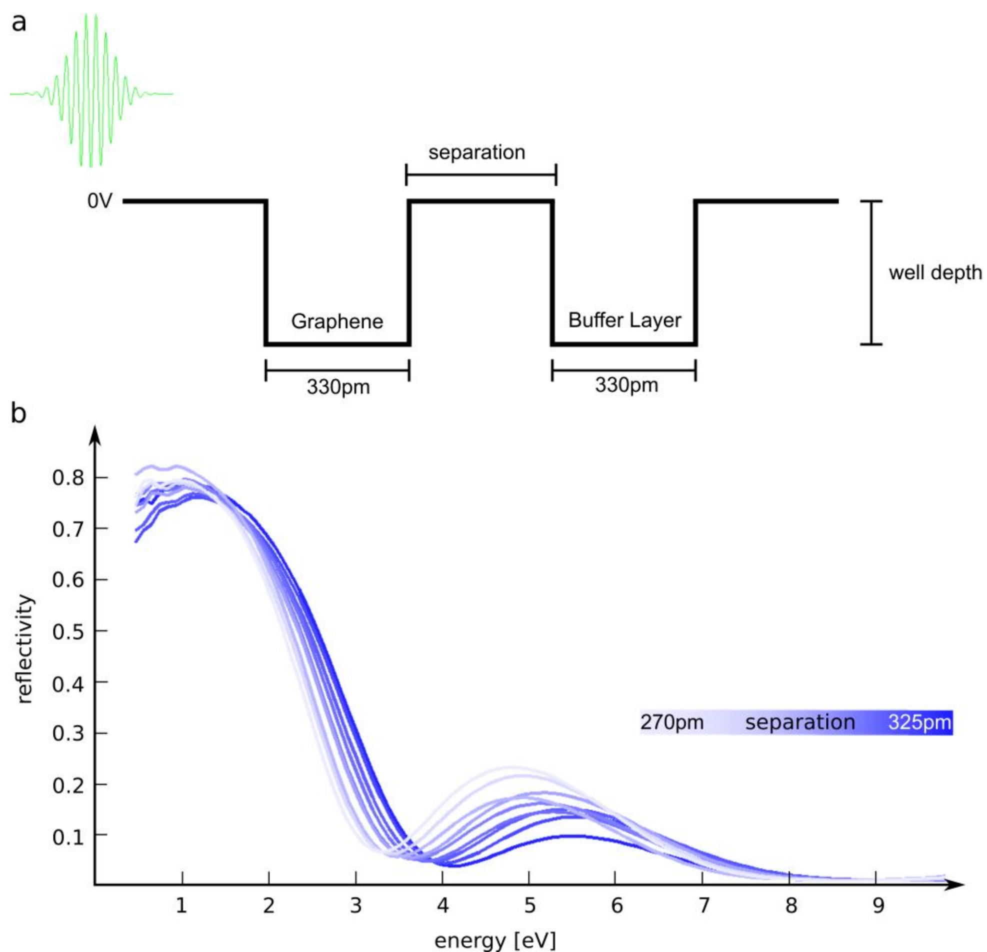

Figure 5.4 Calculation of LEEM-IV curves. (a) the system is modelled considering two identical potential wells, one representing the graphene and one representing the buffer layer. A wave package is propagated using the split step algorithm and the corresponding reflectivity is calculated. (b) Varying the separation between graphene and buffer layer induces a shift in the position of the minimum.

6 Line Defects in Local Transport Measurements

Defects in epitaxial graphene on SiC can take different forms and range from 0D point defects, such as lattice imperfections or foreign atoms, to 1D line defects, such as substrate steps or boundaries between monolayer and bilayer regions, to large-scale inhomogeneities, such as the presence of buffer layer patches due to an incomplete growth process. Some of these defects are intentionally induced with the aim to tune the properties of the graphene, as it is the case for single atoms in the lattice causing a doping of the graphene. This has already been shown for different atomic species [69,146,156] and, e.g., it turned out that the incorporation of Boron into the graphene lattice is a suitable tool to lower the strong n-type doping of epitaxial graphene on SiC or even tune it to p-type doping depending on the dopant concentration [69]. Some defect types can be completely suppressed by refined growth processes, such as the formation of bilayer regions, and, thus, associated monolayer-bilayer transitions [11]. However, other defects, such as substrate steps, are inevitable in epitaxial graphene on SiC.

In general, each individual defect type has a specific influence on charge transport, but since all these defect types can be present at the same time, macroscopic transport measurements only provide an averaged picture, which prohibits determining the exact influence of a specific defect type. Switching to the local scale opens up the possibility to investigate the influence of certain defects independently, which brings us closer to a comprehensive understanding of charge transport in epitaxial graphene.

Prior to this work, several studies have already been published on this subject (see, e.g., [68,85,87,96,157]). It has been shown that substrate steps, although the graphene lies continuously on top of them like a carpet, cause a local voltage drop in the graphene. This voltage drop scales linearly with the height of the substrate step [85,86] as discussed in section 1.5.3. A rather large defect resistance in the range of four to five times the resistance associated with a single SiC substrate step was experimentally determined for monolayer-bilayer transitions [84,85]. Interestingly, in this case the voltage drop does not occur at the topographic position of the junction, but it extends several nanometers into the bilayer region [84].

For both types of defects (substrate steps as well as monolayer-bilayer transitions) comparable to the local sheet resistance there is a large deviation in the literature regarding their quantitative resistance values. In principle, it would be possible that these variations are due to the fact that even with local techniques it is not possible to investigate different defects completely independently of each other due to variations in the current density caused by defects in the vicinity of the investigated defect. On the other hand, similar to the local variation in the sheet resistance (section 4.2), these variations from defect to defect could be an intrinsic property of graphene on SiC. In section 6.2 we investigate this issue for the step resistance and find that the variation of the step resistance is indeed an intrinsic property of graphene on SiC.

6.1 Author Contributions

A.S. and M.W. planned the experiments. D.M. and K.P. prepared the samples. A.S. and G.A.T. performed the room temperature STM measurements, A.S. acquired the low-temperature data. A.S. carried out the data analysis and calculations. A.S. wrote the original draft of the manuscript. A.S. and M.W. reviewed and edited the manuscript. G.A.T., D.M., K.P., H.W.S. and M.W. discussed the results and commented on the manuscript.

6.2 Unraveling the Origin of Local Variations in the Step Resistance of Epitaxial Graphene on SiC: A Quantitative Scanning Tunneling Potentiometry Study

A. Sinterhauf, G. A. Traeger, D. Momeni, K. Pierz, H. W. Schumacher, M. Wenderoth

Carbon **184**, 463-469, 2020

DOI: 10.1016/j.carbon.2021.08.050

Licensed under CC BY 4.0

By combining highly resolved Scanning Tunneling Potentiometry with the exceptional sample homogeneity of graphene on SiC epitaxially grown by polymer-assisted sublimation growth, we reveal local variations in the resistance associated with substrate steps. We quantify these variations and

show that they are an intrinsic property of graphene on SiC. Furthermore, we trace back their origin to variations in the electronic structure of the interface and, thereby, demonstrate the crucial impact of intrinsic proximity effects in graphene on SiC. Moreover, we find a correlation of the step resistance with the local conductivity and show that at room temperature, the step resistance decreases with increasing local conductivity, whereas at low temperatures, it increases with increasing local conductivity. We attribute this inversion to an interplay between the reduction in electron-phonon scattering and potential scattering with decreasing temperature, and the efficiency of the built-up of an almost completely charge carrier depleted zone at the position of the substrate step.

6.2.1 Introduction

Many of the unique transport properties of graphene on SiC can be understood in the framework of ballistic motion of slow relativistic electrons [158]. It is well known that for epitaxial graphene the proximity of the SiC substrate as well as the carbon-rich intermediate layer between the SiC substrate and the graphene layer, the so-called buffer layer, have a decisive influence on the global as well as on the local properties of graphene [31,36,54,148]. Although the SiC substrate is decoupled from the graphene by the buffer layer, it still crucially influences the properties of the graphene sheet, as can be seen e.g. in the framework of polarization doping [5,31] The 6H-SiC substrate consists of six fundamental layers of silicon and carbon atoms referred to as S1, S2, S3 and S1*,S2*,S3* [51]. It was shown that transport properties such as the sheet resistance of graphene show strong systematic variations that can be traced back to the termination of the SiC substrate, i.e. S2/S2* and S3/S3* [33].

Especially the buffer layer is an intrinsic source for disorder. One-third of the carbon atoms in the buffer layer is bonded to Si in the SiC below [55] resulting in a very large unit cell. Interface / surface states were observed in constant current topographies (CCT) by scanning tunneling microscopy (STM) [58] as well as photoelectron spectroscopy showing defect states for the buffer layer [31]. Furthermore, fingerprints of defect states have also been observed in CCT and spectroscopic measurements using scanning tunneling spectroscopy (STS) that reveal an enhanced local density of states (LDOS) at small negative bias voltages [33].

While the impact of the stacking sequence as well as disorder of the interface on the sheet resistance of graphene has been addressed in a recent study [33], their influence on the scattering properties of localized defects has not been considered so far. Within this study, we have investigated the local resistance of graphene carpeting single and double substrate steps. Theses line-type defects are unavoidable even in high quality samples. And although the graphene sheet on top of the SiC substrate continuously crosses these substrate steps [159], a defect resistance ρ_{step} is associated with the steps [85]. Different methods have been used to determine the role of defects on transport, and scanning probe techniques have proven to be particularly useful [84,86,87]. Especially scanning tunneling potentiometry (STP), which measures the local electrochemical potential with the precision of a Scanning Tunneling Microscope, has been utilized to visualize the change in the local potential associated with substrate steps. ρ_{step} is theoretically explained by a local change in the doping, which is significantly lowered in the vicinity of the substrate step due to a detachment of the graphene resulting in an n-i-n-junction [68,86]. A larger substrate step height induces a more pronounced detachment of the graphene sheet on top, i.e., a longer intrinsic doping region, and, thus, an increased step resistance. Experimentally, it has been demonstrated that ρ_{step} increases roughly linear with step height [68,86]. This can be traced back to the band structure of graphene leading to a unique linear ("pseudo-diffusive") behavior [86] of the step resistance as a function of the step height.

While evidence has been found that the step resistance is independent of magnetic field [89] and temperature [68], the compilation of published data on different samples shows a rather wide spread of ρ_{step} [68]. Understanding the origin of this spread can open a way to further optimize the overall resistance of epitaxial graphene. One of the open questions is whether the variation of ρ_{step} can be attributed to a locally varying current density, i.e. a more technical challenge, to differences in the sample quality, e.g. with respect to the growth process, or whether it is an intrinsic property of each individual step.

To this end, we exploit the high quality of epitaxial monolayer graphene samples grown by polymer assisted sublimation growth (PASG) [11,32] in combination with highly resolved scanning tunneling potentiometry (STP). Due to a homogeneous local current density, i.e. $j_{\mathrm{local}}(x, y) \approx j$, which is an intrinsic property of graphene prepared by PASG, this approach allows for a quantitative analysis of local

transport properties [33]. Moreover, the high lateral resolution allows us to correlate the transport properties with structural properties of the steps as well as the electronic and transport properties of the surrounding graphene sheet.

The aim of this work is to identify the dominant parameters, as well as to unravel the underlying processes in order to gain a deeper understanding of the charge transport across substrate steps in graphene on SiC.

6.2.2 Results

The morphology of PASG graphene is mainly dominated by single and double substrate steps. Most important, the negligible amount of bilayer regions [11] assures a homogeneous current density and allows a quantitative comparison of local transport properties [33]. We have applied scanning tunneling potentiometry (STP) to study the impact of single and double substrate steps as one-dimensional line defects on charge transport. In our study, we have taken the parameter temperature into account measuring at 8 K, 77 K, and 300 K. In total, we have analyzed 34 different single and double substrate steps on two different graphene samples both grown by PASG. Figure 6.1 shows an example of a typical STP data set for a single substrate step consisting of a simultaneously acquired constant current topography (CCT) and potential map, resembling the local electrochemical potential under

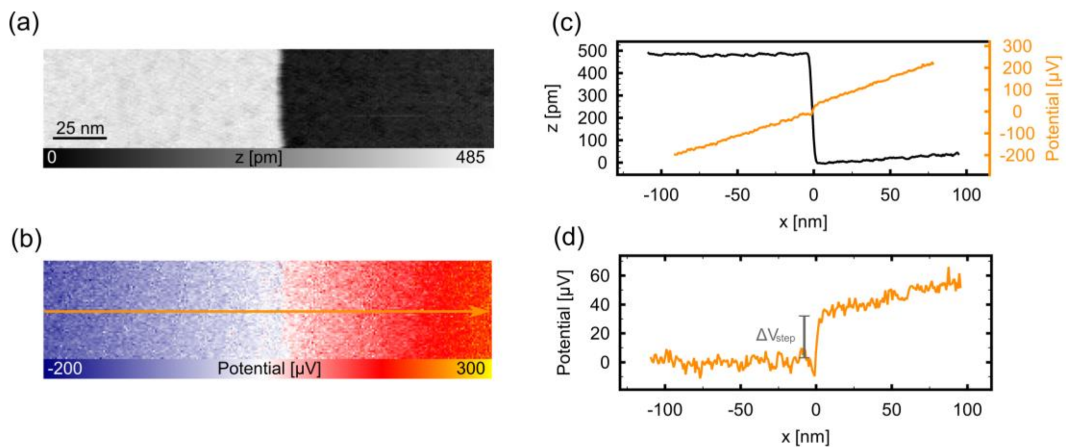

Figure 6.1 Data evaluation (a) Constant current topography (170 nm x 50 nm, $V_{Bias} = 0.03\,V, I_T = 0.2\,nA$) and (b) simultaneously acquired potential map ($j = 5.7\,Am^{-1}$) across a double substrate step acquired at T=300 K (c) topographic line profile and potential line profile. The potential shows a localized jump, associated with the step resistance, which is more clearly visible in (d), where the slope left of the step was subtracted from the averaged potential. The localized jump in the potential is indicated by ΔV_{step}.

transport condition. At the position of the substrate step below the graphene sheet, a localized voltage drop ΔV_{step} is induced which becomes more apparent subtracting the average voltage drop on one of the adjacent graphene terraces (Figure 6.1d). As reported [33], the sheet resistance encoded in the slope to the left and right of the step is different due to the S2, respectively S3 terminated SiC(0001) substrate. It is important to note that although the corresponding step resistance $\rho_{step} = \Delta V_{step}/j$ [68] is calculated based on the macroscopically determined current density j, the superb lateral homogeneity of the current density in PASG graphene across the sample opens the way for a quantitaive comparison of ρ_{step} for different substrate steps.

The experimentally determined mean step resistance averaged over all data sets is $\bar{\rho}_{step}^{single} = 4.7\ \Omega\mu m$ for single substrate steps, and $\bar{\rho}_{step}^{double} = 9.8\ \Omega\mu m$ for double substrate steps. This finding is in agreement with earlier studies reporting a roughly linear scaling between step height and ρ_{step} [86]. The mean step resistance for single as well as double substrate steps as a function of temperature for T=300 K, T=77 K, and T=8 K is shown in Figure 6.2a. These data confirm previous studies as the mean step resistance is within our statistics independent of temperature.

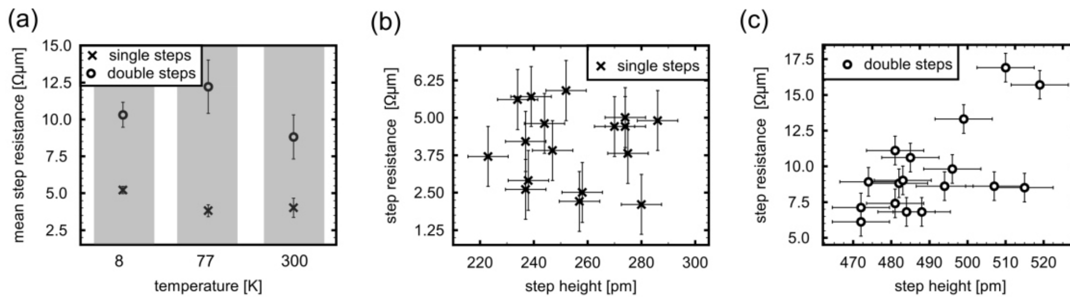

Figure 6.2 Summary of all step resistances. In (a) the mean step resistances are given as a function of temperature. STP measurements were performed at 8 K, 77 K and 300 K. In (a) all step resistances corresponding to single substrate steps and in (b) all step resistances corresponding to double substrate steps are shown as a function of step height.

But while the averaged values are in agreement with published results [85–87], we find a significant variation in the measured step resistances that clearly exceeds the statistical uncertainty of our method. For single substrate steps, the variation between the largest and the smallest value ranges from $2.1\ \Omega\mu m$ to $5.9\ \Omega\mu m$. For double substrate steps, a spread in the data is measured with a minimum value of

$6.1\ \Omega\mu m$ and a maximum value of $16.9\ \Omega\mu m$. In both cases we find a variation of $\approx$ 280%.

Obviously, the step height is an important parameter. Consequently, from constant current topographies we extract the step height for each step. One rarely finds the expected height of the substrate steps, i.e. multiple of 0.25 nm. Instead, we measure smaller as well as larger values for both single and double steps (see Figure 6.2b,c). The variation can be up to ± 25 pm.

Figure 6.2b,c shows the correlation between ρ_{step} and the corresponding measured step height. While the mean values of ρ_{step} scales with the step height h, for single substrate steps there is definitely no clear dependence of the step resistance on the actual step height, i.e. a deviation from the expected step height of 250 pm does not cause a clear trend in the change of the step resistance. For double steps, it seems that the step resistance increases with increasing step height. However, besides the two data sets with a step resistance of $> 15\ \Omega\mu m$ (these values are significantly higher than all other data points), there is no obvious trend. The quantitative analysis, presented in the discussion, will support this conclusion.

In a recent study, we have shown that the sheet resistance ρ_{sheet} of graphene depends on the surface termination of the substrate, i.e., terraces S2 and terraces S3 [33]. Local variations of up to 270% have been found [33]. Being aware of these strong and systematic local variations of ρ_{sheet} of PASG graphene on 6H-SiC [33], we test for correlations between ρ_{step} of each step and the local conductivities of the adjacent terraces. To this end, we plot ρ_{step} as a function of the sheet resistance ρ_{sheet} on the terrace to the right, as well as to the left of the respective step as a function of temperature (Figure 6.3). Overall, we find a dependency between ρ_{step} and ρ_{sheet}. Moreover, the data show an interesting temperature-dependency. For T=300 K, a positive slope is observed for single as well as for double substrate steps, i.e., ρ_{step} increases with increasing ρ_{sheet} on adjacent terraces (Figure 6.3a). In contrast, for low temperatures, a decrease in ρ_{step} with increasing ρ_{sheet} with respect to the adjacent terrace S2, as well as to the adjacent terrace S3 (as shown in Figure 6.3b) is measured. Moreover, the dependence of ρ_{step} on the local conductivity σ (quantified by the slope $(\Delta\rho_{step}/\Delta\rho_{sheet})$) even matches quan-

titatively. This can be seen when comparing adjacent terraces with a different surface termination of the SiC substrate S2 and S3, indicated by the dashed lines in Figure 6.3b exhibiting almost the same slope. Overall, we find a dependence of ρ_{step} on the local sheet conductivity with $\rho_{step} \sim \rho_0 + c(T) \cdot \Delta\rho_{sheet}$ with $c(T) < 0$ for T=8 K and $c(T) > 0$ for T=300 K.

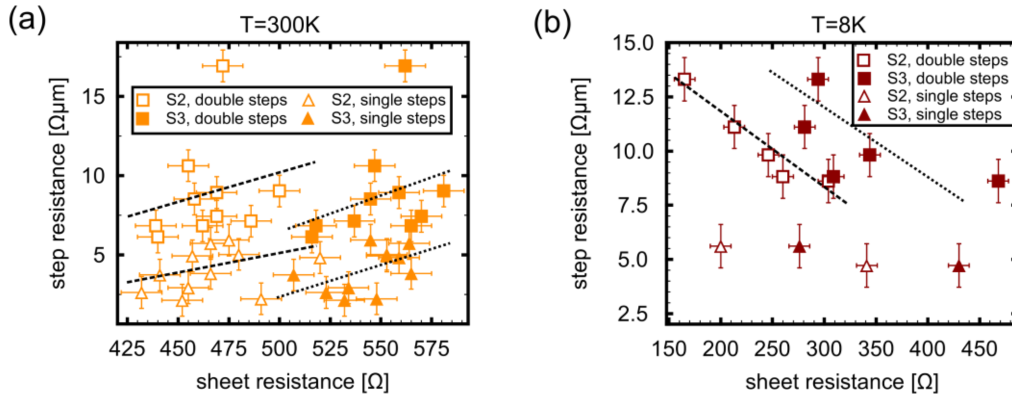

Figure 6.3 Step resistance as a function of the local sheet resistance on adjacent terraces. (a) step resistances for T=300 K and (b) step resistances for T=8 K. Dashed lines are linear fits to the data indicating a correlation between the step resistance and the local sheet resistance.

6.2.3 Discussion

The step resistance ρ_{step} according to Low et al. [86] is attributed to the detachment of the graphene sheet from the SiC substrate. This detachment leads to a local reduction in doping of the graphene resulting in a local n-i-n junction [86]. Low et al. [86] have shown that the graphene can be almost completely depleted of charge carriers in the detached region.

This junction, connecting two graphene terraces, can be thought of as a potential barrier for charge carriers and the transmission probability for the charge carrier to pass the step is finite giving rise to the step resistance ρ_{step}. The linear dependence of ρ_{step} on the step height is traced back to the specific linear band structure of graphene [86]. Transport across such a potential barrier is described by evanescent states penetrating the barrier, which in the case of graphene with the Fermi energy at the Dirac Point results in a pseudo-diffusive behavior, similar to the minimum conductivity case [160]. Most important, the step resistance is determined by the spatial extent of this depleted region [161], labelled in our discussion as $\mathcal{L}$. Our

data show, consistent with published data, a linear dependence of the averaged step resistance $< \rho_{step} >$ on the averaged step height h_{step}, i.e. $< \rho_{step} >= \rho_0 * n$ for n=1,2. Subtracting the experimentally determined impact of ρ_{sheet} on the step resistance, the slope $\Delta\rho_{step}/\Delta\rho_{sheet}$ for each temperature and step configuration individually allows us to analyze the superimposed impact of step height variations for single and double substrate steps as a function of temperature separately, as shown in Figure 6.4a and Figure 6.4b, respectively. The detailed analysis shows that none of these data sets give strong indications for an impact of Δh_{step} on $\Delta\rho_{step}$.

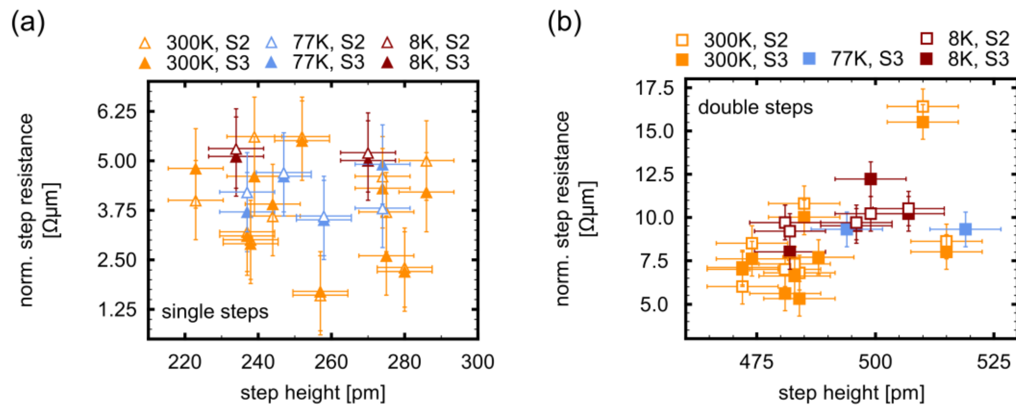

Figure 6.4 Step resistances normalized by the impact of the local conductivity. For each temperature individually, the step resistances are normalized for the local conductivity. In (a) the resulting normalized step resistances are shown as a function of step height for single substrate steps, and in (b) for double substrate steps.

Moreover, based on the linear scaling of the mean step resistance with step height and the average step resistance of $4.7\ \Omega\mu m$ for a single step, a maximum step height deviation of 40 pm only causes a change in the step resistance of $< 0.8\ \Omega\mu m$. This estimation indicates that an influence of the step height deviation is rather small and that more dominant processes must be present to account for the observed local variations of ρ_{step}.

Finally, if the deviations from the expected step heights were the reason for the local variations in step resistance, one would expect a quantitatively equally large spread in the measured data for single steps and double steps due to the underlying linear relationship between step height and step resistance. As this can be excluded from our data, we conclude that a variation in the step height does not play the dominant role for the resulting spread in ρ_{step}.

In the context of the n-i-n junction model, the length $\mathcal{L}$ of the depleted zone characterizes the pseudo-diffusive region, which finally determines ρ_{step}. More specific, $\mathcal{L}$ describes how quickly the transition from strong n-type doping, i.e., strong coupling to the substrate, to completely depleted of charge carriers, i.e., pseudo-diffusive, occurs. A slow transition results in a small $\mathcal{L}$ and, thus, in a small ρ_{step}. A large step resistance is measured, if the transition from n-type doping to pseudo-diffusive behavior occurs fast resulting in a large $\mathcal{L}$. The theoretical results of Low et al. are based on a capacitor model capturing the buffer layer and the graphene sheet.

A separation-dependent shift in the Fermi level was also investigated for metals close to a graphene sheet (more specific, the separation is in the range of the equilibrium distance $\mathrm{h_{eq}}$) [28,29]. In this case, a strong dependence on the properties of the specific metal was observed. For Al, a transition from strong n-type doping to charge neutral occurs over a change in graphene-metal-separation of 200 pm, whereas for Ag this transition takes place on a much shorter length scale of approximately 70 pm [28]. The situation resembles the case of graphene on top of a SiC substrate detaching in the vicinity of a substrate step resulting in a change in doping and highlights the crucial role of the specific electronic properties of the substrate.

For epitaxial graphene on SiC the carrier concentration of $\mathrm{n} \approx 1 \times 10^{13}\ \mathrm{cm}^{-2}$ with a Fermi energy of $\approx -400\ \mathrm{meV}$ above the Dirac point is a result of the polarization of the SiC substrate modified by the buffer or zero layer (ZL) [31]. As stated above, the basic idea behind the step resistance is the detachment of graphene, i.e. the increase of the distance between ZL and graphene layer, resulting in a region of lower carrier concentration. Within this framework, a variation in the step resistance has to be discussed as a variation in the change of the doping concentration or more specific in the transition length from doped to undoped region. This is sketched for two configuration in Figure 6.5 based on theoretical considerations by Low et al. [86].

In addition, Figure 6.5 shows and compares STS spectra ($\mathrm{T} = 8\ \mathrm{K}$) measured on two terraces connected by a double step with a large ρ_{step} (Figure 6.5a), and two STS spectra measured on two terraces connected by a double step with a small

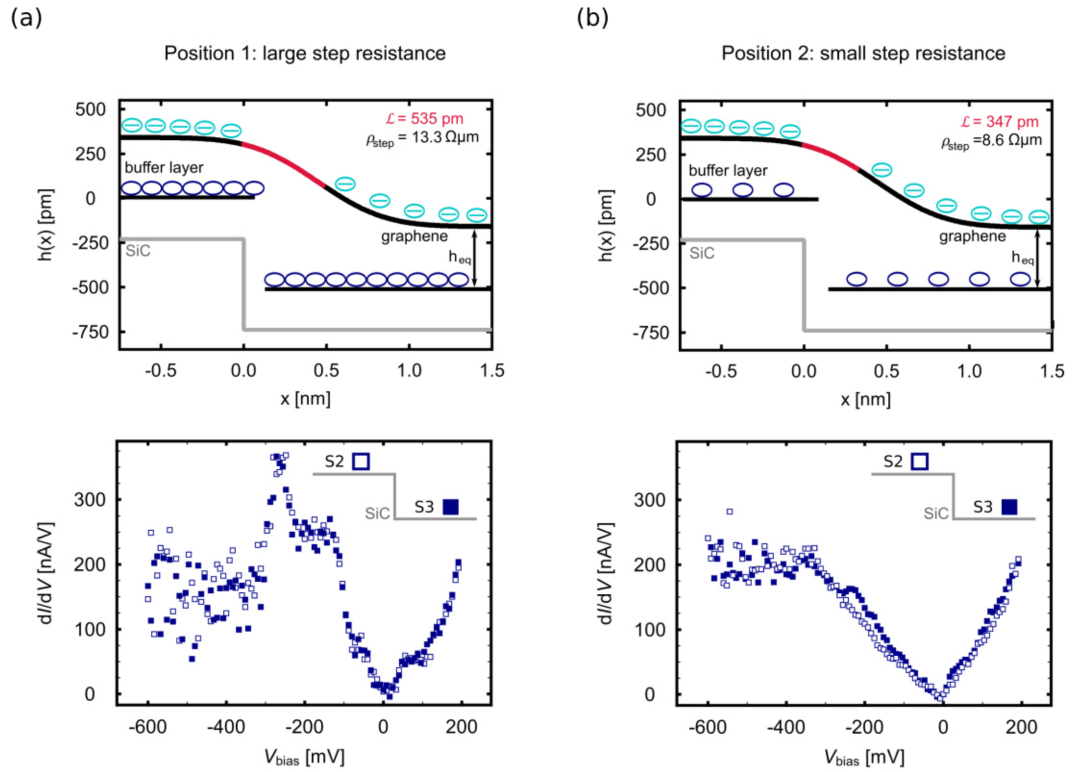

Figure 6.5 Side view of the calculated graphene and depletion zone geometries for different step configurations and corresponding STS spectra acquired on the adjacent terraces. (a) shows a step configuration with a large step resistance and (b) shows a step configuration with a small step resistance. Low et al. [86] showed that the geometry of the graphene sheet crossing a SiC substrate step can be approximated by an error function $h(x) \approx -\frac{h_{step}}{2}\left[\mathrm{erf}\left(\frac{x-x_s}{d_s}\right)+1\right]+h_{eq}$, where h_{step} is the step height of the substrate step and h_{eq} is the equilibrium distance between graphene and substrate, which is assumed to be 340 pm. Gray solid lines symbolize the respective substrate steps; the graphene layer is shown in black and the depleted region is marked in red. Blue ovals represent the interface states of the buffer layer and charge carriers in the graphene are shown in turquoise.

ρ_{step} (Figure 6.5b). To obtain this complete information, it is necessary to perform topographic as well as transport and also spectroscopic measurements at a fixed position. Due to the long measurement time to collect all the required information, this places high demands on the stability of the system. For this reason, we combined all methods only at $T = 8$ K. Furthermore, $T = 8$ K provides the best energetic resolution in spectroscopic measurements compared to $T = 77$ K and room temeprature. Overall, the spectra show similarities and are in agreement with published results [69,147]. Generally, dI/dV spectra of graphene on SiC are characterized by two prominent minima, one is the so-called pseudogap at 0 mV and the other is

a minimum at the position of the Dirac point [69]. However, the STS spectra for the two steps strongly deviate in the voltage range close to the Fermi Energy between -300 mV and 0 mV. Electronic states within this energy interval have been found to be associated with electronic states of the interface layer [33]. Connecting ρ_{step} and the LDOS, we find a clear correlation. For the step configuration with the larger ρ_{step}, the STS spectra show pronounced maxima in this energy range, while a smaller LDOS is found for smaller ρ_{step}.

We attribute this experimental correlation between DOS close to the Fermi energy and $\mathcal{L}$, i.e. the step resistance, to a more effective screening of the ZL with the higher DOS compared to the ZL with the lower DOS. Within this picture, the detachment of the graphene layer is accompanied with an local charge modification within the ZL states. From the experimental results we conclude that a larger DOS results in a more effective transistion as a function of distance d between graphene and ZL.

At this point we like to add two remarks. Firstly, the absolute value of d as well as the details of d as a function of the lateral position is expected to be influenced as the whole step configuration has to be in thermodynamical equilibrium (neglecting the small pertubation by the transport field). Secondly, our data show small deviations of the step height from the expected value given by the SiC lattice. This finding might also be attributed to the interplay between ZL and graphene layer.

For low temperature, we propose that in the case of SiC substrate steps, the transition from strong n-type doping to pseudo-diffusive behavior is controlled by electronic states near the Fermi energy. A high LDOS results in a laterally short switch between the differently doped areas resulting in a long pseudo-diffusive region and a large ρ_{step}. The presence of the pronounced spectral weight below the Fermi energy can be regarded as a manifestation of electronic states of the interface [33] that mediate the switching between n-type doping and pseudo-diffusive behavior. In the framework of this model, it is also reasonable that ρ_{step} shows quantitatively larger variations for double steps compared with single steps. The curvature of the graphene layer over a single step is smoother than over a double step. This leads to a less pronounced influence of the available states and, thus, a smaller variation in ρ_{step}. Our suggestion to include the local electronic environment in the description of the step resistance within the framework of the n-i-n model captures both

the variations in ρ_{step} for a given step configuration, single step or double step, as well as the quantitative differences in the variation for single and double steps.

We visualize the properties of the depleted region with respect to the geometry of the graphene sheet across a step for different configurations as shown in Figure 6.5 (see supplement in section 6.2.7 for details on the calculations). We mark the lengths $\mathcal{L}$ of the depleted regions corresponding to the respective ρ_{step} and find values of $\mathcal{L} = 535\ \mathrm{pm}$ for the step configuration with the larger ρ_{step} and $\mathcal{L} = 347\ \mathrm{pm}$ for the smaller ρ_{step}.

In contrast to the low-temperature behavior showing a decrease in ρ_{step} with increasing ρ_{sheet}, measurements at room temperature reveal the opposite trend: ρ_{step} increases with increasing ρ_{sheet}, both with respect to terraces S2 and with respect to terraces S3. The dependence of ρ_{step} on ρ_{sheet} on adjacent terraces with S2 and S3 agrees quantitatively reasonably well (as indicated by the dashed lines in Figure 6.3a). For epitaxial graphene on SiC it has been shown that especially at room temperature electron-phonon scattering is relevant [9]. It is dominated by the contribution of remote interfacial phonons [76]. As ρ_{step} and ρ_{sheet} follow a common trend, we suggest that the room temperature step resistance is similar to ρ_{sheet} affected by electron-phonon scattering.

6.2.4 Conclusion

Based on a detailed STP survey in combination with the high sample quality of PASG graphene, we have quantitatively studied the step resistance in epitaxial graphene on SiC for different temperatures. Using PASG graphene, we can exclude local variations of the current density as the main reason for the observed strong local variations of ρ_{step}, which have been reported in several studies. Instead we show that this variation is an intrinsic property, having different origins for low (8 K) and high (300 K) temperatures. At room temperature, the step resistance decreases with increasing sheet conductivity, whereas at low temperatures, an increase in sheet conductivity leads to an increase in the step resistance. We have utilized low temperature STS measurements to trace back the origin of these variations to the electronic states of the interface demonstrating the crucial influence of the substrate on the local properties of the step resistance.

This inversion from 300 K to 8 K is a priori surprising and indicates an intrinsic limit for the overall resistance. While with decreasing temperature a reduction of both electron-phonon scattering [9] and potential scattering [153] results in a decrease in $\Delta\rho_{\mathrm{sheet}}$, the built-up of a depletion zone in graphene carpeting surface steps becomes more efficient. We expect that our findings are not restricted to PASG graphene, but can be a guideline in optimizing the overall resistance in any epitaxially grown graphene sample.

6.2.5 Methods

6.2.5.1 Sample preparation

Graphene was grown on the (0001) Si-terminated face of semi-insulating 6H-SiC wafers with small nominal miscut angle of 0.06° towards $[1\bar{1}00]$ direction by applying the PASG technique [11,32]. The general concept of PASG is to use an external carbon source to support the growth process. Following this approach, a polymer was deposited onto the substrate using liquid phase deposition [11,32] before the high-temperature sublimation growth. The samples were annealed in vacuum ($p \approx 4 \cdot 10^{-7}$ mbar, 900°C, 30min) followed by two intermediate annealing steps in argon atmosphere (p = 900 mbar) at 1200°C and 1400°C for 10 minutes and 2 minutes, respectively. In the final step, the samples were heated up to 1750°C for 6 minutes (argon flux was kept at 0 sccm) [135].

6.2.5.2 Scanning probe measurements

We electrically contact the graphene samples (3mm x 7mm) with gold contacts with a thickness of 50 nm - 100 nm by thermal evaporation in a shadow mask procedure using a two-terminal geometry. In order to eliminate surface contamination after reinserting the samples into the UHV chamber, they are heated up to 400° C for 30 minutes. The STP measurements were performed in a custom-built low-temperature STM and in a custom-built room temperature STM under UHV conditions (base pressure $<10^{-10}$ mbar at $300\ \mathrm{K}$, $77\ \mathrm{K}$ and $8\ \mathrm{K}$) using electrochemically etched tungsten tips. For transport measurements, a voltage is applied across the sample using the two gold contacts. The additional voltage $\mathrm{V_{STP}(x,y)}$ at the tip is adjusted such that the net tunnel current $\mathrm{I_T}$ vanishes giving access to the electrochemical potential of the sample at the position of the tip. In order to obtain a potential map of the surface, $\mathrm{V_{STP}(x,y)}$ is recorded as a function of position [108]. As $\mathrm{V_{STP}(x,y)}$ is a measure of the local electrochemical potential, it gives access to the

local voltage drop along the graphene [108]. STS spectra were acquired using standard lock-in technique and a modulation amplitude of 10 mV.

6.2.6 Acknowledgements

Financial support of the Deutsche Forschungsgemeinschaft (DFG) through project We 1889/13-1 is gratefully acknowledged. The preparation of the samples was funded by the Deutsche Forschungsgemeinschaft (DFG) under Germany's Excellence Strategy – EXC-2123 QuantumFrontiers – 390837967.

6.2.7 Supplementary Information

6.2.7.1 Visualization of the depleted region

The geometry of the graphene sheet crossing a SiC substrate step and the built-up of a depletion zone at the position of the step have been discussed by Low et al. [86] As described in the manuscript, the geometry of the graphene sheet crossing a SiC substrate step can be approximated by an error function

$$h(x) \approx -\frac{h_{step}}{2}\left[\mathrm{erf}\left(\frac{x - x_s}{d_s}\right) + 1\right] + h_{eq} \tag{6.1}$$

where h_{step} is the step height of the substrate step and h_{eq} is the equilibrium distance between graphene and substrate, which is assumed to be 340pm, and h_{step} refers to the step height. The parameters x_s and d_s depend on h_{step} and are taken from Ref. [86]. For a double step, Low et al. determine the width of the region that is almost completely depleted of charge carriers to be $0.6\ \mathrm{nm}$ (from $x = 0.0\ \mathrm{nm}$ to $x = 0.6\ \mathrm{nm}$). For our calculations, we assume that this width translates to the step configuration with the largest step resistance with $\rho_{step} = 16.9\ \Omega\mu\mathrm{m}$ and calculate the corresponding arc length by inserting equation 6.1 into

$$\mathcal{L} = \int_a^b \sqrt{1 + (h'(x))^2}\, dx \tag{6.2}$$

and find for the length of the depleted region $\mathcal{L} = 677\mathrm{pm}$. As stated in the manuscript, we propose that this length $\mathcal{L}$ is affected by the local electronic environment. Based on the linear dependence of $\mathcal{L}$ on ρ_{step}, we calculate the length of the depleted region for other step configurations. Exploiting equation 6.1 and assuming that the point of the detachment is fixed at $x = 0.0\mathrm{nm}$, we visualize the properties of the depleted region as shown in the manuscript in Figure 6.5. The parameters x_s, d_s are extracted from Ref. [86], and are summarized in Table 4 for different step configurations.

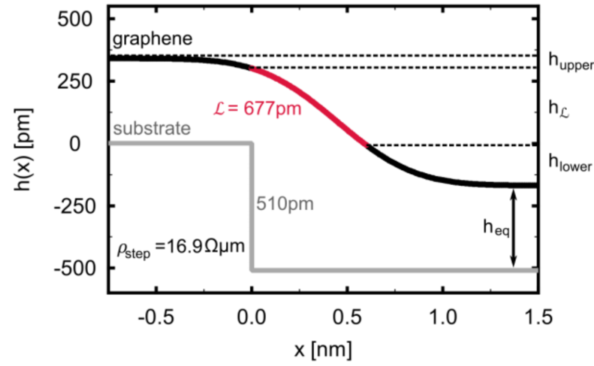

Figure 6.6 Side view of the calculated graphene geometry and definition of h_{upper}, $h_{\mathcal{L}}$ and h_{lower}.

To check the consistency of our calculations, we test for each step configuration that $h_{step} = h_{upper} + h_{\mathcal{L}} + h_{lower}$ with h_{upper}, $h_{\mathcal{L}}$ and h_{lower} as indicated in Figure 6.6.

Table 4: Summary of the parameter x_s, d_s, and $\mathcal{L}$ of the capacitor model for different step configurations.

h_{step} [pm]	ρ_{step} [Ω]	x_s [pm]	d_s [pm]	$\mathcal{L}$ [pm]
510	16.9	450	450	677
485	10.6	450	450	427
472	6.1	450	450	244
280	2.1	350	400	82
275	3.8	350	400	154
252	5.9	300	400	239

7 Big Picture

In recent years, great progress has been made in the growth processes of graphene on SiC. As a result, such samples were often regarded as homogeneous and well-defined systems with potential applications in quantum metrology [162]. Consequently, assuming a homogeneous sample, the properties of the entire graphene layer are described by single quantities, which do not depend on the position on the graphene. An example for this is the sheet resistance, which is extracted from macroscale measurements and is supposed to characterize the electrical properties of the entire graphene layer.

For mesoscopic scales, in section 3 we determine the residual anisotropy of the resistance for high-quality monolayer graphene on SiC prepared by the PASG growth method. We find an anisotropy as low as 2%, which is evidence of the significant improvement in graphene growth. By combining mesoscopic and local transport measurements, we could identify the origin of this remaining anisotropy. It is due to scattering at SiC substrate steps, which are aligned in good approximation parallel to each other. As the presence of SiC substrate steps is unavoidable for graphene on SiC, the residual anisotropy represents an intrinsic limit in the optimization of the resistance anisotropy.

For the local scale, in the literature, parameters such as the local sheet resistance and the local defect resistance are found to vary largely [68]. In the context of local transport measurements, it is not possible to distinguish whether such a variation actually arises from locally varying resistances or merely from uncertainties in the current density. It has been shown in this thesis that this problem is solved with the availability of PASG graphene. The choice of the PASG growth method allows atomic-scale quantities, such as the local sheet resistance or the defect resistance, to be measured quantitatively. This is enabled by the absence of bilayer graphene in PASG graphene which leads to a homogeneous local current density. Furthermore, for PASG graphene, different graphene terraces can be directly and unambiguously correlated with the stacking sequence of the SiC substrate.

Surprisingly, however, in this thesis it was found that many material quantities that were previously assumed to be constant instead exhibit strong local variations. An

example of this is the step height. Although SiC is known to have a step height of multiples of 250 pm [52], it turned out that there are significant deviations from this defined height in the case of graphene on SiC. These step height variations were explained by a local variation in the distance between the graphene and the substrate. This is a clear indication that the generally accepted picture of graphene on SiC being a homogeneous system does not hold. Instead, local proximity effects play a crucial role. It was shown further that besides the step height also the local sheet resistance as well as the defect resistance of substrate steps exhibit local variations. Basically, all these variations can be traced back to proximity coupling of the graphene with the buffer layer and the SiC substrate.

Proximity effects like the substrate-induced strong n-type doping of graphene on SiC were known, but the view of this type of interaction was limited to the idea that these proximity effects lead to a homogeneous change in the properties of the graphene layer in the sense that every location in the graphene is affected to the same extent by this interaction. In this thesis, this way of thinking is challenged and a new view on proximity effects in graphene on SiC is opened.

Explicitly, this thesis aims at understanding local proximity effects in graphene on SiC and to answer questions like ‘How homogeneous is epitaxial graphene on SiC regarding charge transport on the local scale?’ and ‘What is the origin of the quantitative spread in the defect resistance assigned to substrate steps in the literature?’.

It was shown that the sheet resistance in graphene on SiC is not a constant quantity, but that it is subject to strong local variations of up to 270% at low temperatures. The reasons for these local variations are, on the one hand, the different terminations of the SiC substrate and, on the other hand, a local variation of the distance between graphene and substrate.

Moreover, it was found that also the defect resistance of SiC substrate steps exhibits strong intrinsic variations. By linking the transport data with STS measurements, we concluded that the origin of these variations in the step resistance are local variations in the interface states, once again highlighting the crucial impact of the substrate and proximity coupling on graphene’s properties.

Despite the presence of these variations in the sheet resistance as well as the defect resistance, no change in doping was found for graphene on terraces S2

compared to terraces S3 based on the position of the Dirac point in STS spectra and consistent with our KPFM measurements.

In summary, although there are many experimental and theoretical studies on epitaxial graphene on SiC (see e.g. [36] for a thorough review), proximity effects in graphene have not yet been considered to exhibit local variations, nor have they been quantified. This thesis successfully extends the existing view on substrate-graphene interactions by demonstrating that the step height and the sheet resistance as well as the defect resistance are subject to strong local variations induced by local variations in the coupling between the graphene and the substrate. This new perspective clearly emphasizes the relevance of spatially-resolved studies for a comprehensive understanding of proximity effects in graphene on SiC.

7.1 Outlook

Based on the new view on proximity effects in graphene on SiC elaborated in this thesis, several systematic studies can be carried out on this topic. In the following, three follow-up research focuses are suggested.

Doping and distance variation

- It seems worthwhile to perform a detailed investigation of the global as well as the local doping of epitaxial graphene on SiC with the aim to understand why this thesis comes to a different result regarding local doping than Ref. [54].
- STS spectra show interface states at small negative bias voltages. In addition, local variations in the distance between the graphene layer and the substrate were observed. Possibly, the distance between the graphene and the buffer layer is adjusted depending on the interface states such that a constant doping with a charge carrier concentration of roughly $1 \times 10^{13}\ \mathrm{cm}^{-2}$ is present [31]. With a combination of STM, STS and KPFM this aspect could be investigated in more detail with the aim to develop a more quantitative picture of the intrinsic doping process in graphene on SiC.

Input for sample optimization

- It seems worthwhile to investigate the substrate induced transport properties in more detail, e.g., by considering the influence of different growth parameters. This approach could allow for a better understanding of the interface between graphene and the SiC substrate. As a starting point, one could change the polytype of the SiC substrate from 6H-SiC to 4H-SiC. By investigating the temperature dependence of the sheet resistance for differently grown epitaxial graphene on SiC samples, it may be possible to develop a deeper understanding of the dominant scattering processes. This knowledge could eventually serve to provide important input for sample optimization.
- Combining local conductivity with defect resistances and doping insights, a comprehensive understanding of proximity effects including the properties of the buffer layer or electron-phonon scattering in epitaxial graphene on SiC comes within reach. This may even open up the possibility of improving the generally low carrier mobility in epitaxial graphene.

Tuning based on intercalation

- Furthermore, a comprehensive understanding might enable tuning of the properties of graphene by exploiting extrinsic proximity effects in the sense that elements with certain properties are brought deliberately close to the graphene, e.g., by intercalation in a targeted and predictable manner.
- Following the idea to tailor the electronic properties of a graphene sheet by intercalation, the intercalation process has successfully been demonstrated for a wide range of atomic species beyond hydrogen such as Cu [17], Au [18], Ge [19], F [20], Pb [21] or Pd [22]. Each of these elements induces its unique interactions, thereby changing the properties of the graphene. Intercalated graphene samples have been studied intensively applying different techniques [14,17–22,56] including macroscopic transport measurements [16], however, atomic-scale transport studies are still missing. Extending the approach of locally resolved transport measurements to the wide range of intercalated systems would provide a new perspective on these types of systems with their diverse properties depending on the intercalated species.

Bibliography

1. Tung, R. T. The physics and chemistry of the Schottky barrier height. *Appl. Phys. Rev.* **1**, 011304 (2014).
2. Harris, J. J. Delta-doping of semiconductors. *J. Mater. Sci. Mater. Electron.* **4**, 93–105 (1993).
3. Holm, R. & Meissner, W. Messungen mit Hilfe von flüssigem Helium. XIII. *Zeitschrift für Physik.* **74**, 715–735 (1932).
4. De Gennes, P. G. *Superconductivity Of Metals And Alloys*. CRC Press, (1999).
5. Mammadov, S. *et al.* Polarization doping of graphene on silicon carbide. *2D Mater.* **1**, 035003 (2014).
6. Zhou, S. Y. *et al.* Substrate-induced bandgap opening in epitaxial graphene. *Nat. Mater.* **6**, 770–775 (2007).
7. Shen, T. *et al.* Observation of quantum-Hall effect in gated epitaxial graphene grown on SiC (0001). *Appl. Phys. Lett.* **95**, 10–13 (2009).
8. Tzalenchuk, A. *et al.* Towards a quantum resistance standard based on epitaxial graphene. *Nat. Nanotechnol.* **5**, 186–189 (2010).
9. Jobst, J. *et al.* Quantum oscillations and quantum Hall effect in epitaxial graphene. *Phys. Rev. B* **81**, 195434 (2010).
10. Emtsev, K. V. *et al.* Towards wafer-size graphene layers by atmospheric pressure graphitization of silicon carbide. *Nat. Mater.* **8**, 203–207 (2009).
11. Kruskopf, M. *et al.* Comeback of epitaxial graphene for electronics: Large-area growth of bilayer-free graphene on SiC. *2D Mater.* **3**, 041002 (2016).
12. Dean, C. R. *et al.* Boron nitride substrates for high-quality graphene electronics. *Nat. Nanotechnol.* **5**, 722–726 (2010).
13. Bolotin, K. I. *et al.* Ultrahigh electron mobility in suspended graphene. *Solid State Commun.* **146**, 351–355 (2008).
14. Speck, F. *et al.* The quasi-free-standing nature of graphene on H-saturated SiC(0001). *Appl. Phys. Lett.* **99**, 122106 (2011).
15. Riedl, C., Coletti, C., Iwasaki, T., Zakharov, A. A. & Starke, U. Quasi-free-standing epitaxial graphene on SiC obtained by hydrogen intercalation. *Phys. Rev. Lett.* **103**, 246804 (2009).
16. Jobst, J. *Quantum Transport in Epitaxial Graphene on Silicon Carbide (0001)*. PhD thesis, Friedrich-Alexander-Universität Erlangen-Nürnberg (2013).
17. Yagyu, K. *et al.* Fabrication of a single layer graphene by copper intercalation on a SiC(0001) surface. *Appl. Phys. Lett.* **104**, 053115 (2014).
18. Gierz, I. *et al.* Electronic decoupling of an epitaxial graphene monolayer by gold intercalation. *Phys. Rev. B* **81**, 235408 (2010).
19. Emtsev, K. V., Zakharov, A. A., Coletti, C., Forti, S. & Starke, U. Ambipolar

doping in quasifree epitaxial graphene on SiC(0001) controlled by Ge intercalation. *Phys. Rev. B* **84**, 125423 (2011).

20. Wong, S. L. *et al.* Quasi-free-standing epitaxial graphene on SiC (0001) by fluorine intercalation from a molecular source. *ACS Nano* **5**(9), 7662–7668 (2011).

21. Yurtsever, A. *et al.* Effects of Pb Intercalation on the Structural and Electronic Properties of Epitaxial Graphene on SiC. *Small* **12**(29), 3956–3966 (2016).

22. Yagyu, K., Takahashi, K., Tochihara, H., Tomokage, H. & Suzuki, T. Neutralization of an epitaxial graphene grown on a SiC(0001) by means of palladium intercalation. *Appl. Phys. Lett.* **110**, 131602 (2017).

23. Ge, J. L. *et al.* Weak localization of bismuth cluster-decorated graphene and its spin–orbit interaction. *Front. Phys.* **12**(4), 127210 (2017).

24. Avsar, A. *et al.* Spin-orbit proximity effect in graphene. *Nat. Commun.* **5**, 4875 (2014).

25. Song, K. *et al.* Spin Proximity Effects in Graphene/Topological Insulator Heterostructures. *Nano Lett.* **18**, 2033–2039 (2018).

26. Haugen, H., Huertas-Hernando, D. & Brataas, A. Spin transport in proximity-induced ferromagnetic graphene. *Phys. Rev. B* **77**, 115406 (2008).

27. Tang, C. *et al.* Approaching quantum anomalous Hall effect in proximity-coupled YIG/graphene/h-BN sandwich structure. *APL Mater.* **6**, 026401 (2018).

28. Giovannetti, G. *et al.* Doping graphene with metal contacts. *Phys. Rev. Lett.* **101**, 026803 (2008).

29. Khomyakov, P. A. *et al.* First-principles study of the interaction and charge transfer between graphene and metals. *Phys. Rev. B* **79**, 195425 (2009).

30. Natterer, F. D. *et al.* Scanning tunneling spectroscopy of proximity superconductivity in epitaxial multilayer graphene. *Phys. Rev. B* **93**, 045406 (2016).

31. Ristein, J., Mammadov, S. & Seyller, T. Origin of doping in quasi-free-standing graphene on silicon carbide. *Phys. Rev. Lett.* **108**, 246104 (2012).

32. Momeni Pakdehi, D. *et al.* Minimum Resistance Anisotropy of Epitaxial Graphene on SiC. *ACS Appl. Mater. Interfaces* **10**, 6039–6045 (2018).

33. Sinterhauf, A. *et al.* Substrate induced nanoscale resistance variation in epitaxial graphene. *Nat. Commun.* **11**, 555 (2020).

34. Sinterhauf, A. *et al.* Unraveling the origin of local variations in the step resistance of epitaxial graphene on SiC: a quantitative Scanning Tunneling Potentiometry study. *Carbon* **184**, 463–469 (2021).

35. Foa Torres, L. E. F., Roche, S. & Charlier, J.-C. *Introduction to Graphene-Based Nanomaterials*. Cambridge University Press (2014)

36. Berger, C., Conrad, E. H. & De Heer, W. A. Epigraphene: epitaxial graphene on silicon carbide. in *Physics of solid surfaces* (eds. Chiarotti, G. & Chiaradia, P.), Springer Verlag (2017).

37. Novoselov, K. S. *et al.* Electric Field Effect in Atomically Thin Carbon Films. *Science* **306**, 666–669 (2004).

38. Wang, H., Zhao, Y., Xie, Y., Ma, X. & Zhang, X. Recent progress in synthesis

of two-dimensional hexagonal boron nitride. *Journal of. Semiconductors* **38**, 031003 (2017).

39. Wallace, P. R. The band theory of graphite. *Phys. Rev.* **71**, 622 (1947).

40. Sutter, P. W., Flege, J. I. & Sutter, E. A. Epitaxial graphene on ruthenium. *Nat. Mater.* **7**, 406–411 (2008).

41. Coraux, J., N'Diaye, A. T., Busse, C. & Michely, T. Structural coherency of graphene on Ir(111). *Nano Lett.* **8**(2), 565–570 (2008).

42. Li, X. *et al.* Large-area synthesis of high-quality and uniform graphene films on copper foils. *Science* **324**, 1312–1314 (2009).

43. Vita, H. *et al.* Understanding the origin of band gap formation in graphene on metals: Graphene on Cu/Ir(111). *Sci. Rep.* **4**, 5704 (2014).

44. Hattab, H. *et al.* Interplay of wrinkles, strain, and lattice parameter in graphene on iridium. *Nano Lett.* **12**(2), 678–682 (2012).

45. Lukosius, M. *et al.* Metal-Free CVD Graphene Synthesis on 200 mm Ge/Si(001) Substrates. *ACS Appl. Mater. Interfaces* **8**, 33786–33793 (2016).

46. Sinterhauf, A. *et al.* A comprehensive study of charge transport in Au-contacted graphene on Ge/Si(001). *Appl. Phys. Lett.* **117**, 023104 (2020).

47. Aprojanz, J. *et al.* High-Mobility Epitaxial Graphene on Ge/Si(100) Substrates. *ACS Appl. Mater. Interfaces* **12**, 43065–43072 (2020).

48. Schardt, J. *et al.* LEED structure determination of hexagonal α-SiC surfaces. *Surf. Sci.* **337**, 232–242 (1995).

49. Park, C. H., Cheong, B. H., Lee, K. H. & Chang, K. J. Structural and electronic properties of cubic, 2H, 4H, and 6H SiC. *Phys. Rev. B* **49**(7), 4485–4493 (1994).

50. Hristu, R., Stanciu, S. G., Tranca, D. E., Polychroniadis, E. K. & Stanciu, G. A. Identification of stacking faults in silicon carbide by polarization-resolved second harmonic generation microscopy. *Sci. Rep.* **7**, 4870 (2017).

51. Seyller, T. Passivation of hexagonal SiC surfaces by hydrogen termination. *J. Phys. Condens. Matter* **16**, S1755-S1782 (2004).

52. Yazdi, G. R. *et al.* Growth of large area monolayer graphene on 3C-SiC and a comparison with other SiC polytypes. *Carbon* **57**, 477–484 (2013).

53. Borovikov, V. & Zangwill, A. Step bunching of vicinal 6H-SiC{0001} surfaces. *Phys. Rev. B* **79**, 245413 (2009).

54. Momeni Pakdehi, D. *et al.* Silicon Carbide Stacking-Order-Induced Doping Variation in Epitaxial Graphene. *Adv. Funct. Mater.* **30**, 2004695 (2020).

55. Emtsev, K. V., Speck, F., Seyller, T., Ley, L. & Riley, J. D. Interaction, growth, and ordering of epitaxial graphene on SiC{0001} surfaces: A comparative photoelectron spectroscopy study. *Phys. Rev. B* **77**, 155303 (2008).

56. Guisinger, N. P., Rutter, G. M., Crain, J. N., First, P. N. & Stroscio, J. A. Exposure of epitaxial graphene on SiC(0001) to atomic hydrogen. *Nano Lett.* **9**(4), 1462–1466 (2009).

57. Riedl, C., Starke, U., Bernhardt, J., Franke, M. & Heinz, K. Structural properties of the graphene-SiC(0001) interface as a key for the preparation of homogeneous large-terrace graphene surfaces. *Phys. Rev. B* **76**, 245406

(2007).

58. Rutter, G. M. *et al.* Imaging the interface of epitaxial graphene with silicon carbide via scanning tunneling microscopy. *Phys. Rev. B* **76**, 235416 (2007).

59. Mallet, P. *et al.* Electron states of mono- and bilayer graphene on SiC probed by scanning-tunneling microscopy. *Phys. Rev. B* **76**, 041403(R) (2007).

60. Kim, S., Ihm, J., Choi, H. J. & Son, Y. W. Origin of anomalous electronic structures of epitaxial graphene on silicon carbide. *Phys. Rev. Lett.* **100**, 176802 (2008).

61. Van Bommel, A. J., Crombeen, J. E. & Van Tooren, A. LEED and Auger electron observations of the SiC(0001) surface. *Surf. Sci.* **48**, 463–472 (1975).

62. Berger, C. *et al.* Ultrathin epitaxial graphite: 2D electron gas properties and a route toward graphene-based nanoelectronics. *J. Phys. Chem. B* **108**, 19912–19916 (2004).

63. Seyller, T. *et al.* Structural and electronic properties of graphite layers grown on SiC(0001). *Surf. Sci.* **600**, 3906–3911 (2006).

64. Hibino, H. *et al.* Microscopic thickness determination of thin graphite films formed on SiC from quantized oscillation in reflectivity of low-energy electrons. *Phys. Rev. B* **77**, 075413 (2008).

65. Kruskopf, M. *et al.* A morphology study on the epitaxial growth of graphene and its buffer layer. *Thin Solid Films* **659**, 7–15 (2018).

66. Sommerfeld, A. & Bethe, H. Elektronentheorie der Metalle. in *Handbuch der Physik - Aufbau der zusammenhängenden Materie* 333–622 (1933).

67. Hunklinger, S. *Festkörperphysik*. Oldenbourg Verlag, 4. Auflage (2014).

68. Willke, P., Schneider, M. A. & Wenderoth, M. Electronic Transport Properties of 1D-Defects in Graphene and Other 2D-Systems. *Ann. Phys.* **529**, 1700003 (2017).

69. Willke, P. *et al.* Doping of Graphene by Low-Energy Ion Beam Implantation: Structural, Electronic, and Transport Properties. *Nano Lett.* **15**(8), 5110–5115 (2015).

70. Mendoza, M., Herrmann, H. J. & Succi, S. Hydrodynamic model for conductivity in graphene. *Sci. Rep.* **3**, 1052 (2013).

71. Du, X., Skachko, I., Duerr, F., Luican, A. & Andrei, E. Y. Fractional quantum Hall effect and insulating phase of Dirac electrons in graphene. *Nature* **462**, 192–195 (2009).

72. Jobst, J., Waldmann, D., Gornyi, I. V., Mirlin, A. D. & Weber, H. B. Electron-electron interaction in the magnetoresistance of graphene. *Phys. Rev. Lett.* **108**, 106601 (2012).

73. Cooper, D. R. *et al.* Experimental Review of Graphene. *ISRN Condens. Matter Phys.* **2012**, 501686 (2012).

74. Tikhonenko, F. V., Kozikov, A. A., Savchenko, A. K. & Gorbachev, R. V. Transition between electron localization and antilocalization in graphene. *Phys. Rev. Lett.* **103**, 226801 (2009).

75. Chen, J. H., Jang, C., Xiao, S., Ishigami, M. & Fuhrer, M. S. Intrinsic and extrinsic performance limits of graphene devices on SiO 2. *Nat.*

Nanotechnol. **3**, 206–209 (2008).

76. Fratini, S. & Guinea, F. Substrate-limited electron dynamics in graphene. *Phys. Rev. B* **77**, 195415 (2008).

77. Tanabe, S., Sekine, Y., Kageshima, H., Nagase, M. & Hibino, H. Carrier transport mechanism in graphene on SiC(0001). *Phys. Rev. B* **84**, 115458 (2011).

78. Wang, S. Q. & Mahan, G. D. Electron Scattering from Surface Excitations. *Phys. Rev. B* **6**, 4517–4526 (1972).

79. Perebeinos, V., Rotkin, S. V., Petrov, A. G. & Avouris, P. The effects of substrate phonon mode scattering on transport in carbon nanotubes. *Nano Lett.* **9**(1), 312–316 (2009).

80. Willke, P. *et al.* Local transport measurements in graphene on SiO_2 using Kelvin probe force microscopy. *Carbon* **102**, 470–476 (2016).

81. Landauer, R. Spatial variation of currents and fields due to localized scatterers in metallic conduction. *IBM J. Res. Dev.* **1**, 223–231 (1957).

82. Druga, T. Graphen auf Siliziumcarbid: elektronische Eigenschaften und Ladungstransport. PhD thesis, Georg-August-Universität Göttingen (2014).

83. Di Ventra, M. *Electrical Transport in Nanoscale Systems*. Cambridge University Press (2008).

84. Willke, P., Druga, T., Ulbrich, R. G., Schneider, M. A. & Wenderoth, M. Spatial extent of a Landauer residual-resistivity dipole in graphene quantified by scanning tunnelling potentiometry. *Nat. Commun.* **6**, 6399 (2015).

85. Ji, S. H. *et al.* Atomic-scale transport in epitaxial graphene. *Nat. Mater.* **11**, 114–119 (2012).

86. Low, T., Perebeinos, V., Tersoff, J. & Avouris, P. Deformation and scattering in graphene over substrate steps. *Phys. Rev. Lett.* **108**, 096601 (2012).

87. Clark, K. W. *et al.* Spatially resolved mapping of electrical conductivity across individual domain (Grain) boundaries in graphene. *ACS Nano* **7**(9), 7956–7966 (2013).

88. Ciuk, T. *et al.* Step-edge-induced resistance anisotropy in quasi-free-standing bilayer chemical vapor deposition graphene on SiC. *J. Appl. Phys.* **116**, 123708 (2014).

89. Willke, P., Kotzott, T., Pruschke, T. & Wenderoth, M. Magnetotransport on the nano scale. *Nat. Commun.* **8**, 15283 (2017).

90. Homoth, J. Das elektrochemische Potential auf der atomaren Skala: Untersuchung des Ladungstransports eines stromtragenden zweidimensionalen Elektronengases mit Hilfe der Rastertunnelpotentiometrie. PhD thesis, Georg-August-Universität Göttingen (2008).

91. Hofer, C. *et al.* Direct imaging of light-element impurities in graphene reveals triple-coordinated oxygen. *Nat. Commun.* **10**, 4570 (2019).

92. Hashimoto, A., Suenaga, K., Gloter, A., Urita, K. & Iijima, S. Direct evidence for atomic defects in graphene layers. *Nature* **430**, 870–873 (2004).

93. Bostwick, A., Ohta, T., Seyller, T., Horn, K. & Rotenberg, E. Quasiparticle dynamics in graphene. *Nat. Phys.* **3**, 36–40 (2007).

94. First, P. N. *et al.* Epitaxial graphenes on silicon carbide. *MRS Bull.* **35**, 296–305 (2010).

95. Chen, C. J. *Introduction to Scanning Tunneling Microscopy*. Oxford Univ. Press (1993).

96. Willke, P. Atomic-scale transport in graphene : the role of localized defects and substitutional doping. PhD thesis, Georg-August-Universität Göttingen (2016).

97. Hamers, R. J. Atomic-resolution surface spectroscopy with the scanning tunneling microscope. *Annu. Rev. Phys. Chem.* **40**, 531–559 (1989).

98. Voigtländer, B. *Atomic force microscopy*. *Springer Verlag, 2. Auflage (2019)*

99. Wiesendanger, R. Scanning probe microscopy and spectroscopy: methods and applications. *Cambridge University Press* (1994).

100. Prüser, H. Scanning Tunneling Spectroscopy of Magnetic Bulk Impurities. PhD thesis, Georg-August-Universität Göttingen (2013).

101. Druga, T., Wenderoth, M., Lüpke, F. & Ulbrich, R. G. Graphene-metal contact resistivity on semi-insulating 6H-SiC(0001) measured with Kelvin probe force microscopy. *Appl. Phys. Lett.* **103**, 051601 (2013).

102. Curtin, A. E. *et al.* Kelvin probe microscopy and electronic transport in graphene on SiC(0001) in the minimum conductivity regime. *Appl. Phys. Lett.* **98**, 243111 (2011).

103. Eriksson, J. *et al.* The influence of substrate morphology on thickness uniformity and unintentional doping of epitaxial graphene on SiC. *Appl. Phys. Lett.* **100**, 241607 (2012).

104. Zerweck, U., Loppacher, C., Otto, T., Grafström, S. & Eng, L. M. Accuracy and resolution limits of Kelvin probe force microscopy. *Phys. Rev. B* **71**, 125424 (2005).

105. Miccoli, I., Edler, F., Pfnür, H. & Tegenkamp, C. The 100th anniversary of the four-point probe technique: The role of probe geometries in isotropic and anisotropic systems. *J. Phys. Condens. Matter* **27**, 223201 (2015).

106. Muralt, P. & Pohl, D. W. Scanning tunneling potentiometry. *Appl. Phys. Lett.* **48**, 514–516 (1986).

107. Besocke, K. An easily operable scanning tunneling microscope. *Surf. Sci.* **181**, 145–153 (1987).

108. Druga, T., Wenderoth, M., Homoth, J., Schneider, M. A. & Ulbrich, R. G. A versatile high resolution scanning tunneling potentiometry implementation. *Rev. Sci. Instrum.* **81**, 083704 (2010).

109. Potter, R. I. Magnetoresistance anisotropy in ferromagnetic NiCu alloys. *Phys. Rev. B* **10**, 4626–4636 (1974).

110. Mittendorff, M. *et al.* Anisotropy of excitation and relaxation of photogenerated charge carriers in graphene. *Nano Lett.* **14**(3), 1504–1507 (2014).

111. Almeida, C. M. *et al.* Giant and tunable anisotropy of nanoscale friction in graphene. *Sci. Rep.* **6**, 31569 (2016).

112. Homoth, J. *et al.* Electronic transport on the nanoscale: Ballistic transmission and Ohm's law. *Nano Lett.* **9**(4), 1588–1592 (2009).

113. Avouris, P. & Dimitrakopoulos, C. Graphene: Synthesis and applications.

Mater. Today **15**(3), 86–97 (2012).

114. Lin, Y. M. *et al.* Enhanced performance in epitaxial graphene FETs with optimized channel morphology. *IEEE Electron Device Lett.* **32**, 1343–1345 (2011).

115. Tan, Y. W. *et al.* Measurement of scattering rate and minimum conductivity in graphene. *Phys. Rev. Lett.* **99**, 246803 (2007).

116. Odaka, S. *et al.* Anisotropic transport in graphene on SiC substrate with periodic nanofacets. *Appl. Phys. Lett.* **96**, 062111 (2010).

117. Kobayashi, K. *et al.* Resistivity Anisotropy Measured Using Four Probes in Epitaxial Graphene on Silicon Carbide. *Appl. Phys. Express* **8**, 036602 (2015).

118. Schumann, T. *et al.* Anisotropic quantum Hall effect in epitaxial graphene on stepped SiC surfaces. *Phys. Rev. B* **85**, 235402 (2012).

119. Pallecchi, E. *et al.* High electron mobility in epitaxial graphene on 4H-SiC(0001) via post-growth annealing under hydrogen. *Sci. Rep.* **4**, 4558 (2014).

120. Yakes, M. K. *et al.* Conductance Anisotropy in Epitaxial Graphene Sheets Generated by Substrate Interactions. *Nano Lett.* 10, 1559–1562 (2010).

121. Robinson, J. *et al.* Nucleation of epitaxial graphene on SiC(0001). *ACS Nano* **4**(1), 153–158 (2010).

122. Nagase, M., Hibino, H., Kageshima, H. & Yamaguchi, H. Local conductance measurements of double-layer graphene on SiC substrate. *Nanotechnology* **20**, 445704 (2009).

123. Giannazzo, F., Deretzis, I., La Magna, A., Roccaforte, F. & Yakimova, R. Electronic transport at monolayer-bilayer junctions in epitaxial graphene on SiC. *Phys. Rev. B* **86**, 235422 (2012).

124. Clark, K. W. *et al.* Energy gap induced by friedel oscillations manifested as transport asymmetry at Monolayer-Bilayer graphene boundaries. *Phys. Rev. X* **4**, 011021 (2014).

125. Iagallo, A. *et al.* Bilayer-induced asymmetric quantum Hall effect in epitaxial graphene. *Semicond. Sci. Technol.* **30**, 055007 (2015).

126. Chua, C. *et al.* Quantum hall effect and quantum point contact in bilayer-patched epitaxial graphene. *Nano Lett.* **14**(6), 3369–3373 (2014).

127. Kruskopf, M. *et al.* Modification of Structural and Electron Transport Properties by Substrate Pretreatment. *J. Phys. Condens. Matter.* **27**, 185303 (2015).

128. Ostler, M., Speck, F., Gick, M. & Seyller, T. Automated preparation of high-quality epitaxial graphene on 6H-SiC(0001). *Phys. Status Solidi B* **247**, 2924–2926 (2010).

129. Ul Hassan, J. *et al.* Surface evolution of 4H-SiC(0001) during in-situ surface preparation and its influence on graphene properties. *Mater. Sci. Forum* **740–742**, 157–160 (2013).

130. Chien, F. R., Nutt, S. R., Yoo, W. S., Kimoto, T. & Matsunami, H. Terrace growth and polytype development in epitaxial β-SiC films on α-SiC (6H and 15R) substrates. *J. Mater. Res.* **9**(4), 940–954 (1994).

131. Baringhaus, J. *et al.* Local transport measurements on epitaxial graphene.

Appl. Phys. Lett. **103**, 111604 (2013).

132. Kanagawa, T. *et al.* Anisotropy in Conductance of a Quasi-One-Dimensional Metallic Surface State Measured by a Square Micro-Four-Point Probe Method. *Phys. Rev. Lett.* **91**, 036805 (2003).

133. Lara-Avila, S. *et al.* Non-volatile photochemical gating of an epitaxial graphene/polymer heterostructure. *Adv. Mater.* **23**, 878–882 (2011).

134. Lee, D. S. *et al.* Raman spectra of epitaxial graphene on SiC and of epitaxial graphene transferred to SiO2. *Nano Lett.* **8**(12), 4320–4325 (2008).

135. Momeni Pakdehi, D. *et al.* Homogeneous Large-Area Quasi-Free-Standing Monolayer and Bilayer Graphene on SiC. *ACS Appl. Nano Mater.* **2**, 844–852 (2019).

136. Wang, Z. jun *et al.* Simultaneous N-intercalation and N-doping of epitaxial graphene on 6H-SiC(0001) through thermal reactions with ammonia. *Nano Res.* **6**(6), 399–408 (2013).

137. Baringhaus, J. *et al.* Bipolar gating of epitaxial graphene by intercalation of Ge. *Appl. Phys. Lett.* **104**, 261602 (2014).

138. Baringhaus, J., Stöhr, A., Forti, S., Starke, U. & Tegenkamp, C. Ballistic bipolar junctions in chemically gated graphene ribbons. *Sci. Rep.* **5**, 9955 (2015).

139. Ella, L. *et al.* Simultaneous voltage and current density imaging of flowing electrons in two dimensions. *Nat. Nanotechnol.* **14**, 480–487 (2019).

140. Jobst, J. *et al.* Transport properties of high-quality epitaxial graphene on 6H-SiC(0001). *Solid State Commun.* **151**, 1061–1064 (2011).

141. Riedl, C., Coletti, C. & Starke, U. Structural and electronic properties of epitaxial Graphene on SiC(0001): A review of growth, characterization, transfer doping and hydrogen intercalation. *J. Phys. D. Appl. Phys.* **43**, 374009 (2010).

142. Sclauzero, G. & Pasquarello, A. Stability and charge transfer at the interface between SiC(0001) and epitaxial graphene. *Microelectron. Eng.* **88**, 1478–1481 (2011).

143. Červenka, J., Van De Ruit, K. & Flipse, C. F. J. Giant inelastic tunneling in epitaxial graphene mediated by localized states. *Phys. Rev. B* **81**, 205403 (2010).

144. Conrad, M. *et al.* Structure and evolution of semiconducting buffer graphene grown on SiC(0001). *Phys. Rev. B* **96**, 195304 (2017).

145. Gruschwitz, M., Schletter, H., Schulze, S., Alexandrou, I. & Tegenkamp, C. Epitaxial graphene on 6H-SiC(0001): Defects in SiC investigated by STEM. *Phys. Rev. Mater.* **3**, 094004 (2019).

146. Joucken, F. *et al.* Localized state and charge transfer in nitrogen-doped graphene. *Phys. Rev. B* **85**, 161408(R) (2012).

147. Brar, V. W. *et al.* Scanning tunneling spectroscopy of inhomogeneous electronic structure in monolayer and bilayer graphene on SiC. *Appl. Phys. Lett.* **91**, 122102 (2007).

148. Varchon, F. *et al.* Electronic structure of epitaxial graphene layers on SiC: Effect of the substrate. *Phys. Rev. Lett.* **99**, 126805 (2007).

149. Du, X., Skachko, I., Barker, A. & Andrei, E. Y. Approaching ballistic transport

in suspended graphene. *Nat. Nanotechnol.* **3**, 491–495 (2008).

150. Hwang, E. H. & Das Sarma, S. Screening-induced temperature-dependent transport in two-dimensional graphene. *Phys. Rev. B* **79**, 165404 (2009).

151. Das Sarma, S. & Hwang, E. H. Density-dependent electrical conductivity in suspended graphene: Approaching the Dirac point in transport. *Phys. Rev. B* **87**, 035415 (2013).

152. Kotov, V. N., Uchoa, B., Pereira, V. M., Guinea, F. & Castro Neto, A. H. Electron-electron interactions in graphene: Current status and perspectives. *Rev. Mod. Phys.* **84**, 1067–1125 (2012).

153. Stauber, T., Peres, N. M. R. & Guinea, F. Electronic transport in graphene: A semiclassical approach including midgap states. *Phys. Rev. B* **76**, 205423 (2007).

154. Cao, B. Y., Yao, W. J. & Ye, Z. Q. Networked nanoconstrictions: An effective route to tuning the thermal transport properties of graphene. *Carbon* **96**, 711–719 (2016).

155. Srivastava, N. *et al.* Low-energy electron reflectivity of graphene on copper and other substrates. *Phys. Rev. B* **87**, 245414 (2013).

156. Willke, P. *et al.* Short-range ordering of ion-implanted nitrogen atoms in SiC-graphene. *Appl. Phys. Lett.* **105**, 111605 (2014).

157. Wang, W., Munakata, K., Rozler, M. & Beasley, M. R. Local transport measurements at mesoscopic length scales using scanning tunneling potentiometry. *Phys. Rev. Lett.* **110**, 236802 (2013).

158. Aleiner, I. L. & Efetov, K. B. Effect of disorder on transport in graphene. *Phys. Rev. Lett.* **97**, 236801 (2006).

159. Lauffer, P. *et al.* Atomic and electronic structure of few-layer graphene on SiC(0001) studied with scanning tunneling microscopy and spectroscopy. *Phys. Rev. B - Condens. Matter Mater. Phys.* **77**, 1–10 (2008).

160. Tworzydło, J., Trauzettel, B., Titov, M., Rycerz, A. & Beenakker, C. W. J. Sub-poissonian shot noise in graphene. *Phys. Rev. Lett.* **96**, 264802 (2006).

161. Danneau, R. *et al.* Evanescent wave transport and shot noise in graphene: Ballistic regime and effect of disorder. *J. Low Temp. Phys.* **153**, 374–392 (2008).

162. Momeni Pakdehi, D. Optimization of Epitaxial Graphene Growth for Quantum Metrology. (2020).

List of Abbreviations

0D *zero-dimensional*

1D *one-dimensional*

2D *two-dimensional*

3D *three-dimensional*

ADC *analogue-digital converter*

AFM *atomic force microscopy*

AM-AFM *amplitude modulation atomic force microscopy*

AM-KPFM *amplitude modulation Kelvin probe force microscopy*

ARPES *angle-resolved photoemission spectroscopy*

BN *boron nitride*

CCT *constant current topography*

CVD *chemical vapor deposition*

DAC *digital-analogue-converter*

FM-KPFM *frequency modulation Kelvin probe force microscopy*

HOPG *highly oriented pyrolytic graphite*

KPFM *Kelvin probe force microscopy*

LDOS *local density of states*

LEED *low-energy electron diffraction*

LEEM *low-energy electron microscopy*

ML–BL *monolayer-bilayer*

N4PP *nano 4-point probe*

PASG *polymer-assisted sublimation growth*

QFBLG *quasi-free-standing bilayer graphene*

QFMLG *quasi-free-standing monolayer graphene*

QHE *quantum Hall effect*

SG *sublimation growth*

SiC *silicon carbide*

SiO_2 *silicon dioxide*

STM *scanning tunneling microscopy*

STP *scanning tunneling potentiometry*

STS *scanning tunneling spectroscopy*

TEM *transmission electron microscopy*

UHV *ultra-high vacuum*

ZL *zero layer*

Danksagung

Zum Schluss möchte ich mich noch bei all denjenigen bedanken, die mich während meines Studiums und der Promotion unterstützt und somit maßgeblich zum Gelingen dieses Vorhabens beigetragen haben.

Als erstes danke ich PD Dr. Martin Wenderoth, der es mir ermöglicht hat dieses faszinierende Projekt durchzuführen. Besonders geholfen bei der Realisierung haben mir die anregenden und kreativen Diskussionen, die Beantwortung vieler Fragen, sowie die konstruktive Kritik und die wiederkehrende Frage nach „dem anschaulichen Bild dahinter“. Diese zahllosen Diskussionen haben mein physikalisches Verständnis enorm erweitert.

Mein Dank gilt ebenso Herrn Prof. Dr. Hans Hofsäss für die Übernahme des zweiten Gutachtens, sowie für die Dotierung diverser Graphen Proben im Laufe dieser Doktorarbeit. Außerdem danke ich Prof. Dr. Rolf Möller für die Erstellung des dritten Gutachtens, sowie Prof. Dr. Claus Ropers, Prof. Dr. Thomas Weitz, Prof. Dr. Christian Jooß und apl. Prof. Dr. Michael Seibt für die Bereitschaft in meiner Prüfungskommission mitzuwirken.

Darüber hinaus möchte ich mich bei allen aktuellen und ehemaligen Mitgliedern der AG Wenderoth bedanken, die mich während meiner Promotion begleitet haben. Die freundliche Atmosphäre und die enorme Hilfsbereitschaft untereinander haben entscheidend dazu beigetragen, dass ich mich stets wohlgefühlt habe. Hervorheben möchte ich an dieser Stelle Dr. Philip Willke, dem ich zu Dank verpflichtet bin für die Einweisung in die experimentellen Techniken, für herausfordernde Aufgaben und kreative Denkanstöße, sowie Georg Traeger, Benno Harling und Simeon Bode, die ich im Rahmen unterschiedlicher Abschlussarbeiten betreuen durfte. Herzlich danke ich auch meinen Korrekturlesern Georg Traeger und Dr. Thomas Kotzott.

Ein besonderer Dank geht außerdem an den technischen und elektronischen Support ohne den diese Arbeit nicht möglich gewesen wäre. Insbesondere möchte ich hier Bernhard Spicher nennen, dessen technische Expertise Grundlage für die In-

betriebnahme und Erhaltung der experimentellen Anlagen ist, sowie allen Mitgliedern der Werkstätten für die Abwicklung größerer und kleinerer Aufträge. Dr. Jörg Malindretos danke ich für die Einweisung und umfangreiche Unterstützung bei der Bedienung des Bonders, sowie der 4-Probe-Station.

Weiterhin bin ich PD Dr. Hans Werner Schumacher, Dr. Klaus Pierz und Dr. Davood Momeni für die Herstellung diverser qualitativ hochwerter Graphen Proben und für zahlreiche Diskussionen zu Dank verpflichtet. Darüber hinaus möchte ich mich bei weiteren Forschungspartnern bedanken: Prof. Dr. Christoph Tegenkamp, Prof. Dr. Thomas Seyller, Dr. Florian Speck und Philip Schädlich für die intensive Zusammenarbeit an den Ursachen der lokalen Widerstandsvariation, Prof. Dr. Hans Hofsäss, Manuel Auge, Felix Junge, Dr. Gunther Lippert und Dr. Mindaugas Lukosius für die erfolgreiche Kooperation zur Erforschung von Graphen auf Ge/Si(001), sowie Prof. Dr. Sense Jan van der Molen, Dr. Johannes Jobst und Tobias A. de Jong für die interessanten Einblicke in die Welt der niederenergetischen Elektronenmikroskopie.

Dankbar bin ich ebenfalls für meine Freunde, die immer für mich da waren ob aus der Ferne oder in Göttingen. Ihr habt mein Leben außerhalb der Physik bereichert. Ein riesiger Dank gilt meiner gesamten Familie für die grenzenlose Unterstützung nicht nur während der Promotion, sondern auch auf dem Weg dorthin. Ich danke euch für euren Zuspruch in allen Lebenslagen.